

Copyright Undertaking

This thesis is protected by copyright, with all rights reserved.

By reading and using the thesis, the reader understands and agrees to the following terms:

- 1. The reader will abide by the rules and legal ordinances governing copyright regarding the use of the thesis.
- 2. The reader will use the thesis for the purpose of research or private study only and not for distribution or further reproduction or any other purpose.
- 3. The reader agrees to indemnify and hold the University harmless from and against any loss, damage, cost, liability or expenses arising from copyright infringement or unauthorized usage.

IMPORTANT

If you have reasons to believe that any materials in this thesis are deemed not suitable to be distributed in this form, or a copyright owner having difficulty with the material being included in our database, please contact lbsys@polyu.edu.hk providing details. The Library will look into your claim and consider taking remedial action upon receipt of the written requests.

UNRAVELING THE PHASE TRANSITION OF FORMAMIDINIUM LEAD IODIDE THIN FILM MEDIATED BY DEFECTS USING INSITU AND EX-SITU MICROSCOPY

YANG CHEN

PhD

The Hong Kong Polytechnic University

2025

The Hong Kong Polytechnic University Department of Applied Physics

Unraveling The Phase Transition of Formamidinium

Lead Iodide Thin Film Mediated by Defects Using In
Situ and Ex-Situ Microscopy

Yang Chen

A thesis submitted in partial fulfilment of the requirements for the degree of Doctor of Philosophy

August 2024

CERTIFICATION OF ORIGINALITY

I hereby affirm that the doctoral thesis submitted for the degree of Doctor of Philosophy
at The Hong Kong Polytechnic University is entirely my own original work. I attest
that this thesis has not incorporated any material previously published or written by
another person, nor has it been submitted to secure any other degree or credential. All
external references and sources have been explicitly acknowledged and duly cited
within the thesis text.
(C: 1)
(Signed)

Yang Chen (Name of student)



Abstract

Over a prolonged period, the energy problem has been a focal point of global concern. The direct application of solar energy is regarded as one of the most promising solutions to alleviate or resolve this issue. The development of FAPbI₃ has substantially advanced the field of photovoltaics, largely due to its exceptional electronic properties and an optimal bandgap of approximately 1.48 eV. However, this material has perpetually faced numerous challenges, among which the issue of stability remains a significant concern for scientists. This problem has attracted considerable attention, leading to extensive efforts in both mechanistic studies and engineering improvements. In the fabrication of FAPbI₃ devices, annealing induces the transformation of FAPbI₃ from the non-photoactive δ phase to the photoactive α phase. The advancement of FAPbI₃ devices is intrinsically linked to a profound understanding of this phase transition process, therefore, intuitive observation of this phase transition is essential. Particularly, 4D STEM (scanning transmission electron microscopy) is invaluable for capturing the orientation relationship at the phase boundary and the formation of defects during the phase transition.

In this thesis, *in-situ* optical microscopy and *ex-situ* 4D STEM techniques are employed to explore the dynamic phase transition process, the preferred orientation during the

I



phase transition, and the formation of defects resulting from the phase transition in FAPbI₃ from the δ to α phase. Building upon the understanding gained from the characterizations, the preferred orientation of the α phase resulting from the phase transition was ultimately determined and verified by X-ray diffraction.

Initially, millimeter-sized highly oriented single crystal δ phase thin films with precisely defined $[10\overline{1}0]_{\delta}$ surface orientations were synthesized using an innovative space confined anti-solvent method. In situ annealing polarized optical microscopy was conducted at various temperatures to determine the activation energy of the δ to α phase transition in two dimensions. Furthermore, the preferred phase transition orientation $<0.002>_{\delta}$ over $<2.110>_{\delta}$ directions is examined. Subsequent *ex-situ* 4D-STEM characterization of the transferred thin films elucidated a specific phase transition relationship: $\langle 10\bar{1}0\rangle_{\delta}//\langle 001\rangle_{\alpha}$, $\{1\bar{2}10\}_{\delta}//\{210\}_{\alpha}$, and $\{0002\}_{\delta}//\{120\}_{\alpha}$. Boundary analysis revealed a preferred $\{210\}_{\alpha}$ interphase boundary, the non-coherent interphase boundary reveals the reconstructive behavior of this phase transition, further evidenced by the observed ledge growth mode. Furthermore, analysis of the regions near the transition front, the degree of amorphousness and the defect density progressively increases. Hence, this study proposed a systematic approach to investigate the underlying mechanisms of the δ to α phase transition in FAPbI₃, examining the anisotropy inherent in this transition. This work advances the understanding of the



phase transition, providing insights into the anisotropic nature of the transformation. Additionally, the study elucidates the prevalent $[001]_{\alpha}$ orientation commonly observed in FAPbI₃.

This thesis also scrutinizes the degradation of FAPbI₃ under moist conditions, focusing not only on the δ to α phase transition in perovskite but also utilizing X-ray diffraction (XRD) and transmission electron microscopy (TEM) with selected area electron diffraction (SAED) to investigate the degradation phenomenon. In this experimental section, the active layer, consistent with device fabrication, was prepared as a free-standing sample. The XRD analysis revealed a distinct peak at $2\theta = 11.78^{\circ}$, while SAED confirmed this peak to be confined $10\overline{10}_{\delta}$ peak. Subsequent degradation experiments under ultraviolet and high humidity conditions demonstrated an initial strengthening followed by decay of the confined $10\overline{10}_{\delta}$ peak. This observation suggests that the degradation of FAPbI₃ samples maybe initiated by such defects.

These findings shed light on the phase transition from δ to α and both degradation mechanisms of FAPbI₃, highlighting the utility of XRD and TEM techniques in comprehending the underlying phase transition mechanism. This understanding fills a critical gap which significantly aids in further modifications of this material.



List of Publication

Chen Yang, Changsheng Chen, Tieyuan Bian, Chao Xu, Xiangli Che, Dongyang Li, Xuezhe Dong, Kuan Liang, Jun Yin, Gang Li*, Ye Zhu*.
 "Anisotropic δ-to-α Phase Transition in Formamidinium Lead Iodide Thin Films. "ACS nano, 19(9), 9225-9231.



Acknowledgements

First and foremost, I extend my deepest gratitude to my advisor, Professor. Ye Zhu, for his unwavering support and invaluable guidance throughout my doctoral journey, I vividly recall the profound reflections and growth I underwent after each Thursday's one-on-one meetings with professor. Zhu. His guidance has transcended the ordinary bounds of a teacher-student relationship, touching the very core of my academic and personal development, it is a profound privilege to forever be your student. I am also immensely grateful to my co-advisor, Professor. Gang Li from the EEE department, whose insights and expertise have significantly enriched my research experience.

I would like to express my sincere appreciation to my colleagues and group members, Dr. Xiangli Che, Dr. Chao Xu, Dr. Changsheng Chen, Dr. Yunduo Yao, Dr. Shanru Yan, Dr. Xuyun Guo, Mr. Zhihang Xu, Mr. Yezhou Hu, Mr. Cenchen Zhong, Mr. Kuan Liang, Mr. Junyi Yue and Mr. Chunhong Chen, for their collaborative spirit and contrast encouragement. Their contributions to my scientific growth and well-being have been immeasurable.

Special thanks are owed to Dr. Chao Xu, Dr. Changsheng Chen, Dr. Zhiwen Ren, Dr. Kuan Liu, and Dr. Jiaming Huang for their assistance with my experiments and for sharing their technical expertise, which was crucial to the completion of this research.



On a personal note, my heartful appreciation goes to my parents and mother-in-law for their endless love, support, and sacrifices. Their strength and encouragement have been fundamental in my life and throughout this academic endeavor.

I extend my heartfelt thanks to Dr. Hardy Lui, Dr. Wei Lu and the supportive staff at UMF for their invaluable assistance throughout my research.

I owe a special thanks to my son, Antony, whose presence brings boundless joy and inspiration. His understanding and cheerful smiles provided me with the strength to persevere through the toughest times.

To my beloved wife, Fanny, words cannot fully capture the depth of my gratitude. Your steadfast support has been my anchor during the most challenging times of my academic journey. You have managed our life with grace and resilience, allowing me to pursue my passion for research. Your patience, encouragement, and love have not only sustained me but have inspired me every day. Thank you for being my partner, my confidant, and my best friend. I am truly blessed to share this with you. I love y'all~

This journey would not have been possible without the collective support and encouragement of everyone mentioned here, as well as many others who have contributed in various ways to my academic and personal development. I am deeply thankful for the opportunity to learn from and growth with you all.



Table of contents

Abstra	ct	I
List of	Publication	IV
Ackno	wledgements	. V
List of	Figures	. X
List of	Tables	ΚV
Chapte	er 1 Introduction	1
1.1	Background	1
1.2	Objectives and scope of research	11
1.2.1	Objectives	11
1.2.2	Synopsis of Thesis	17
Chapte	er 2 Literature review	21
2.1 Ir	ntroduction to hybrid perovskite	21
2.1.1 E	Basic information of perovskite	22
2.1.2 T	Colerance factor and octahedral tilting	24
2.2 H	ybrid perovskite synthesis and fabrication	28
	Antisolvent engineering	
	Additive engineering	
	Single crystal bulk and thin film hybrid perovskite	
	tructural and dynamic investigation of hybrid perovskite.	
	TEM analysis on MAPbI ₃ and FAPbI ₃	
	Oynamic study of FAPbI ₃ phase transition	40
Chapte	er 3 Anisotropic δ-to-α phase transition in	
Forma	midinium Lead Iodide thin films	44

3.1 Introduction	44
3.2 Material preparation and characterization	46
3.2.1 Synthesis of single crystal bulk prism δ-FAPbI ₃	46
3.2.2 Synthesis of epitaxial δ -FAPbI $_3$ thin film	47
3.2.3 Transfer of FAPbI ₃ thin film onto TEM grid	48
3.2.4 X-ray Diffraction (XRD)	48
3.2.5 In-situ optical polarized microscopy	49
3.2.6 Confocal PL	49
3.2.7 Transmission electron microscopy (TEM)	50
3.2.8 4D-STEM	
3.2.9 Density functional theory (DFT) calculations	51
3.3 Results and discussion	52
3.3.1 Single crystal δ-FAPbI ₃ prism	52
3.3.2 Epitaxial δ-FAPbI ₃ thin film	55
3.3.3 Kinetics analysis using JMA model	70
3.3.4 Beam effect analysis on stacking stability of $\{1210\}$ and $\{0002\}$	73
3.4 Conclusion	75
Chapter 4 Polycrystalline perovskite thin film	
degradation	77
4.1 Introduction	
4.2 Material preparation and characterization	
4.2.1 Precursor preparation	
4.2.2 Device fabrication	
4.2.3 Free standing TEM sample preparation	
4.2.4 Ex-situ TEM	
4.2.5 Ex-situ XRD and in-situ XRD	80
4.3 Results and discussion	8 1
4.4 Conclusion	95
Chapter 5 Conclusions and future work	
5.1 Summary of work	
2.1 Samma 1 of horr	·····/ 1

5.2 Future work......101

(%)	
5.2.1 Synthesis of single crystal α-FAPbI ₃ thin film	
5.2.2 Degradation of single crystal α-FAPBI ₃ thin films	102
5.2.3 Low-dose high resolution imaging	102
5.2.4 Mixed halide and cation system	102
Reference	103



List of Figures

Figure 1.1 Schematic of historical progression of photovoltaic cell
efficiencies across various technologies from 1975 to 2023. Adapted from
NREL. ¹¹ 4
Figure 1.2 Schematic illustration of crystal structure of perovskite material.
6
Figure 1.3 Illustration of in Situ/operando characterization, combing
deposition techniques and multiple beam sources with detectors under
external stimuli for perovskite thin film analysis. ³²
Figure 2.1 Elucidation of perovskite structures. a) natural mineral perovskite
crystals. b) depiction of molecular structure displaying atomic positions of A,
B and X atoms within the perovskite framework. c) illustration of perovskite
formation showcasing an octahedron encasing the A cation, exemplifying an
ideal perovskite formation. d) representation of a non-perovskite structure
characterized by octahedra with face-sharing configuration22
Figure 2.2 Displays the structural evolution of hybrid perovskite materials
from three-dimensional perovskite to RP configurations for $n=1$ and $n=2$,
extending from n=0 to n= ϖ , where n= ϖ denotes a three-dimensional
perovskite structure. ⁵²
Figure 2.3 Progressive stages in the development of single crystal perovskite
bulk and thin film synthesis. (a) Time-dependent inverse-temperature
crystallization of $\alpha\text{-FAPbI}_3$. ⁸⁵ (b) Surface hydrophobic modification for
single crystal $MAPbI_3$ and $MAPbBr_3$ thin film using space confined and
inverse temperature method. ⁸⁷ (c) Pressure-induced MAPbBr ₃ single crystal
thin film synthesis with ultra-thin film thickness combining space confined
and inverse temperature method. ⁸⁹
Figure 2.4 Twinning model and actual SAED pattern of MAPbI ₃ . (a)
Description of the twin-domain structure in zone axis [1 10]. (b) SAED
pattern of [1 $\overline{10}$] oriented MAPbI3 twin with θ =1° point split at the 220
diffraction spot. c) Schematic model of the continuous {112} twin structure. 93



......38

Figure 3. 1 Characterization of single crystal δ -FAPbI ₃ prism. (a) optical
image from both top and side perspectives of the obtained $\delta ext{-FAPbI}_3$ prism.
(b) PL spectra for the black prism (after annealing). The inset image depicts
the black crystal after being adequately annealed at 150°C. (c) XRD patterns
obtained by solely tilting the chi angle from 0° to 30° to 60° , focusing on the
side and corner lattice structures of the δ -FAPbI $_3$ prism. (d) XRD
measurement results from the top side of the crystal, with combined tilting at
chi 90° and phi 90°
Figure 3. 2 Powder X-ray diffraction (PXRD) patterns of prism ground into
powder. (a) yellow prism, (b) black prism, compared with the simulated
diffraction pattern
Figure 3. 3 Synthesis protocol of epitaxial δ-FAPbI ₃ thin films using a
combination of space-confined and antisolvent methods, and optical images
of a film before and after annealing
Figure 3. 4 (a) AFM height map of a δ-FAPbI ₃ thin film. (b) Height profile
along the red arrow in A, showing a surface roughness (Ra) of 3.32 nm. (c)
Profilometry thickness measurement, with the inset optical image indicating
the scan direction over the sample. (d) Rocking curve measurement on 1010
diffraction with full width at half maximum (FWHM) $\sim 0.222^{\circ}.$ 57
Figure 3.5 (a) Ex situ XRD of a FAPbI ₃ thin film before (yellow) and after
(red) annealing at 160 °C, showing δ -to- α phase transition as indicated by
the reference XRD at the bottom. Insets: electron diffraction patterns taken
from corresponding samples. (b,c) PLM on a FAPbI ₃ thin film (b) before and
(c) after annealing, showing δ -to- α phase transition at the upper-right corner
(d-f) Confocal PL mapping on a δ -to- α transition front with (d) the optical
image, (e) PL intensity map from the same region, and (f) PL (brown) and
image intensity (blue) profiles along the red dotted arrows in (e) and (d),
respectively, with the position of the boundary indicated by the cyan arrow.
58



Figure 3.6 Illustration of the PLM mechanism on distinguish δ/α FAPbI₃¹²²: (a,b) Schematics showing (a) unchanged light polarization direction from an isotropic specimen, resulting in extinction in PLM, and (b) polarized light separation into ordinary (O) and extraordinary (E) rays from an anisotropic material, showing no extinction in PLM. (c,d) Atomic structure of (c) isotropic α -FAPbI₃ and (d) anisotropic δ -FAPbI₃ with a single optical axis Figure 3.7 (a) Confocal PL map with the selected area highlighted. (b) Corresponding PL spectra for the indicated areas in a......60 Figure 3.8 (a) Time-series PLM images showing δ -to- α phase transition induced by *in situ* annealing at 170 °C. (b) Measured α-FAPbI₃ area fraction as functions of annealing time at 150, 170, and 180 °C, respectively. (c) Derivation of activation energies for δ -to- α phase transition along <0001> Figure 3.9 (a) PLM image showing a transition front between the colored δ -FAPbI₃ and black α-FAPbI₃. (b,c) Diffraction patterns from 4D-STEM showing (b) <1.100> and (c) <0.01> zone axes for α - and δ -FAPbI₃, respectively. (d) DFT calculation on surface energies of α - and δ -FAPbI₃. (e) Dark-field image reconstructed using 0002 diffraction, showing the morphology of the transition front with the orientation relationship labelled in different colors. The upper-right inset is a diffraction pattern across the red boundary, showing the overlap of two phases with $<10.10>_{\delta}//<001>_{\alpha}$, $\{1210\}_\delta/\!/\{210\}_\alpha,$ and $\{0002\}_\delta/\!/\{120\}_\alpha,$ as illustrated by the schematic on left.67 Figure 3.10 (a) Dark-field image reconstructed using 0002 diffraction, showing the δ -to- α transition front along the dotted line. (b) Reconstructed bright-field image from the same region as (a), showing high-density planar defects in the newly formed α-FAPbI₃ near the transition front. (c) Measured 020 diffraction peak width along the red arrow in (b), showing increased defect density towards the transition front. The initial and final diffraction patterns are shown in the insets......70



Figure 3.11 (a) Reconstructed dark-field image using 001 diffraction showing the δ -to- α transition front in FAPbI ₃ . (b) Selected 5x3 scan region across the
transition front. (c) Corresponding electron diffraction patterns at each scan
position, where the radius of the circles represents $1/d_{100}$ 71
Figure 3.12 Estimation of the growth exponent n from the plot of the δ-to-α phase transition at 150 °C and 170 °C73
E' 2 12 () N
Figure 3. 13 (a) Normalized intensity of 1210 and 0002 diffraction as a
function of accumulated electron dose. The inset shows the diffraction
patterns captured at the initial (left) and final (right) stages of beam exposure.
(b) Measured 0002 and 1210 peak width along <0001> and <1210>
respectively74
Figure 4. 1 Illustration of free-standing FA _x MA _{1-x} PbI ₃ TEM sample
preparation
Figure 4.2 SAED analysis of polycrystalline FA _X MA _{1-X} PbI ₃ thin films. (a,b)
the SAED patterns of FAPbI $_3$ along the $[110]_\alpha$ zone axis, highlighting
stacking faults. (c,d) depict the SAED patterns for FA _{0.8} MA _{0.2} PbI ₃ along the
same zone axis. (e) provides a schematic representation of twin formation in
relation to the $(111)_{\alpha}$ plane along the $[110]_{\alpha}$ zone axis
Figure 4.3 The molecular diagrams of α - and δ -FAPbI ₃ , displayed along their
respective zone axes. (a) $[1210]_{\delta}$ // $[110]_{\alpha}$. (b) $[0001]_{\delta}$ // $[111]_{\alpha}$. (c) single
layer atomic distribution of the $\{111\}_{\alpha}$ and $\{0001\}_{\delta}$
Figure 4.4 Illustration of the α-δ-FAPbI ₃ heterojunction. (a) presents the XRD
spectra for FAPbI ₃ , FA _{0.8} MA _{0.2} PbI ₃ , and FA _{0.6} MA _{0.4} PbI ₃ . (b) depict the TEM
and SAED images for FA _{0.8} MA _{0.2} PbI ₃ , respectively. (c) shows a combined
simulated SAED pattern featuring $[110]_{\alpha}$ and $[2110]_{\delta}$ zone axis
Figure 4.5 Degradation of FAPbI ₃ under UV and relative humidity of 88%.
(a) XRD results of pristine FAPbI ₃ polycrystal thin film, and under UV and
water exposure for 0, 15, 27, and 35 minutes, with peak split analysis of the
$\{1010\}_{\delta}$ peak. (b) change in intensity of the split peak in relation to



degradation time. (c) XRD of FAPbI ₃ thin film from 2θ ranging from 10° to
15°, indicating changes in both δ -, α -FAPbI ₃ and PbI ₂ diffraction90
Figure 4.6 Degradation of FA _{0.8} MA _{0.2} PbI ₃ under UV and relative humidity of
88%. (a) XRD results of pristine polycrystal thin film, and under UV and
water exposure for 0, 10, 30, and 50 minutes, with peak split analysis of the
$\{1010\}_{\scriptscriptstyle 5}$ peak. (b) change in intensity of the split peak in relation to
degradation time. (c) XRD of $FA_{0.8}MA_{0.2}PbI_3$ thin film from 2θ ranging from
10° to 15° , indicating changes in both δ -, α -FAPbI ₃ , and PbI ₂ diffraction92
Figure 4.7 In-situ annealing XRD performed on epitaxial δ -FAPbI ₃ thin film under a vacuum condition ($<10^{-5}$ torr). The temperature was increased from
room temperature to 180°C93
Figure 4.8 In-situ annealing TEM on a single crystal δ-FAPbI ₃ thin film at a
temperature of 150°C. (a,c) TEM image of the sample before and after
annealing. (b,d) SAED of the sample before and after annealing at 150°C.
(inset) enlarged electron diffraction pattern of the area highlighted by the blue
dashed box



List of Tables

able 2.1 Woodward's expansion and revision of Glazer's space grou
assification for perovskite tilting systems with consideration of atomic
ositions. ⁵⁸
able 2. 2 Information on common antisolvents including boiling points an
ipole moments. ⁷⁰ 3



Chapter 1 Introduction

1.1 Background

As the world progresses, the increasing demand for the energy is primarily driven by factors such as population growth, urbanization, and industrialization. According to the latest data from the International Energy Agency (IEA), global energy consumption is on a trajectory to grow significantly over the next few decades. Fossil fuels like coal, oil, and natural gas still make up a substantial portion of global energy use, accounting for about 82% of the total primary energy consumption in 2023.

The combustion of these fossil fuels releases significant amounts of greenhouse gases, notably carbon dioxide, contributing to global warming and climate change. In response, there's a marked global pivot towards renewable energy sources to tackle these environmental and sustainability challenges. Solar energy, in particular, plays a crucial role due to its vast potential and availability. Its's estimated that the sun delivers around 173000 terawatts of solar energy continuously to Earth, vastly outstripping global energy needs.³

As of 2024, solar power contributes approximately 4.5% to global electricity generation,



with an installed capacity of around 1600 gigawatts (GW).⁴ Projections indicate that by 2050, solar capacity could reach between 8000 to 10000 GW, significantly impacting global energy production and potentially providing up to 25% of the world's electricity, this increase reflects a compound annual growth rate of about 9%.⁵ This growth in solar capacity is facilitated by photovoltaic systems and solar thermal technologies, which provide a substantial portion of our energy needs without depleting resources or causing environmental harm.

Notably, the production of solar energy does not generate air pollution or carbon emissions, positioning it as a clean and sustainable alternative to fossil fuels. The adoption of solar energy helped avoid approximately 2.3 gigatons of carbon dioxide emissions in 2023 alone.⁶ Furthermore, technological advancements have significantly enhanced the efficiency and reduced the cost of solar panels, with the cost of electricity from utility-scale solar PV decreasing by about 85% between 2010 and 2020, this reduction in costs was driven by improvements in technology, economies of scale, competitive supply chains, and increased developer experience, the cost decreased from around USD 0.381 per kWh in 2010 to USD 0.057 per kWh in 2020.⁷ The shift towards renewable energy, especially solar, is crucial for reducing our carbon footprint and achieving a sustainable energy future.

In recent decades, solar cell technology has seen remarkable advancements, as depicted



have also made significant strides.

in Figure 1.1, which records the best research-cell efficiencies from 1975 to 2023. Among which traditional silicon-based solar cells have been the cornerstone of the PV industry due to their balance of efficiency, cost, and stability. Over the years, both single-crystal and multi-crystalline silicon cells have achieved notable efficiency improvements. As of the latest data, single-crystal silicon cells have reached efficiencies approaching 27%. Besides that, multi-junction cells represent a significant leap in solar technology, primarily used in concentrated photovoltaics and space applications. These cells leverage multiple layers, each designed to absorb a different portion of the solar spectrum, thus achieving higher efficiencies. Apart from traditional silicon cells, single-junction cells based on other materials such as cadmium telluride (CdTe), copper indium gallium selenide (CIGS), and emerging perovskite materials

Perovskite solar cells, in particular, have shown extraordinary advancements in efficiency over the past decade. Since their inception, the power conversion efficiency (PCE) of PSCs has increased dramatically from about 3.8% in 2009 to over 25% in recent years. This rapid progression is unparallel in the history of solar technology and highlights the significant potential of perovskite materials in the photovoltaic sector. Perovskite solar cells have gathered significant attention due to their high efficiency, low cost, and versatility. The term "perovskite" refers to a specific crystal structure that



many materials can adopt, with the general formula ABX₃.

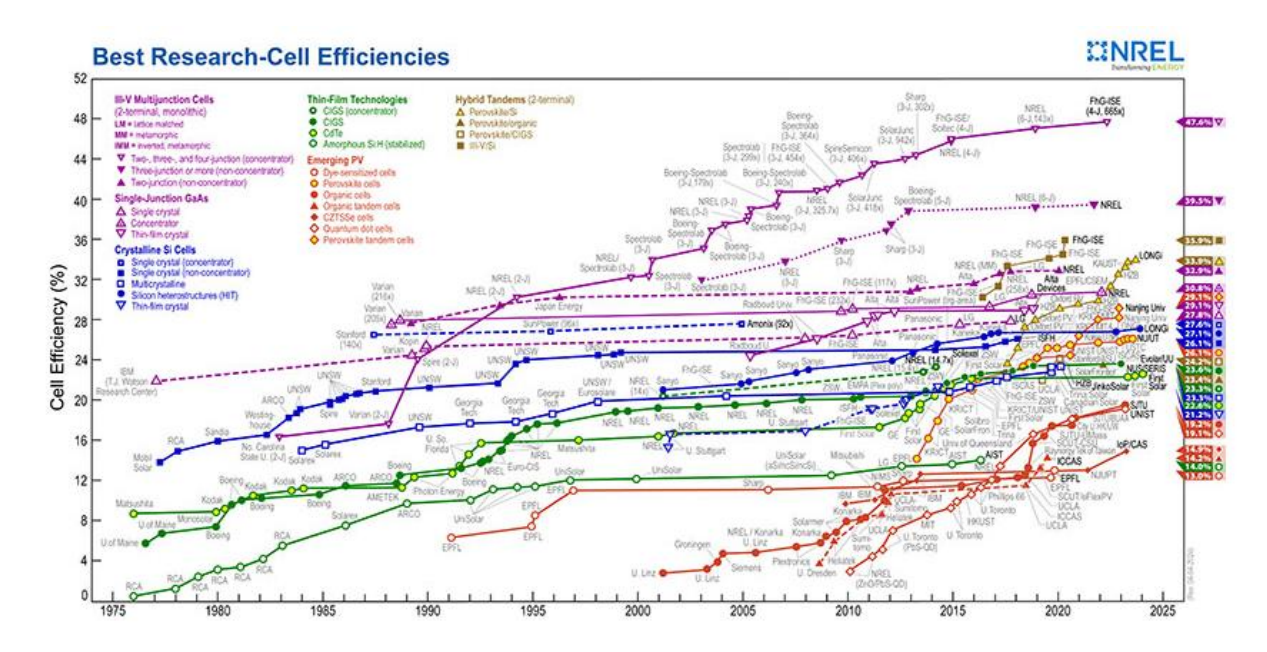


Figure 1.1 Schematic of historical progression of photovoltaic cell efficiencies across various technologies from 1975 to 2023. Adapted from NREL.¹¹

In the context of solar cells, the most commonly used perovskite material is a hybrid organic- inorganic compound. The 'A' site is typically occupied by an organic cation such as methylammonium (CH₃NH₃+) or formamidinium (HC(NH₂)₂+), the 'B' site by a metal cation such as lead (Pb²⁺), and the 'X' site by a halide anion such as iodide (I'), bromide (Br'), or chloride (Cl'). Typical chemical reaction $CH_3NH_3I + PbI_2 \rightarrow CH_3NH_3PbI_3$ and $HC(NH_2)_2I + PbI_2 \rightarrow HC(NH_2)_2PbI_3$ illustrate the formation of methylammonium lead iodide (MAPbI₃) and formamidinium lead iodide (FAPbI₃), which are common perovskite materials used in perovskite solar cells.⁹ ¹² All the precursors involved in these reactions can be readily dissolved in common solvents



such as dimethylformamide (DMF) or dimethyl sulfoxide (DMSO). This solubility facilitates the solution-processing techniques, and these precursors are abundant and relatively inexpensive, making the overall cost of perovskite solar cell production lower compared to other photovoltaic techniques.

The perovskite crystal structure is characterized by its cubic lattice, where the metal cation (B) is surrounded by six halide anions (X) forming an octahedron as depicted in Figure 1.2. The organic cation (A) occupies the spaces between these octahedra. This structure can be visualized as a three-dimensional network of corner-sharing octahedra. Due to the differences in atomic radii, the crystal structure of perovskite undergoes changes, consequently, scientists has been widely using tolerance factor to guide the design of hybrid perovskite structures or components since the introduction of the concept by Goldschmidt in 1926 to describe crystal structure stability.^{13, 14 15} The tolerance factor equation is expressed as $t = \frac{r(A) + r(X)}{\sqrt{2}(r(B) + r(X))}$, where r(A), r(B) and r(X) represent the atomic radius of A cation, B cation and X anion, respectively. 16 It is worth noting that r(A) + r(X) represents the bond length of AX while r(B) + r(X)represents the bond length of BX. The tolerance factor provides a geometric perspective on the perovskite structure; ideally, when the t=1, the cubic crystal structure, with a=b=c, $\alpha = \beta = \gamma = 90^{\circ}$ can be tightly formed. Empirically, perovskite materials with t value between 0.8 to 1 can crystallize into the perovskite structure. Taking into account the



atomic radii of Pb^+ (1.03 Å), I^- (2.20 Å), I^8 the influence of A site cation electronegativity on lead and iodide radii is neglected. The atomic radius of A^+ is found to be approximately 2.37Å to achieve a tolerance factor of 1. However, the largest naturally alkali cation, Cs^+ (1.81 Å), I^9 is relatively small to form a stable perovskite structure. Therefore, organic cations with larger radii, such as I^+ (2.17Å) and I^+ (2.53Å), I^7 have been favored by scientists. Especially I^+ FAPbI3, which has a more suitable bandgap (~1.48 eV) I^+ (2.20 compared to MAPbI3 (~1.55 eV), I^+ the narrower bandgap of I^+ FAPbI3 allows for better absorption of the solar spectrum, particularly in the read and near-infrared regions, leading to improved overall device performance.

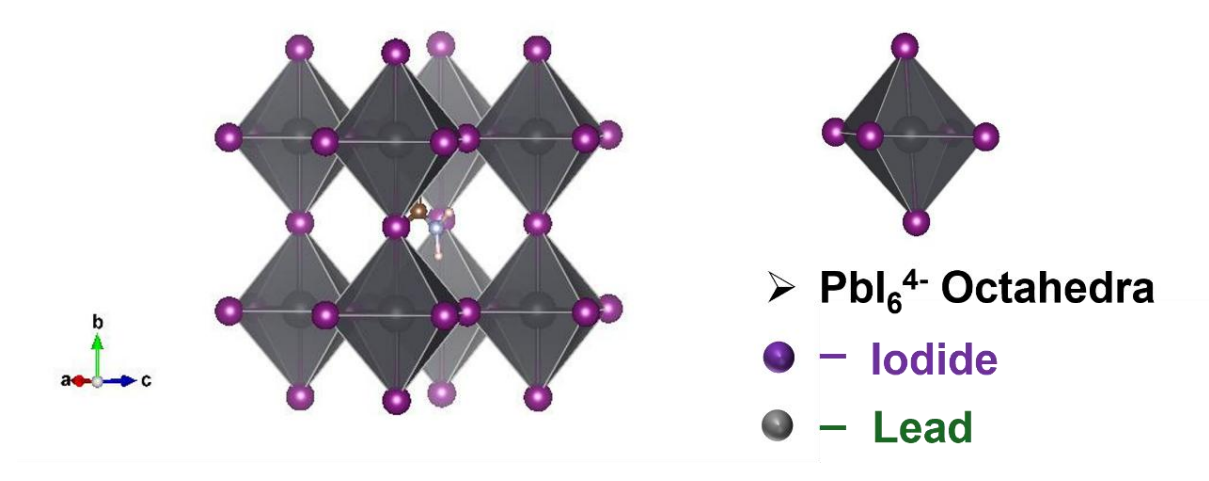


Figure 1.2 Schematic illustration of crystal structure of perovskite material.

In the case of FAPbI₃, a tolerance factor of 1.036 ¹⁸ for FAPbI₃ suggests that longer FA-I bonds can provide more space for Pb movement. This situation is comparable to the study of inorganic oxide perovskite with t>1, such as BaTiO₃ and PbTiO₃,²¹ where a



ferroelectric distortion, even in a hexagonal phase, can be produced. The finding regarding FAPbI₃ solar cells is in line with previous research indicating that FAPbI₃ exhibits two phases at ambient temperature: δ -FAPbI₃ (a non-photoactive yellow phase) and α -FAPbI₃ (a black photoactive phase). ²²⁻²⁴ It is worth noting that during the preparation of FAPbI₃ solar cells, annealing is a crucial step after spin-coating the precursor to induce the transition from the δ phase to the α phase. It has been reported that annealing at 150 °C can effectively overcome the phase transition barrier for additive-free FAPbI₃ in principle; ²⁵ A plethora of crystal twins or planar defects oriented along the <111> α direction have been revealed by selected area diffraction (SAED) analysis of polycrystalline FAPbI₃, ^{26, 27} and it has been established that these defects have an adverse impact on the performance of solar cells.

Previous research on the phase transition of metal zirconium has shown that the transition from body center cubic (bcc) to hexagonal close pack (hcp) passes through an intermediate face center cubic (fcc) phase. The transformation from fcc to hcp in a pure shearing mode can explain the specific crystallographic orientation relationship between the original bcc phase and the newly formed fcc phase.²⁸ Unfortunately, this crystallographic orientation relationship between the pristine and newly formed phase in FAPbI₃ has not been experimentally revealed. Hence, the incomplete understanding of phase transition mechanisms, along with the uncertainties surrounding the origins of



defect formation, remains a gentle hindrance to the further advancement of this versatile material. Understanding of the phase transition of FAPbI₃ remains critically incomplete, presenting a substantial barrier to advancements in the field. And the complexity of these phase transitions necessitates sophisticated experimental methodologies and robust theoretical frameworks to reveal the intricate dynamics involved. Achieving a thorough comprehension of these transitions is of paramount importance, as it holds the potential to significantly elucidate the mechanisms underlying defect formation during the fabrication of FAPbI₃ based devices.

The characterization methods for perovskite thin films primarily include X-ray diffraction (XRD) to analyze the crystal structure, scanning electron microscopy (SEM) and transmission electron microscopy (TEM) to reveal their surface morphology and microstructure, atomic force microscopy (AFM) to measure surface roughness and topography, UV-visible absorption spectroscopy (UV-Vis) and photoluminescence spectroscopy (PL) to study their optical properties, as well as electrical characterization methods such as conductivity measurements and hall effect measurement. **Figure 1.3** comprehensively illustrates a range of advanced in-situ analytical techniques employed for the study of perovskite materials, these methodologies encompass the structural characterization of perovskite active layers during the spin-coating process using synchrotron XRD,²⁹ in-situ heating experiments observed via SEM coupled with



cathodoluminescence (CL),³⁰ and PL testing ³¹ to evaluate the evolution of structural changes. Each technique provides critical insights into the dynamic process and structural evolution of perovskite films, facilitating a deeper understanding of the material properties and performance.

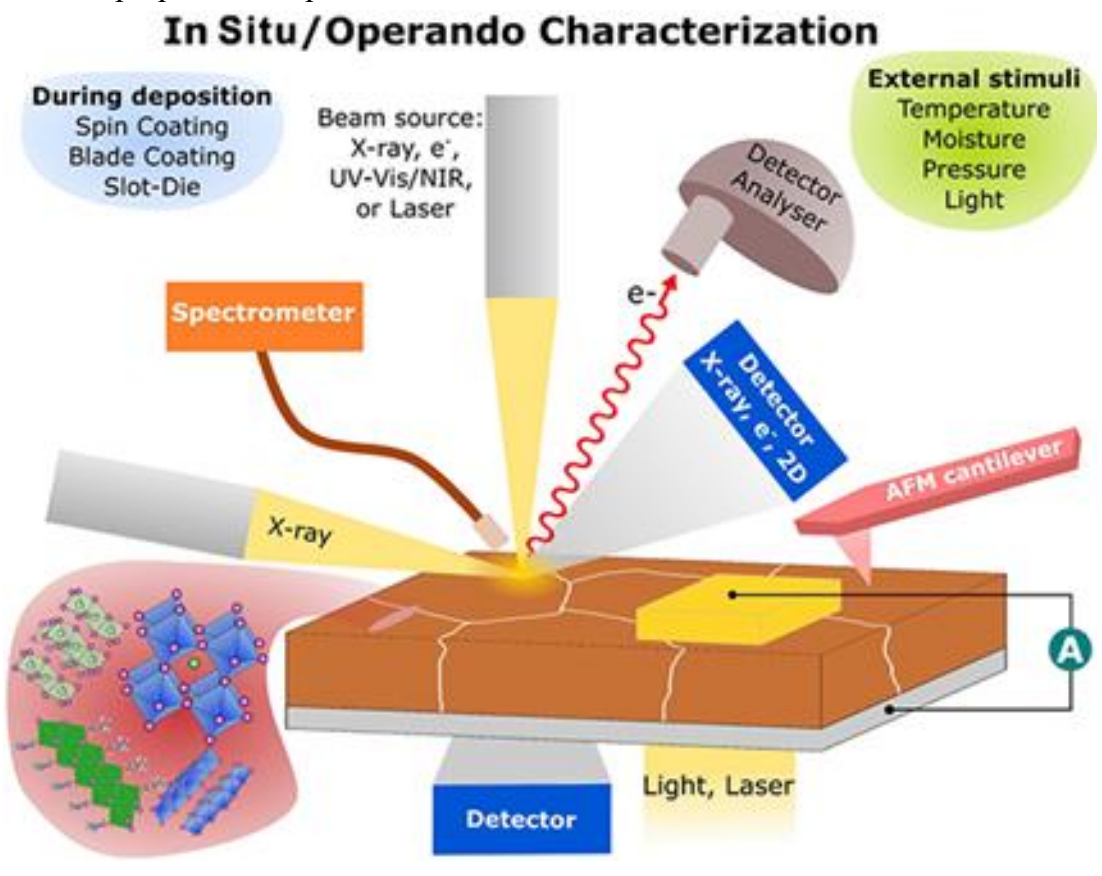


Figure 1.3 Illustration of *in Situ/operando* characterization, combing deposition techniques and multiple beam sources with detectors under external stimuli for perovskite thin film analysis.³²

However, these characterization techniques are primarily applied to polycrystalline FAPbI₃ thin films with an average grain smaller than 5 μm , ³³ making it challenging to obtain a direct view of the interphase boundary. Other techniques, such as *in-situ* Raman



spectroscopy and density functional theory (DFT),³⁴ have been employed to detect the intermediate phase during the formation of α -FAPbI₃. Nonetheless, more details still need to be revealed, including the phase transition, defect formation, interphase boundary, and related mechanisms. Thus, to better investigate this versatile material, particularly its phase transition processes, there is a significant need for more intuitive characterization methods that allow for large-area observation with minimum material damage. Therefore, the synthesis of highly oriented single-crystal δ -FAPbI₃ thin films in is a prerequisite. Performing microscopy and structural analysis during the annealing process is a highly effective method for achieving this goal.

The study of single-crystal FAPbI₃ is pivotal due to its unique properties and potential applications. Research includes advanced synthesis techniques, such as inverse temperature crystallization (ITC),³⁵ anti-solvent,³⁶ space confine growing ³⁷ and so on, to produce high-quality crystals. Mechanistic studies of FAPbI₃ single crystal are essential for understanding the material's space group and provide insights into its structure and electronic properties. These insights are crucial to optimizing FAPbI₃ for use in optoelectronic applications, including high-efficiency solar cells, LEDs, and photodetectors, ultimately driving advancements in next-generation optoelectronic devices. However, to date, there has been no research on the application of single-crystal FAPbI₃ thin films for the δ to α phase transition, nor the synthesis of bulk single-



crystal δ -FAPbI₃. Thus, this thesis proposes a novel synthesis method for producing high-quality single-crystal δ -FAPbI₃ thin films. Additionally, it employs 4D STEM techniques to study the annealing-induced phase transition, with a focus on the transition front, orientation relationships, and the formation of defects, particularly planar defects.

1.2 Objectives and scope of research

1.2.1 Objectives

Perovskite solar cells, recognized as one of the most promising and sustainable energy technologies, offer substantial potential in addressing the global energy crisis and mitigating environmental pollution. Their development is crucial in transitioning away from reliance on fossil fuels, thereby contributing to a cleaner and sustainable energy future. To date, FAPbI₃ based materials have received significant attention due to their high efficiency, efforts to enhance these materials have not only focused on material modifications but also investigating the underlying mechanism. In the fabrication of perovskite devices using a one-step method, FAPbI₃ initially forms the δ phase following spin-coating and subsequently transitions to the α phase upon annealing. This



transformation process, though critical, has not been extensively investigated. It is closely related to the preferred orientation of the films and the formation of defects. Specifically, the association between the $\{111\}_{\alpha}$ planar defects commonly observed in FAPbI₃ thin films and the phase transition process remains unexplored. ^{26, 27} Furthermore, previous studies on the phase transition kinetics of FAPbI₃ have primarily focused on the phase transition kinetics of FAPbI₃ have primarily focused on polycrystalline thin films or powders, the measurements of the activation energy for the phase transition of FAPbI₃ have exhibited considerable variation, ranging from approximately 0.84 eV to 1.814 eV.³⁸⁻⁴⁰ This significantly discrepancy suggests that the current understanding of the mechanisms underlying the FAPbI₃ phase transition remains incomplete. Such variations underscore the complexities of the dynamics and molecular interactions involved in the phase transition process that have yet to be fully elucidated. This observation underscores the necessity for further research and detailed exploration of the kinetic dynamics of FAPbI₃ phase transitions to refine theoretical models and accurately interpret experimental data.

In solid-solid phase transition transformations, the Johonson-Mehl-Avrami (JMA) model is frequently employed to describe the kinetic of the transformation process.^{41, 42}

This model is a mathematical description used to predict the kinetic of phase transformations in materials. It quantifies how a new phase grows within a matrix phase



under isothermal conditions, so quantifying the extent of phase transformation has conventionally been achieved through XRD signals or visual color changes. However, the XRD method often suffers from slow data acquisition rates and the potential degradation of perovskite materials under the high-energy X-rays typically employed in synchrotron radiation. Furthermore, identifying phase transitions by color change lacks sensitivity and can be imprecise. These limitations necessitate the exploration of alternative methodologies that provide accurate, sensitive, and non-destructive evaluations of phase transformations.

Beyond the phase transformation from δ to α , the reversal from α to δ is critically important, particularly due to the stability concerns of FAPbI₃. It is well known that the degradation of FAPbI₃ can be accelerated by moisture and light exposure. ^{13, 43, 44} Evidence indicates that water begins to erode FAPbI₃ at the boundaries, as observed in KPFM measurements. ⁴⁴ This phenomenon is understandable since grain boundaries typically possess higher boundary energy, facilitating easier phase transitions. However, intragrain defects such as planar defects and stacking faults can also contribute to the increase in total energy and may play a critical role in the origin of degradation. ⁴⁵ In the synthesis of pure FAPbI₃ thin films, the persistence of the residual δ phase is frequently observed. Notably, XRD consistently demonstrates an anomaly in the $10\overline{10}_{\delta}$ diffraction, which manifests as a split slightly preceding its theoretical position (2θ =11.78°), and



this phenomena is reported to be attributed to the effects of water interaction. ^{13, 44, 46, 47} Furthermore, DFT calculations investigating hydrogen bond interaction for FA⁺ and MA⁺ indicate that the bonding of FA⁺ with the compound is 0.10 eV to 0.15 eV weaker than that of MA. ⁴⁸ This suggests that FA⁺ may exhibit a relatively weak interaction with water, implying that the observed split peak could serve as an important indicator requiring further elucidation through additional characterization.

Based on the above considerations, to thoroughly compare the phase transition mechanism of this versatile material, it is imperative to design both in-situ and ex-situ microscopy alongside XRD characterization, particularly targeting the novel morphology of single-crystal δ -FAPbI $_3$ thin film. Systematic measurements should be implemented to achieve direct observation of the FAPbI $_3$ thin film, which will also unveil more dynamic information about the δ to α transition, especially regarding the nature of the phase transition and its anisotropy.

The objectives of this study are summarized as follows:

- A. To design and synthesize single crystalline, highly oriented, distinctive δ -FAPbI₃ thin films and bulk crystals for structure analysis.
- **B.** To directly observe the dynamic behavior of thermal annealing induced δ to α phase transition in single crystal FAPbI₃ thin films, obtaining more detailed information while minimizing the impact on the sample during experimental



observation.

- C. To correlate macroscopic phase transition information with phase transition details at the microscopic level, including the orientation relationship between δ and α phases and the phase transition front.
- **D.** To elucidate the defect formation mechanism, primarily focusing on planar defects, and their relationship with phase transitions.
- E. To investigate the degradation of polycrystalline α -FAPbI₃ thin films under moisture and illumination exposure, and to interpret the role of residual δ-FAPbI₃ from a structural perspective.

To fulfill the outlined objectives, the following methodologies are proposed:

a. To mitigate the influence of diverse cations on the investigation of phase transitions, this study utilized pure FAPbI3 as the subject of research. Moreover, to enable direct observation of the phase transitions in specific orientations, it is imperative that the FAPbI3 be configured either as a well-defined crystal bulk or as a thin film with a distinct shape. Guided by the prior narrative, the initial synthesis involved the production of a well-defined δ -FAPbI3 single crystal prism. The synthesis was conducted using antisolvent at ambient temperature. The top facet of the crystal was denoted as $\{0002\}_{\delta}$, surrounded by six side facets indexed as $\{10\overline{1}0\}_{\delta}$. Then, the experimental synthesis targeted a single



crystal δ-FAPbI₃ thin film, which was distinguished by a well-defined boundary and dimensions on the scale of hundreds of micrometers. The crystal's side plane facet was indexed as $\{10\overline{1}0\}_{\delta}$, and its corner facet was delineated by the $\{1\bar{2}10\}_{\delta}$. A bulk single crystal prism underwent systematic XRD analysis, which was precisely implemented with the specimen strategically aligned in predetermined configurations, accompanied by basal chi adjustments ranging from 0° to 60°. This methodical arrangement was essential for the detailed investigation of both edge and side facets of the crystal. In addition to traditional XRD techniques, grazing incidence wide angle X-ray scattering (GIWAXS) and in-situ annealing XRD was employed as a supplementary characterization method to assess structural changes pre and post phase transition. Furthermore, for the analysis of the single crystal thin film, in-situ annealing polarized microscopy was periodically conducted to monitor the evolution of the α phase over time. Four dimensional- Scanning transmission electron microscopy (4D-STEM) was employed to examine a sample subjected to annealing yet not fully phase-transformed, enabling the precise determination of distinct structural orientations specific to the δ/α phases. This advanced imaging technique provided an integrated assessment of both macroscopic and microscopic structural details. Additionally, when coupled with detailed amorphous analysis,



this methodology facilitated an elucidation of the progressive formation of defects within the crystalline matrix. Confocal PL spectroscopy was performed to evaluate the crystallinity within the phase transition regions of the sample.

This analysis was systematically compared to the results obtained from 4D-STEM, providing a complementary perspective on the structural changes occurring during the phase transition.

b. To elucidate the structural transformations during the degradation of the polycrystalline thin films, comprehensive analyses using XRD and TEM were conducted to provide corroborative evidence of these changes. To facilitate more precise TEM investigations, a novel methodology for preparing free-standing TEM samples was devised. This approach entailed the integration of a sacrificial layer during the fabrication of the thin films, which was later selectively dissolved using a perovskite-compatible, non-detrimental solvent, thereby enabling unobstructed electron microscopy analysis.

1.2.2 Synopsis of Thesis

This thesis documents the synthesis of δ -FAPbI $_3$ in both prism and thin film forms and characterizes the δ to α phase transition, which is crucial for comprehending the integral



process underlying perovskite device fabrication. This investigation is essential for elucidating the critical steps involved in the manufacturing of perovskite-based devices. The synthesis of single crystal δ-FAPbI₃ with well-defined shape and boundaries is essential for subsequent in-situ and ex-situ microscopy and spectroscopy measurements. For FAPbI₃ degradation studies, the newly developed free standing TEM samples are meticulously designed to replicate the authentic morphology of perovskite devices and to accurately reflect their degradation dynamics.

The structure of this thesis is organized as follows:

Chapter 1: This chapter comprehensively expounds on the trajectory of global energy utilization, emphasizing the significant strides in renewable energy innovations, particularly within the context of solar technology. Special attention is devoted to the emergent field of perovskite solar cells, with a focus on the swift advancements in FAPbI₃, a leading material in this domain. Additionally, this chapter critically examines the challenges confronting FAPbI₃ within perovskite solar applications. The articulated objectives and methodological approaches are meticulously tailored to meet the exigencies of real-world technological advancements, with a concerted focus on elucidating the complex mechanisms underlying phase transition and degradation in FAPbI₃ materials.

Chapter 2: In this chapter, an exhaustive examination of the extant academic research



on FAPbI₃ is presented, emphasizing the synthesis of knowledge concerning phase transitions, defect formation, degradation dynamic, and the phase change kinetics of FAPbI₃. This analysis incorporates a robust suite of characterizations, including XRD, GIWAX, and TEM, complemented by theoretical insights derived from density functional theory (DFT) and molecular dynamics (MD) simulations. The discourse presented herein establishes the scholarly foundation for this thesis, offering critical insights that underpin and propel the overarching research narrative.

Chapter 3: This chapter elaborates on the methodological synthesis of our pioneering δ -FAPbI₃ single crystal prism and thin films, accompanied by an in-depth material characterization that scrutinizes both the structural and compositional attributes of the materials. Subsequently, it ventures into a sophisticated analytical discourse on the findings, notably elucidating the anisotropic δ to α phase transitions that are intrinsic to the material. These phase transitions are rigorously analyzed through *in situ* annealing microscopy, systematically integrated with the Johnson-Mehl-Avrami (JMA) model, to provide a quantitative framework for assessing phase transition dynamics. The discourse extends to a precise delineation of interphase boundaries and a detailed quantification of defect structures, thereby establishing a multiscale microscopy methodology for investigating perovskite phase transition.

Chapter 4: This chapter will initially expound upon our newly established



methodology for preparation device-grown, free standing TEM samples. It will detail how XRD measurements of the δ -FAPbI₃ residual phase, when coupled with TEM, reveal diverse manifestations of the δ -FAPbI₃ existence. Additionally, the chapter will present and analyze *ex-situ* XRD results, specifically focusing on the degradation of FAPbI₃ facilitated by moisture and illumination, thereby offering a thorough evaluation of the diverse interpretations concerning the initialization of FAPbI₃ degradation.

Chapter 5: This chapter will consolidate the key findings and achievements presented in this thesis, highlighting the significant contributions to the field and demonstrating the impact of these discoveries on current understanding. Additionally, it will outline recommendations for future research directions, suggesting areas where further investigation could yield valuable insights and advancements. This discussion will also propose specific methodologies and approaches that future studies might adopt to build upon the foundational work laid out in this thesis.



Chapter 2 Literature review

In this section, an overview of the phase transition of hybrid perovskite will be discussed and detailed, with a summary provided. The discussion will be structured into three sections for clarity and thoroughness. The introductory section will first offer a comprehensive understanding of hybrid perovskite, covering its material composition, intricate structural features, and applications. The subsequent section will discuss the current study of phase transition of hybrid perovskite, with a particular focus on formamidinium lead iodide-based hybrid perovskites. Following this, the state-of-theart advancements in investigating the structure, phases, and defects of hybrid perovskite using transmission electron microscopy will be explored.

2.1 Introduction to hybrid perovskite



2.1.1 Basic information of perovskite

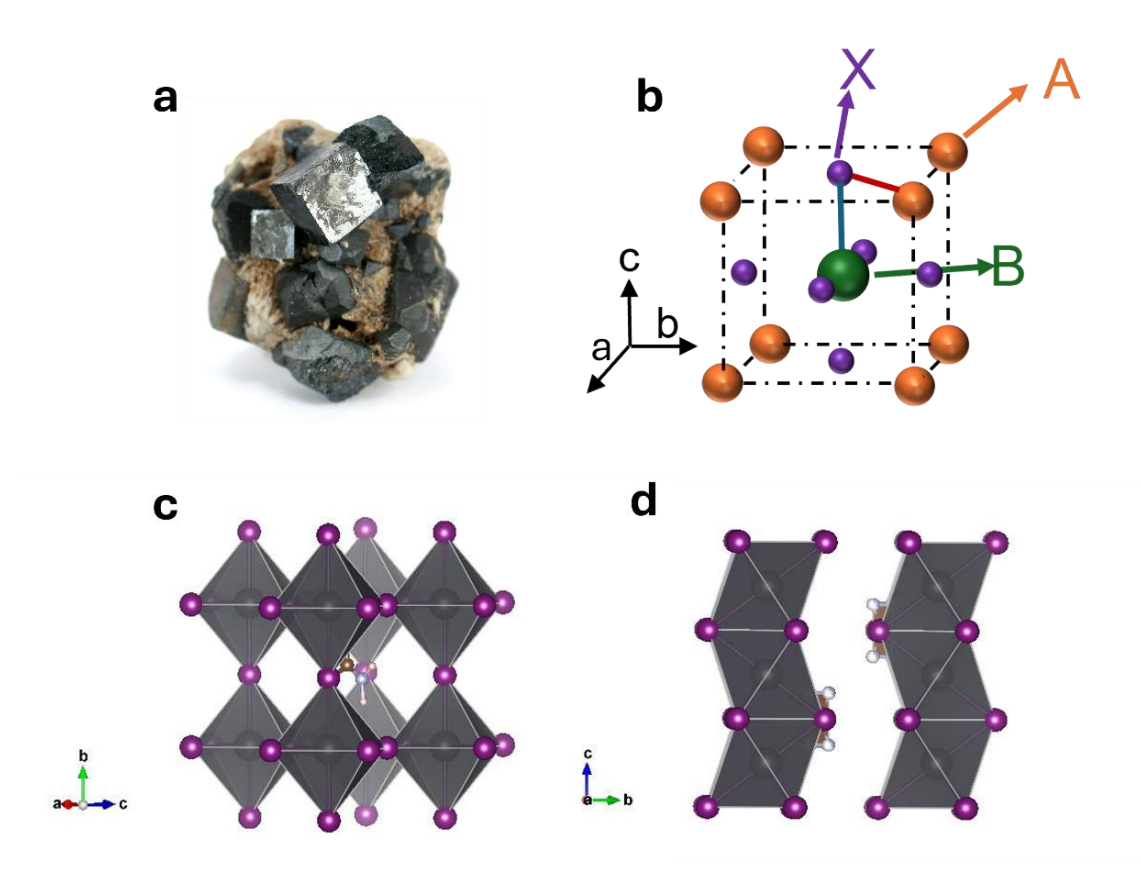


Figure 2.1 Elucidation of perovskite structures. a) natural mineral perovskite crystals. b) depiction of molecular structure displaying atomic positions of A, B and X atoms within the perovskite framework. c) illustration of perovskite formation showcasing an octahedron encasing the A cation, exemplifying an ideal perovskite formation. d) representation of a non-perovskite structure characterized by octahedra with face-sharing configuration.

Hybrid perovskites are a class of materials that have gathered wide attention during the last decade, especially in the field of optoelectronics. 10, 49, 50 These materials feature a



unique crystal structure, and their properties can be easily tuned by adjusting the components. The typical crystal structure of hybrid perovskite is illustrated in **Figure**2.1, where cation A is surrounded by eight BX₆²⁻ octahedra, ultimately forming the ABX₃ component. The primary and most significant application of hybrid perovskites lies in their use as the light-absorbing layer in solar cells.^{9, 12}

Hybrid perovskite materials can be classified into three types — one dimensional (1D), ⁵¹ two dimensional (2D), ⁵² and three-dimensional (3D) based on their structure. This classification can be achieved by altering the A-site cation to include a long chain organic molecule, such as an alkylammonium salt,⁵³ which promotes the formation of a periodic, layered structure. In these 2D-perovskites, the layers are predominantly held together by van der Waals forces, while the organic cations within the layers may interact through hydrogen bonds, this type of hybrid perovskite is also known as Ruddlesdene Popper (RP) perovskites, is represented by the formula A'₂A_{n-1}B_nX_{3n+1} where A' represent the long chain cation, and the n can be tuned by altering the concentration ratio of A'/A, and when n approaches infinity, the RP structure transitions into a three dimensional perovskite, as depicted in Figure 2.2. Owing to the elongated chain-like characteristics, the interlayer in RP perovskites becomes insulating. Consequently, these interlayers facilitate a distinct quantum well configuration in the material,⁵⁴ and the distinctive layered architecture positions it as an exemplary



candidate for the passivation of 3D-perovskites, thereby attenuating the presence of dangling bonds.⁵⁵ However, due to the layered structure of RP perovskites and the insulating properties of the interlayer, solution-processed RP perovskite typically orient with an in plane <001> direction, thereby enhancing the device's electrical resistance, consequently, the efficiency of RP perovskites has yet to match that of three-dimensional perovskites.⁵⁶

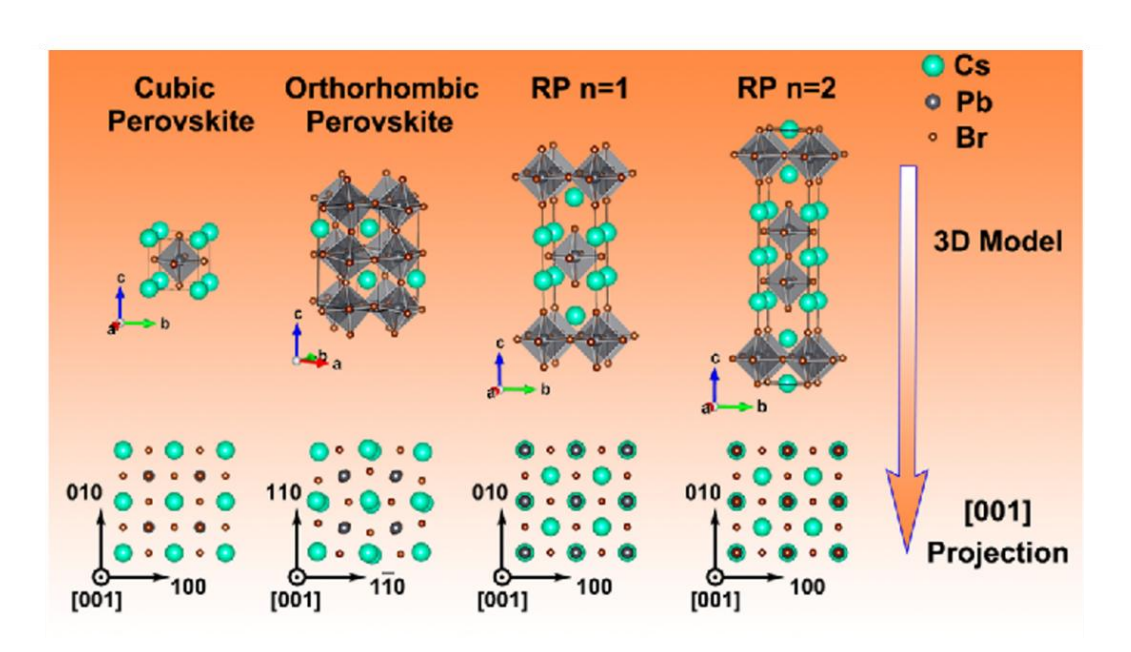


Figure 2.2 Displays the structural evolution of hybrid perovskite materials from three-dimensional perovskite to RP configurations for n=1 and n=2, extending from n=0 to n= ∞ , where n= ∞ denotes a three-dimensional perovskite structure.⁵²

2.1.2 Tolerance factor and octahedral tilting

In the assessment of perovskite structural stability, the Goldschmidt tolerance factor,



calculated using the formula $t = \frac{r(A) + r(X)}{\sqrt{2}(r(B) + r(X))}$, proves instrumental in characterizing the ideality of perovskite, in the formula, r(A), r(B) and r(X) denote the ionic radii of the A-site, B-site, and X-site ions, respectively. 16 When the tolerance factor t falls below unity, octahedral tilting is more readily initiated, resulting in the deformation of the overall matrix configuration. Glazer summarized that the octahedra could tilt around three orthogonal axes, leading to changes in the lattice parameters post tilting as follows: $a_1 = \xi \cos{(\beta)} \cos{(\gamma)}$; $b_1 = \xi \cos{(\alpha)} \cos{(\gamma)}$ and $c_1 = \xi \cos{(\alpha)} \cos{(\beta)}$, in this model, α , β and γ signify the angles of octahedral tilt relative to the a-, b- and caxis, respectively.⁵⁷ The ξ represents the distance between anions traversing the centroid of the octahedron. In glazer notation, tilting solely around [001] axis suggests a tetragonal symmetry within the perovskite structure. The tetragonal symmetry is theoretically maintained as long as the tilt configurations of adjacent layers remain consistent along the axis. However, variations in tilt magnitudes or phase difference across layers can alter the overall symmetry, potentially resulting in other structural symmetries such as orthorhombic or monoclinic, Woodward refined the relationship between octahedral tilting and space classifications, detain these associations in Table

2.1.⁵⁸



Tilt system number	Tilt system symbol	Space group (Glazer)	Space group (Woodward)
Three tilt systems			
1	a+b+c+	Immm (#71)	Immm (#71)
2	a+b+b+	Immm (#71)	Immm (#71)
3	a†a†a†	lm3 (#204)	lm3 (#204)
4	a+b+c-	Pmmn (#59)	Pmmn (#59)
5	a⁺a⁺c⁻	Pmmn (#59)	Pmmn (#59)
6	a⁺b⁺b⁻	Pmmn (#59)	Pmmn (#59)
7	a⁺a⁺a⁻	Pmmn (#59)	Pmmn (#59)
8	a+b-c-	A2 ₁ /m11 (#11)	P2₁/m (#11-1)
9	a⁺a⁻c⁻	A2 ₁ /m11 (#11)	P2 ₁ /m (#11-1)
10	a⁺b⁻b⁻	Pmnb (#62)	Pnma (#62)
11	a+a-a-	Pmnb (#62)	Pnma (#62)
12	a ⁻ b ⁻ c ⁻	F1 (#2)	F1 (#2)
13	a ⁻ b ⁻ b ⁻	I2/a (#15)	I2/a (#15-3)
14	a-a-a-	R3c (#167)	R3c (#167-2)
Two tilt systems			
15	a⁰b⁺c⁺	Immm (#71)	Immm (#71)
16	$a^0b^+b^+$	I4/mmm (#139)	I4/mmm (#139)
17	a ⁰ b⁺c⁻	Bmmb (#63)	Pmmn (#59-2)
18	a⁰b⁺b⁻	Bmmb (#63)	Pmmn (#59-2)
19	a ⁰ b⁻c⁻	F2/m11 (#12)	I2/m (#12-3)
20	a ^o b-b-	Imcm (#74)	Imma (#74)
One tilt systems			
21	а ⁰ а ⁰ с+	C4/mmb (#127)	P4/mbm (#127)
22	a⁰a⁰c⁻	F4/mmc (#140)	I4/mcm (#140)
Zero tilt system			
23	$a^0a^0a^0$	Pm3m (#221)	Pm3m (#221)



Table 2.1 Woodward's expansion and revision of Glazer's space group classification for perovskite tilting systems with consideration of atomic positions.⁵⁸

3D hybrid perovskites currently dominate as the primary photo-active material within the field. This class of materials employs X as a halide element and A cations, primarily FA and MA. Among the various choices for the B site, lead is the most commonly utilized for harvesting the solar energy.⁵⁹ Hybrid perovskites featuring MA as the primary cation demonstrate superior electronic properties and have attracted research interest regarding their ferroelectric and ferro-elastic properties. This interest is attributed to the tetragonal crystal structure, which, influenced by a relatively small tolerance factor (~0.912)⁶⁰ and consequent single-octahedral tilting, results in a lower symmetry configuration of the material, potentially inducing a permanent dipole moment. 61, 62 Compared to the larger bandgap of MAPbI₃ (~1.55 eV), 12 FAPbI₃ exhibit a narrower bandgap (~1.48 eV),12, 20 indicating potential enhancements in light absorption capabilities suitable for solar applications. MAPbI₃ undergoes a series of transitions influenced by temperature-induced lattice dynamics. At approximately 170 K, the material transitions from an orthorhombic structure (Pnma, #62)⁶³ to a tetragonal phase (*I4/mcm*, #140). As the temperature increases to about 327



K, MAPbI₃ further transitions from the tetragonal to a cubic phase $(Pm\overline{3}m, \#221)$.⁶⁴ These transformations are attributed to thermal expansion which facilitates a progressive change in the tilting of the octahedral units within the crystal structure-from bi-axial tilting in the orthorhombic phase, to a single-axis tilting in the tetragonal phase, and finally to an absence of tilting in the cubic phase which also suit perfectly to Woodward's definition in **Table 2**.

The near-room-temperature shift from tetragonal to cubic in MAPbI₃ can compromise device stability, leading to structural issues that impact their performance and durability. FAPbI₃ demonstrates superior thermal stability relative to MAPbI₃, which can be ascribed to its larger tolerance factor (\sim 1.036). However, at room temperature, FAPbI₃ undergoes a transition to a non-perovskite phase where the octahedra share faces, as shown in **Figure 2.1d**. This configurations represents the most stable phase of FAPbI₃ at this temperature, ⁶⁵ therefore, it is challenging to completely eliminate the δ phase (2H configuration), which is directly associated with the degradation of the device's performance.

2.2 Hybrid perovskite synthesis and fabrication

2.2.1 Antisolvent engineering



Considerable research endeavors have been undertaken to inhibit the formation of the δ phase during the fabrication of FAPbI₃ devices, encompassing strategies such as anti-solvent techniques, incorporation of chemical additives, and the adoption of two-step fabrication methodologies. ⁶⁶

Antisolvents trigger quick, dense nucleation in perovskite films, creating smooth, defect-free layers.⁶⁷ Alternative techniques such as additive engineering enhance film quality by moderating crystallization rates or conducting defect passivation, thus boosting the film's crystallinity and optoelectronic properties.⁶⁸ The two-step fabrication method effectively reduces the delta phase in FAPbI₃ by separating the deposition of lead iodide (PbI₂) and its conversion to perovskite with formamidinium iodide (FAI).³⁴

Common solvents such as Dimethyl Sulfoxide (DMSO), Dimethylformamide (DMF), Acetonitrile (ACN), Gamma-Butyrolactone (GBL), and Dimethylacetamide (DMA) are widely used in the fabrication of hybrid perovskite precursors due to their excellent dissolubility suitable boiling points and coordination properties.⁶⁹ The selection of an antisolvent should be closely related to the choice of the precursor solvent, primarily dependent on the solubility of the organic precursors in the antisolvent, as well as the miscibility of the antisolvent with the precursor solvent. These factors synergistically



modulate the rate-dependent dynamics during the application of the antisolvent.⁷⁰ Polarity and boiling point are commonly used as criteria for selecting antisolvents, with the parameters for common antisolvents summarized in **Table 2.2**. In line with the principle of 'like dissolves like,' the polarity of an antisolvent should significantly differ from that of the precursor solvent to facilitate rapid crystallization of the perovskite. Additionally, the boiling point of the antisolvent should be optimally chosen to avoid

Solvent	Boiling point [°C]	Dipole moment [D]
Ethanol (EtOH)	78	1.69
Isopropyl Alcohol (IPA)	83	1.66
Butyl Alcohol (BuOH)	118	1.66
Ethyl Acetate (EA)	77	1.78
Chloroform (CF)	61	1.15
Chlorobenzene (CB)	131	1.69
Butyl Acetate (BA)	126	1.87
Dichlorobenzene (DCB)	180	2.50
Anisole (Ani)	154	2.30
Trifluorotoluene (TFT)	103	2.86
Diethyl Ether (DEE)	35	1.15
Xylene (XyL)	139	0.33-0.37
Toluene (Tol)	111	0.36
Mesitylene (Mesit)	164.7	0.047

Table 2. 2 Information on common antisolvents including boiling points and



dipole moments.⁷⁰

extremes, ensuring uniform film formation by preventing premature evaporation while allowing sufficient time for the solvent to act effectively. Due to DMF's dipole moment of 3.62D,⁷¹ CB, with a dipole moment of 1.6D and a boiling point 131°C,⁷² provides sufficient time for the extension during spin coating. This makes it an appropriate and the most common antisolvent when DMF is used as the precursor solvent.⁷³

2.2.2 Additive engineering

In the fabrication of FAPbI₃ perovskite solar cells, additives play crucial roles in enhancing film morphology, crystallinity, and overall device stability. The underlying mechanisms through which these additives exert their beneficial effects can be grouped into several categories: defect passivation, crystallization control, grain boundary engineering, and phase stabilization.⁶⁷

Additives such as fullerene derivatives (e.g., PCBM)⁷⁴ and alkali metal halides (e.g., KCl, CsCl) ⁷⁵ are known to effectively passivate defects within the perovskite structure. These defects, which include vacancies, interstitials, and grain boundary defects, can act as non-radiative recombination centers, significantly reducing the photovoltaic



performance of the device. By passivating these defects, additives can reduce charge recombination losses, leading to higher power conversion efficiencies (PCE).

The incorporation of additives like chlorides (e.g., PbCl₂)⁷⁶ and organic molecules (e.g., methylammonium chloride, MACl)⁷⁷ can influence the crystallization process of the perovskite film. These additives can modify the nucleation and growth kinetics, resulting in larger and more uniform grain sizes. This enhancement in grain size is critical for improving charge transport properties and reducing grain boundary recombination.

Additives can also play a significant role in engineering the grain boundaries of the perovskite films. For instance, polymers such as polyethylene glycol (PEG)⁷⁸ and polyvinylpyrrolidone (PVP)⁷⁹ can be used to passivate and stabilize grain boundaries. This not only improves the mechanical integrity of the films but also reduces the density of trap states at the grain boundaries, thereby enhancing the overall device performance.

FAPbI₃ is prone to phase instability, where it can transform from its photoactive black phase (α) to the non-photoactive yellow phase (δ). Additives such as guanidinium (GA)⁸⁰ and certain alkali metal ions (e.g., Rb⁺, Cs⁺)⁸¹ can stabilize the black phase by incorporating into the perovskite lattice or by forming secondary phases that promote



the stability of the desired α phase. This stabilization is crucial for maintaining high device performance over time.

2.2.3 Single crystal bulk and thin film hybrid perovskite

The synthesis of single crystal FAPbI₃ in both bulk and thin film forms have attracted significant attention due to their superior properties, including high crystallinity, low defect density, and excellent charge transport capabilities. These attributes are crucial for enhancing the performance of optoelectronic devices such as solar cells, LEDs, and photodetectors, as well as deepening the understanding of perovskite structures.⁸² Achieving high-quality single crystals and thin films depends heavily on advanced synthesis methods, particularly ITC, antisolvent engineering, and the space-confined method.⁸³

In the realm of perovskite synthesis, ITC leverages the unique solubility behavior of perovskite precursors, where solubility decreases with increasing temperature.⁸⁴ As described in **Figure 2.3a** Han and colleagues describe the synthesis of single crystal FAPbI₃ using ITC method in GBL solvent. Initially, seed crystals are formed through a cooling solution method. These seed crystals are then placed in a GBL precursor solution and subjected to precise temperature at 100°C to grow larger single crystals. This method yields high-quality crystals with minimal defects; however, the



temperature rate must be meticulously regulated to ensure the formation of a pure phase α -FAPbI₃ single crystal, necessitating a growth process that is as slow and controlled as possible. 85

Antisolvent engineering is also employed in the synthesis of perovskite single crystals. During the crystallization process, an antisolvent such as CB or toluene is introduced into the perovskite precursor solution. ⁸⁶ This approach facilitates the synthesis of single crystals at room temperature, thereby reducing potential lattice strain that may arise from the high-to-low temperature transitions inherent in the ITC method.

The space-confined method involves confining the perovskite precursor solution between two substrates though, limiting the space available for crystal growth and promoting the formation of thin, continuous single-crystal thin films. Studies have demonstrated that hydrophobic interfaces facilitate the dispersion of precursors and the growth of single crystals within confined environments. For example, as illustrated in **Figure 2.3b**, the application of a poly(triarylamine) (PTAA) coating on the interface significantly enhances these processes.⁸⁷ The confinement induced by capillary action and the inherent weight of the top substrate generally results in relatively thick films, typically exceeding 1 µm.⁸⁸ To achieve thinner single crystal films, researchers have



applied additional pressure, as illustrated in **Figure 2.3c**, successfully obtaining single crystal thin films with thicknesses reduced to the tens of nanometers scale.⁸⁹

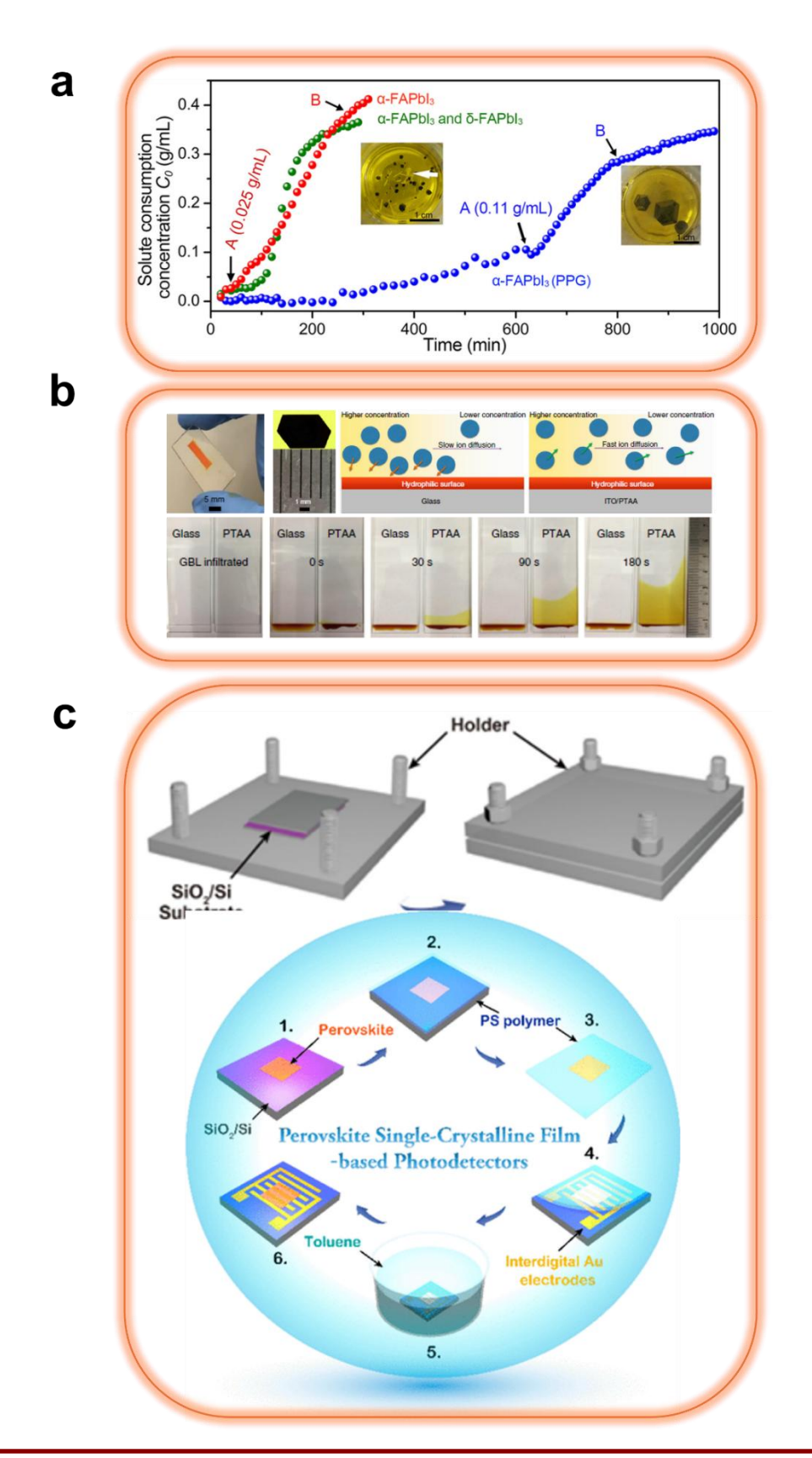




Figure 2.3 Progressive stages in the development of single crystal perovskite bulk and thin film synthesis. (a) Time-dependent inverse-temperature crystallization of α-FAPbI₃. ⁸⁵ (b) Surface hydrophobic modification for single crystal MAPbI₃ and MAPbBr₃ thin film using space confined and inverse temperature method. ⁸⁷ (c) Pressure-induced MAPbBr₃ single crystal thin film synthesis with ultra-thin film thickness combining space confined and inverse temperature method. ⁸⁹

2.3 Structural and dynamic investigation of hybrid perovskite

2.3.1 TEM analysis on MAPbI₃ and FAPbI₃

TEM coupling with SAED is a powerful tool used to investigate the structural properties of materials at the atomic scale. In the field of perovskite solar cells, understanding the microstructure of materials like FAPbI₃ and MAPbI₃ is crucial for optimizing their performance and stability.

The conventional high-resolution imaging approach has been recognized as a direct cause of the perovskite-to-PbI₂ transition in FAPbI₃ and MAPbI₃, 88 owing to the



susceptibility of their organic components to beam-induced damage. TEM operates by transmitting electrons through a thin sample to produce high-resolution images of the internal structure. SAED, employed alongside TEM, focuses on a localized region of the sample, generating a diffraction pattern from scattered electrons to elucidate the crystal structure and orientation while minimizing electron exposure. As a result, in recent years, SAED has increasingly superseded high-resolution transmission electron microscopy (HRTEM) for the structural characterization of organic perovskites due to its reduced beam damage. 91, 92

MAPbI₃ primarily exhibits a tetragonal phase at room temperature. When heated, it transitions to a cubic phase, while cooling induces the formation of a low-temperature orthorhombic phase. Rothmann et al. successfully achieved direct visualization of MAPbI₃ by employing spin coating of the MAPbI₃ precursor onto thin carbon-coated TEM grids. Utilizing TEM bright-field imaging, they identified the presence of twin domains within the MAPbI₃ structure for the first time. These findings were further substantiated by SAED analysis, which revealed the splitting of the 110 diffraction spots, thereby confirming the 112 plane as the twin plane as depicted in **Figure 2.4**. MAPbI₃ is highly sensitive to electron beam irradiation, with significant changes occurring at low doses. Key structural changes include the loss of twin domains and the formation of a $\sqrt{2} \times \sqrt{2}$ supercell, followed by transformation into lead iodide with



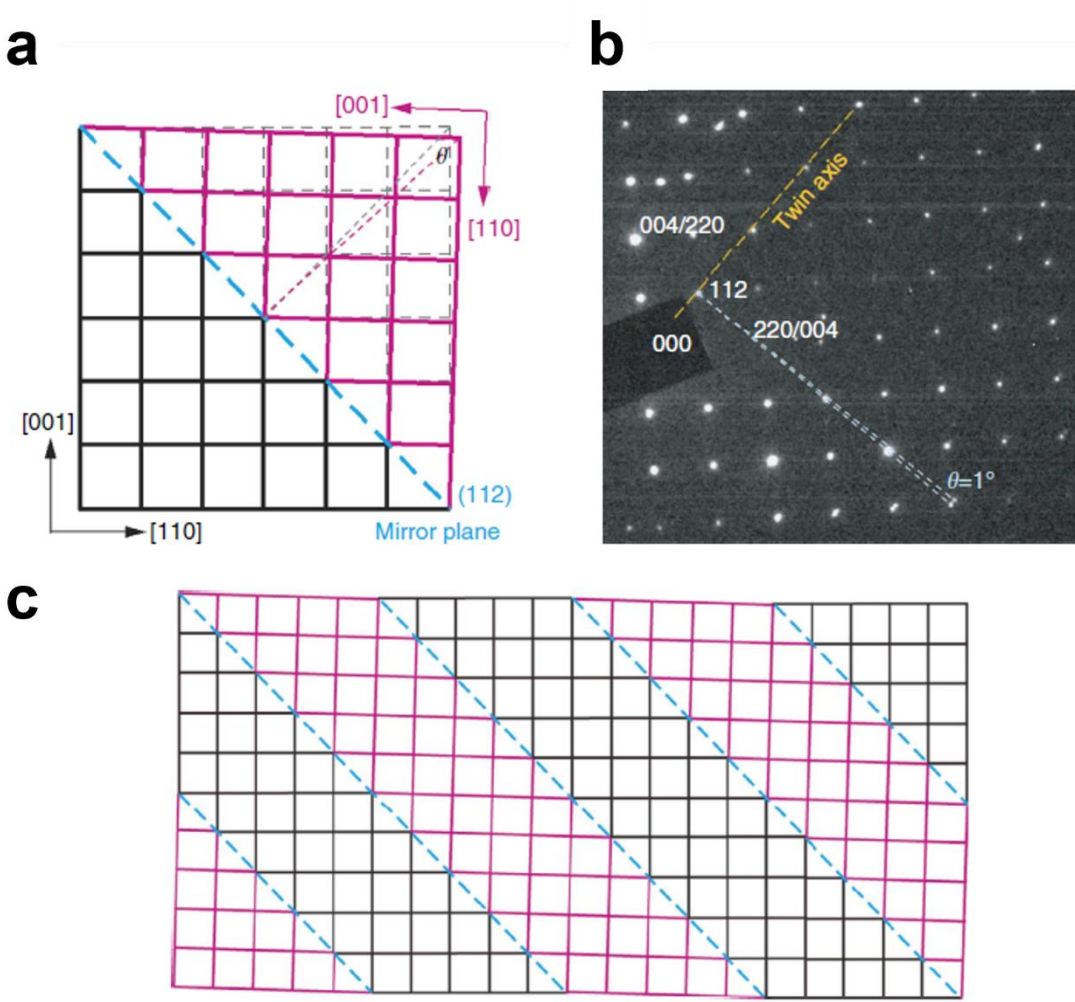


Figure 2.4 Twinning model and actual SAED pattern of MAPbI₃. (a) Description of the twin-domain structure in zone axis [1 $\overline{10}$]. (b) SAED pattern of [1 $\overline{10}$] oriented MAPbI₃ twin with θ =1° point split at the 220-diffraction spot. c) Schematic model of the continuous {112} twin structure.⁹³

increased electron exposure.^{90, 94} The electron-sensitive nature of organic perovskites necessitates meticulous care when utilizing electron microscopy for their study. Similarly, the versatile material FAPbI₃ is also subject to challenges arising from electron sensitivity.



Twinning on the {111} plane in FCC structures is a well-documented phenomenon, commonly observed in materials such as copper (Cu),⁹⁵ silver (Ag),⁹⁶ and other FCC metals. This type of twinning occurs frequently due to the high symmetry and close-packed nature of the {111} plane in FCC crystals, playing a significant role in the mechanical behavior and microstructural evolution of these materials. Similarly, {111} twinning and stacking faults have been extensively characterized in FAPbI₃ using TEM and SAED techniques.^{26, 27, 97}

Li et al. identified that the slight misfit in the geometric configuration of FAPbI₃ in the cubic (α) phase results in a high density of stacking faults. Their research demonstrated that doping with MA effectively alleviates these stacking faults, as evidenced by the gradual disappearance of streaks along the {111} twin plane with increasing MA content. Additionally, the persistent issue of hysteresis was found to be proportional to the amount of stacking faults present.²⁷

In summary, the passage highlights the effectiveness of TEM and SAED in analyzing the microstructure of FAPbI₃ and MAPbI₃ in perovskite solar cells, emphasizing the reduced beam damage with SAED and the detailed structural insights gained. It also underscores the materials' sensitivity to electron beams and the significant role of MA doping in reducing defects and improving performance.



2.3.2 Dynamic study of FAPbI₃ phase transition

Gaining a deep understanding of the kinetic processes involved in the phase transition from delta to α phase in FAPbI₃ is vital for advancing perovskite solar cell technology. The α phase, noted for its excellent photovoltaic properties, plays a crucial role in the overall efficiency and long-term stability of these devices. Being able to master the kinetics of this phase transition could lead to substantial advancements in the field. In industrial settings, the precise control and stabilization of the α phase during production are crucial.⁹⁸

XRD, augmented by GIWAXS, constitutes an essential analytical paradigm for probing crystallographic transformations during material phase transitions.³⁸ Through rigorous analysis of diffraction patterns and GIWAXS data, this technique enables the precise quantification of modifications in lattice parameters and symmetry, thus providing a detailed elucidation of the structural dynamics central to phase transitions. Employed predominantly in real-time or *in-situ* settings, XRD facilitates uninterrupted observation of structural evolution, capturing subtle changes under controlled environmental variables such as temperature and pressure gradients.^{33, 99, 100}

Building on the microscopic structural insights provided by XRD, *in-situ* optical microscopy offers a complementary observational modality for phase transition



studies.^{30, 40} It enables the direct visual assessment of textural, morphological, and chromatic changes at the microscale during transitions. This technique is particularly adept at monitoring the kinetics of phase boundary movements and the genesis of new phases. Enhancements through polarized light microscopy further augment its capability to detail the anisotropic properties of materials undergoing phase transformations, providing a richer understanding of the material behavior.

Concurrently, Differential Scanning Calorimetry (DSC) quantitatively measures the thermal energy exchange associated with material phase changes under various thermal conditions—whether heating, cooling, or isothermal. Specializing in the detection and quantification of first-order transitions, DSC identifies characteristic endothermic or exothermic peaks within the calorimetric curve. These peaks yield essential thermodynamic data, such as transition temperatures and changes in enthalpy, offering a robust quantitative framework that complements the structural and visual data provided by XRD and optical microscopy. Collectively, these techniques furnish a comprehensive multi-scale perspective on the dynamic phenomena occurring during phase transitions in materials. Security of the security of the dynamic phenomena occurring during

The JMA model, also known as the Avrami equation, is a fundamental approach used in materials science to describe the kinetics of phase transformations, particularly non-



equilibrium transformations such as crystallization and the growth of new phases.¹⁰² This model is extensively used to analyze the kinetics of transformations in solids that are not instantaneous but rather occur over a period as a function of temperature and time.

The JMA model is expressed mathematically as: $X(t) = 1 - e^{-k \cdot t^n}$. Where X(t) is the fraction of the material transformed at time t; k is a rate constant that incorporates temperature and material properties; n is the Avrami exponent, which provides insight into the mechanism and dimensions of growth; t is time. In the context of sporadic nucleation, the Avrami exponent n takes on specific values depending on the growth dimensionality: n=2 for needle-like (1D) growth, n=3 for plate-like (2D) growth, and n=4 for spherical (3D) growth. Conversely, for instantaneous nucleation, the values shift to n=1 for needle-like growth, n=2 for plate-like growth, and n=3 for spherical growth. The term 'hard impingement' describes the cessation of growth when grains intersect in a particular direction. n=1

In conclusion, mastering the kinetics of the delta to α phase transition in FAPbI₃ is crucial for enhancing the performance and stability of perovskite solar cells. By deeply understanding the structural and thermodynamic changes during the phase transition and employing models to quantitatively describe the kinetics, precise control of the



phase can be achieved. This advancement is pivotal for driving significant progress in perovskite solar cell technology.



Chapter 3 Anisotropic δ -to- α phase transition in Formamidinium Lead Iodide thin films

3.1 Introduction

Hybrid perovskites based on FAPbI₃ have been recognized as one of the most promising candidates for next-generation solar cells with exceptionally high efficiency and lower cost. Owing to the instability of the cubic perovskite structure inherited from the large ionic radius of NH₂CH=NH₂⁺ (FA⁺), at room temperature FAPbI₃ tends to form a hexagonal non-perovskite structure (δ-FAPbI₃ or yellow phase)¹⁰⁴ without photoactivity. Thermal annealing is usually required to induce phase transition and to achieve the photoactive cubic phase (α-FAPbI₃ or black phase), ¹⁰⁵ which can be maintained down to room temperature for solar cell applications. A plethora of works have been demonstrated to prepare high-quality α-FAPbI₃ materials with record-high power conversion efficiencies (PCEs) based on such annealing-induced δ -to- α phase transition. ^{22, 25, 99, 106-110} Due to its critical impact on solar-cell performance, significant efforts have been made to optimize the annealing process. For example, radiativeassisted thermal annealing has been developed to achieve more efficient phase transition, which can obtain purer α-FAPbI₃ with less annealing time.²⁹ Atmosphere



control during annealing has also been established as an effective approach to lower the δ -to- α transition barrier and to improve crystal quality of α -FAPbI₃.^{22, 111} Moreover, higher δ -FAPbI₃ crystallinity prior to annealing can promote the formation of α -FAPbI₃ with larger grains and more aligned orientation, leading to enhanced performance of FAPbI₃-based solar cells.^{108, 109}

Despite its vital role on the quality and performance of solar cells, however, the fundamental mechanism of δ-to-α phase transition in FAPbI₃ remains unclear. Sánchez et al. examined the impact of heating rate on δ-to-α transition in polycrystalline FAPbI₃ films using X-ray diffraction (XRD) and differential scanning calorimetry, but without microscopic observation to reveal the phase transition process.³⁹ Lai et al. have applied pioneering in situ optical microscopy on δ -to- α phase transition in FAPbI₃, showing its lower activation energy than inorganic perovskites. Nevertheless, the observation was limited to one-dimensional (1D) FAPbI₃ microwires only, which is very different from FAPbI₃ films used in solar cells. The limited resolution of optical microscopy is also incapable of revealing the detailed structure and morphology at the transition front, leaving a significant knowledge gap hampering the understanding of the phase transition mechanism. In this work, we demonstrate multiscale microscopic observation on δ-to-α phase transition in FAPbI₃ thin films that are more relevant to solar cell devices. In particular, we prepare epitaxial δ-FAPbI₃ thin films with well-defined



orientation for this mechanistic study. To better detect the phase transition process, we adopt polarized light microscopy (PLM) that offers enhanced contrast between isotropic α -FAPbI3 and anisotropic δ -FAPbI3. Facilitated by *in situ* heating, it enables the observation of heterogeneous nucleation of α -FAPbI3 and the subsequent anisotropic δ -to- α phase transition underpinned by the lower kinetic energy barrier along <0001>. We further reveal the morphology and orientation relationship at the δ -to- α transition front using 4D scanning transmission electron microscopy (4D-STEM).

By reconstructing dark-field images from specific diffraction spots, delta and alpha phases can be effectively distinguished, unlike conventional bright-field (BF) or dark-field (DF) imaging. Additionally, 4D-STEM enables the investigation of large-area interfaces with an ultralow electron dose. On the other hand, bright-field images reconstructed from non-diffracted beams provide excellent contrast for defect detection in α -FAPbI₃. The presence of high-density planar defects is also unveiled at the transition front, which may promote the structure transformation between δ - and α -FAPbI₃.

3.2 Material preparation and characterization

3.2.1 Synthesis of single crystal bulk prism δ-FAPbI₃



The single crystal δ-FAPbI₃ prism was synthesized utilizing the anti-solvent method.³⁶

To begin with, 1.6 M solution of both Formamidinium iodide (FAI, Sigma-Aldrich) and PbI₂ (Sigma-Aldrich) were prepared by dissolving them in 1 ml of γ -Butyrolactone (GBL, Sigma-Aldrich), with the mixture subjected to continuous magnetic stirring overnight. The clear solution was then filtered through a 2 mm filter head and subsequently set aside for further use.

1 ml of chlorobenzene (CB, Sigma-Aldrich) was placed into a vial, the top of which had been drilled with a 2 mm hole; the same operation was repeated for the precursor solution that had been obtained previously. The vial containing the anti-solvent, alongside the vial containing the precursor, was enclosed within a sealed 200 ml vial situated inside a glove box under an N_2 atmosphere where H_2O and O_2 levels were maintained below 0.1 ppm. Designed to facilitate a gradual diffusion process, the setup was left undisturbed for over 72 hours, allowing the anti-solvent to slowly permeate into the precursor. Following this period, the distinct δ -FAPbI₃ prism that had formed was carefully collected, delicately wiped with lint-free paper, and stored within the glove box in preparation for further application.

3.2.2 Synthesis of epitaxial δ-FAPbI₃ thin film

As illustrated in Figure 3.3, a 3 µl aliquot of the precursor solution was carefully



introduced into the interstitial space formed by aligning two octadecyltrichlorosilane (OTS, Sigma Aldrich)-treated Si/SiO₂ slices in a face-to-face configuration. The assembly was left undisturbed for 10 minutes to allow homogeneous precursor diffusion across the substrate interface via capillary action. The assembled slices were subjected to a self-designed pressure setup and sealed with chlorobenzene (CB, Sigma-Aldrich) as an antisolvent. The crystal growth process was conducted over seven days, after which the slices were separated using a knife. All procedures were performed in an N₂-filled glovebox to avoid exposure to H₂O and O₂.

3.2.3 Transfer of FAPbI₃ thin film onto TEM grid

Polystyrene (PS, Mw \sim 35,000, Sigma Aldrich) was dissolved in chlorobenzene at 10 mg/ml. A 30 μ l aliquot was deposited onto the thin film and spin-coated at 600 rpm. After drying in a glovebox for 30 minutes, the PS layer was carefully lifted with tweezers, transferred onto a legacy TEM grid, and rinsed with CB to remove residual PS.

3.2.4 X-ray Diffraction (XRD)

A Rigaku SmartLab (9 kW, $\lambda \sim 1.54$ Å) was employed for measurements. Optical alignment and sample height adjustments were performed to correct omega offset and



enhance signal contrast. The rocking curve of δ -FAPbI₃ was measured at $2\theta = 11.78^{\circ}$ using the 2θ -omega scan method.

3.2.5 *In-situ* optical polarized microscopy

The as-synthesized single crystal thin film, which was encapsulated within an *in-situ* annealing setup specifically configured for optical observation, was also utilized to facilitate the transfer of the sample from the glove box to the microscope, employing a Leica DM2700M microscope equipped with polarizer and analyzer elements that were in a perpendicular configuration during testing. During the observation period, video data capture was sustained at a rate of one frame per second. Simultaneously, the temperature ramp was regulated to increase at a steady pace of 50°C per minute, ensuring that the thermal conditions remained controlled and consistent throughout the experiment.

3.2.6 Confocal PL

Confocal PL measurements were performed using a Witec confocal microscope that was equipped with an Ar ion laser (~532 nm) as the excitation source, the power of which was reduced to 0.06 mW, a large-scale scan was performed across a region measuring tens of square micrometers, utilizing a resolution defined by a 120x120 pixel



matrix. In addition, the in-situ annealing setup previously described was employed during these measurements to ensure that the perovskite sample remained protected from air exposure.

3.2.7 Transmission electron microscopy (TEM)

The as-prepared single crystal thin film TEM sample was carefully encapsulated within a dry box to ensure an anhydrous environment prior to its transfer into the analytical chamber of the Jeol-2100F electron microscope, which operates with an accelerating voltage of 200 kV. The duration for loading the sample into the microscope was rigorously controlled and limited to a maximum of two minutes to minimize exposure to potential environmental contaminants. Data acquisition for SAED and TEM was conducted with the sample in a fixed orientation, without any tilting, to ensure consistent and reliable imaging across the experiments.

3.2.8 4D-STEM

The 4D-STEM datasets were acquired using an EMPAD on a ThermoFisher Scientific Spectra 300 microscope operated at 300 kV. It was conducted with a small convergence semi-angle of 110 μ rad, a beam current of 1 pA, and an exposure time of 1 ms to achieve the low-dose condition to probe the pristine structure of FAPbI₃.



3.2.9 Density functional theory (DFT) calculations

The DFT calculations were performed using the projector-augmented wave (PAW) method, as implemented in the Vienna Ab initio Simulation Package (VASP). $^{112,\,113}$ The generalized gradient approximation (GGA) in conjunction with the Perdew-Burke-Ernzerhof (PBE) exchange correlation functional was employed. The van der Waals (vdW) interactions were incorporated during structural optimization through the zero-damping method of Grimme (DFT-D3). 114 For the optimization of the crystal structures of the α - and δ -phase FAPbI3 bulk and slabs, a Γ -centered grid with a k-point density of 0.25 Å⁻¹ and Gaussian smearing with a width of 0.05 eV were used. The energy cutoffs of the wavefunctions were set at 500 eV. To avoid interactions between periodic layers, the slab models were placed in the middle of crystals and were separated by vacuum layers of 10 Å at both the top and bottom. The structural optimizations were considered convergent when the force on each atom was less than 0.01 eV/Å.

The FAPbI₃ slabs were constructed to simulate the crystalline surfaces along the $\{001\}$, $\{110\}$, $\{111\}$ and $\{210\}$ crystallographic orientation for the α -FAPbI₃, and along the $\{0002\}$, $\{10\overline{1}0\}$ and $\{2\overline{1}\overline{1}0\}$ crystallographic orientation for the δ -FAPbI₃. The surface energy (σ) was calculated by the following equation:

$$\sigma = \frac{1}{2A} \left\{ \left(E_{slab}^{unrel} - nE_{bulk} \right) + \left(E_{slab}^{rel} - E_{slab}^{unrel} \right) \right\}$$



where A is the surface area; E_{slab}^{unrel} and E_{slab}^{rel} are the energies of the unrelaxed and relaxed slabs, respectively; E_{bulk} is the energy of the bulk α -FAPbI₃ and δ -FAPbI₃ structure; and n is the exact number of FAPbI₃ units in slab models.

3.3 Results and discussion

3.3.1 Single crystal δ-FAPbI₃ prism

The single crystal δ -FAPbI₃ prism, exhibiting a red-brown color, was synthesized using the antisolvent method as described in **Section 4.2**. As shown in **Figure 4.1a**, photos from the top side reveal a six-fold symmetry and a flat top facet, indicative of a hexagonal crystallographic configuration. Upon annealing at 150°C for an adequate duration, the crystal transforms into black. This transformation is confirmed by steady-state PL spectra, with the main peak at 821 nm (band gap \sim 1.51 eV) aligning with the optical properties of α -FAPI₃. An additional minor peak at 796.5 nm (band gap \sim 1.55 eV) suggests that the phase transition in the single crystal may introduce numerous defects.

The conventional hexagonal configuration of FAPbI₃ can exist in forms such as 2H (δ -FAPbI₃), 4H, or 6H, all of which can convert to 3C upon annealing ¹¹⁵. Conventional XRD using the θ -2 θ method measures only the lattice vectors perpendicular to the



substrate. Accordingly, the single crystal prism was aligned and mounted on the equipment substrate as described in the **Section 4.2**, allowing for the examination of each facet, including the corner lattice, was examined. As depicted in **Figure 4.1c**, the side facet corresponds to $\{10\overline{1}0\}_{\delta}$ with no other peaks present. After chi tilting to 30°, the corner lattice is clearly assigned to $\{1\overline{2}10\}_{\delta}$. Further tilting chi to 60° yields an equivalent $\{10\overline{1}0\}_{\delta}$, indicating the 2H configuration. Additional tilting, targeting the top side, confirms that the top facet corresponds to $\{0002\}_{\delta}$, as presented in **Figure 4.1** d.

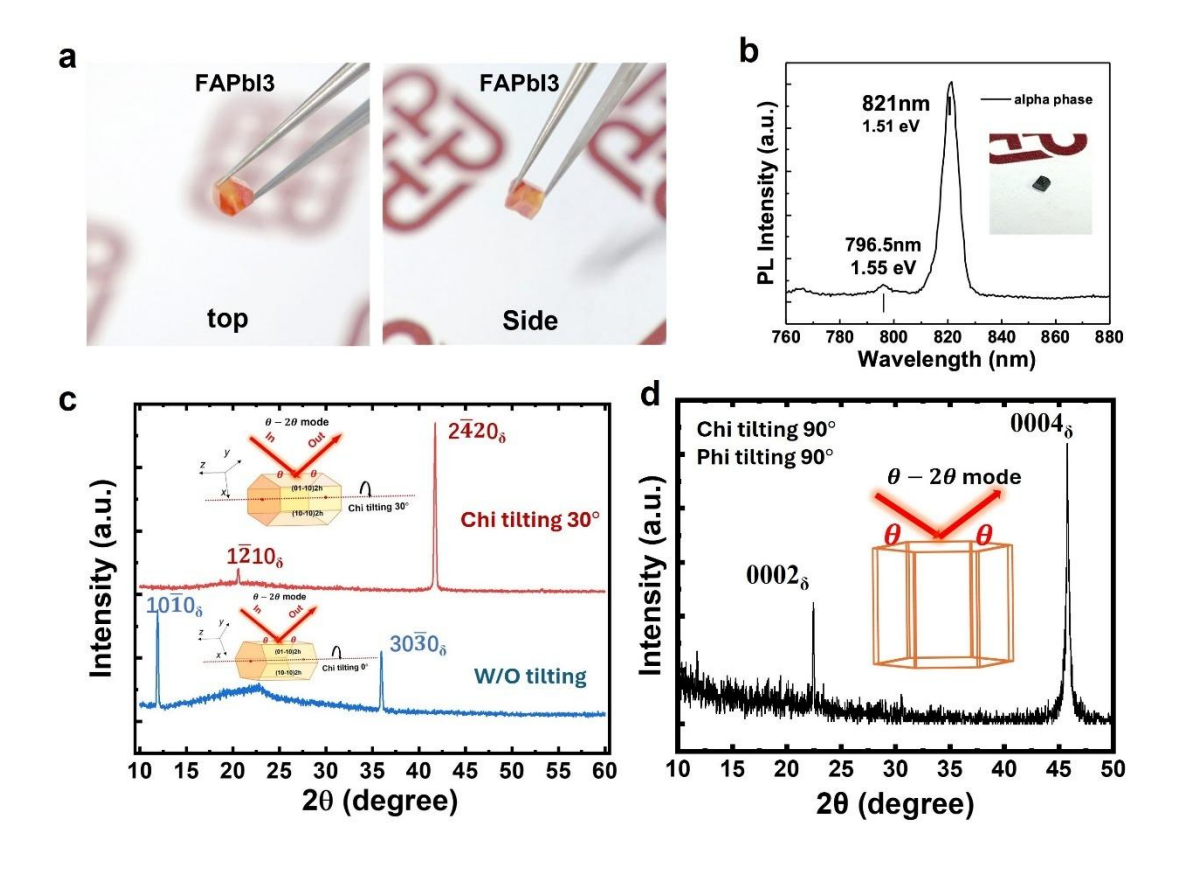


Figure 3. 1 Characterization of single crystal δ-FAPbI₃ prism. (a) optical image from both top and side perspectives of the obtained δ-FAPbI₃ prism. (b) PL spectra for the



black prism (after annealing). The inset image depicts the black crystal after being adequately annealed at 150°C. (c) XRD patterns obtained by solely tilting the chi angle from 0° to 30°, focusing on the side and corner lattice structures of the δ-FAPbI₃ prism.

(d) XRD measurement results from the top side of the crystal, with combined tilting at chi 90° and phi 90°.

Worth noting that the absence of diffraction peaks like 0001_{δ} and 0003_{δ} can indeed result from systematic extinctions due to specific symmetry elements in the crystal structure, which is normal when δ -FAPbI₃, which typically crystallizes in a hexagonal space group (P6₃/mmc, #194) 105 , reflections where l is odd may be systematically absent if there is a screw axis or glide plane parallel to the c-axis 116 .

Thus, the surface of the single crystal prism consistently exhibits a 2H (δ -FAPbI₃) configuration, at least to the depth penetrated by the X-rays. This is further supported by **Figure 4.2**, which shows the X-ray diffraction (XRD) patterns of the crystal ground into powder before and after annealing ^{117, 118}. The consistency between these patterns and the simulated diffraction data for δ - and α -FAPbI₃ indicates that this anti-solvent growth method produces phase-pure δ -FAPbI₃. Furthermore, this prism can be completely transformed into the α -FAPbI₃ undergoing a standard annealing process.



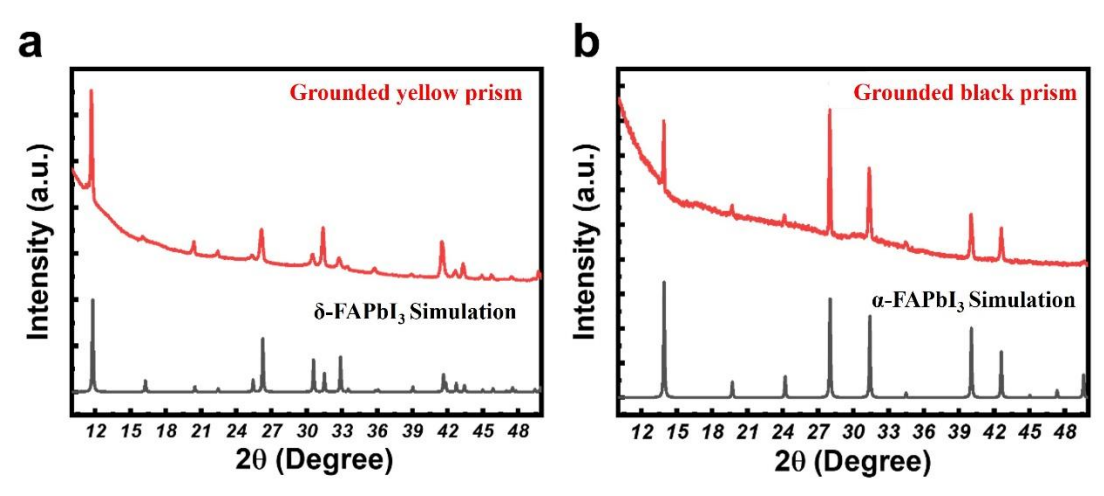


Figure 3. 2 Powder X-ray diffraction (PXRD) patterns of prism ground into powder.

(a) yellow prism, (b) black prism, compared with the simulated diffraction pattern.

3.3.2 Epitaxial δ -FAPbI₃ thin film

We prepare epitaxial δ-FAPbI₃ thin films as large as a few millimeters, using the antisolvent-assisted space-confined method at ambient temperature (see details in **Figure** 3.3).⁸⁹

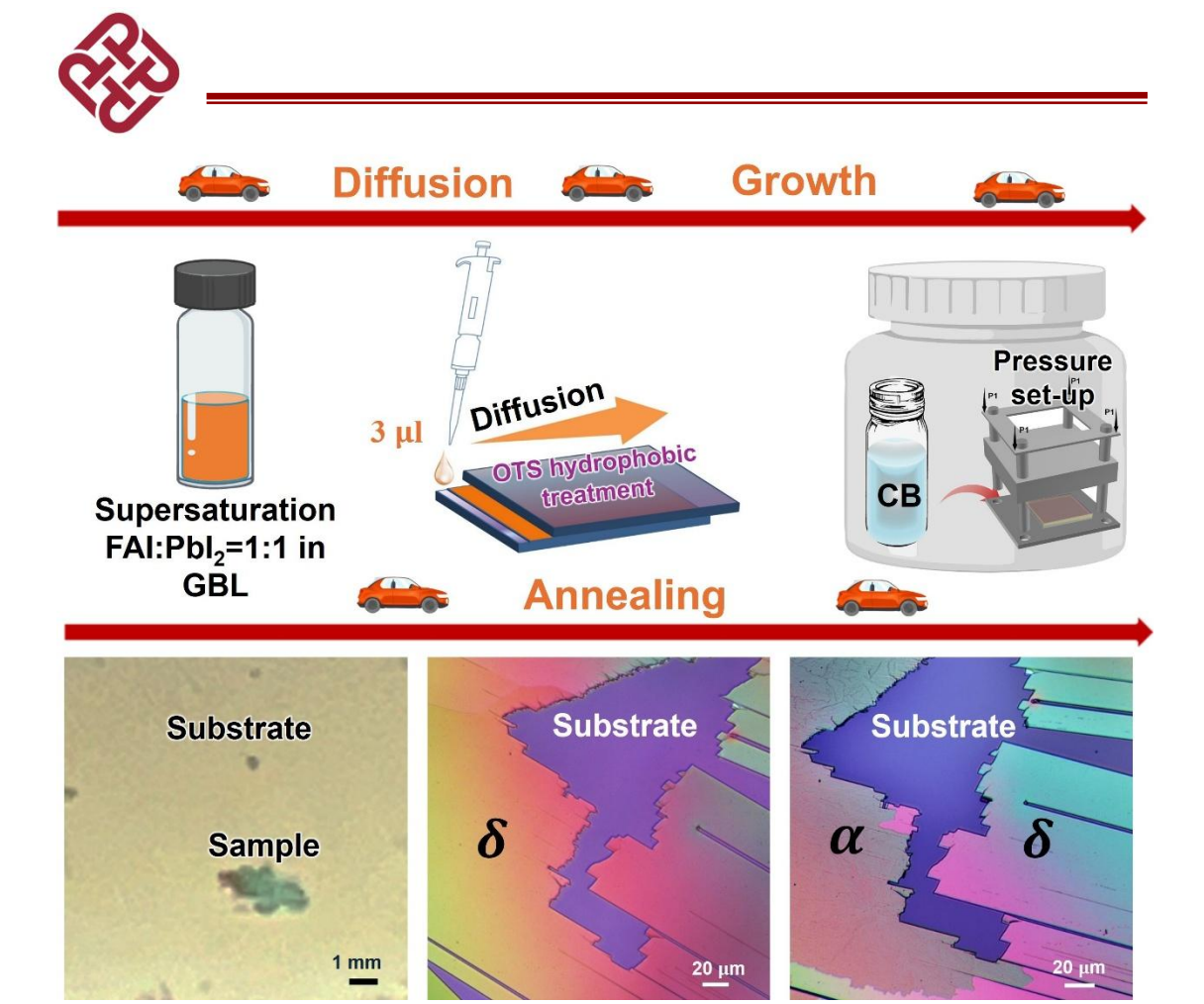


Figure 3. 3 Synthesis protocol of epitaxial δ -FAPbI $_3$ thin films using a combination of space-confined and antisolvent methods, and optical images of a film before and after annealing.

A uniform thickness of 50-100 nm can be achieved with only a few nm surface roughness as measured by profilometry and atomic force microscopy (**Figure 3.4**).



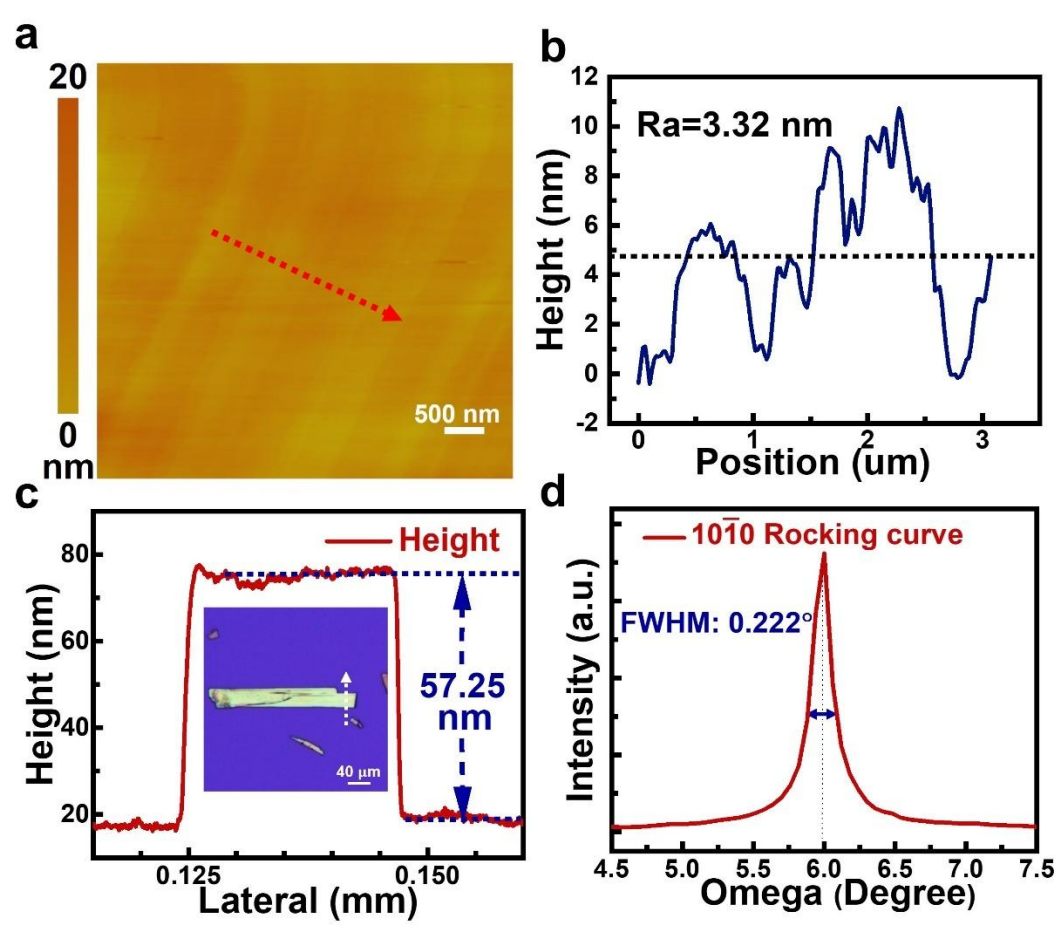


Figure 3.4 (a) AFM height map of a δ-FAPbI₃ thin film. (b) Height profile along the red arrow in A, showing a surface roughness (Ra) of 3.32 nm. (c) Profilometry thickness measurement, with the inset optical image indicating the scan direction over the sample.
(d) Rocking curve measurement on 1010 diffraction with full width at half maximum (FWHM) ~ 0.222°.

XRD evinces the high-purity δ-phase with single-crystal structure $(P6_3/mmc, #194)^{105}$ oriented along the $\{10\overline{1}0\}$ plane normal (yellow curve in **Figure 3.5a**), which has been verified by electron diffraction in the inset. The high crystalline quality of the films is



further evidenced by rocking curve measurement (**Figure 3.4d**), showing the narrow peak width comparable to bulk single crystals grown by inverse temperature crystallization (ITC) approach. ^{119, 120} Such large-scale single-crystal thin films can be transferred onto TEM grids, allowing the investigation of the phase transition behavior using both optical and electron microscopy at multiscale.

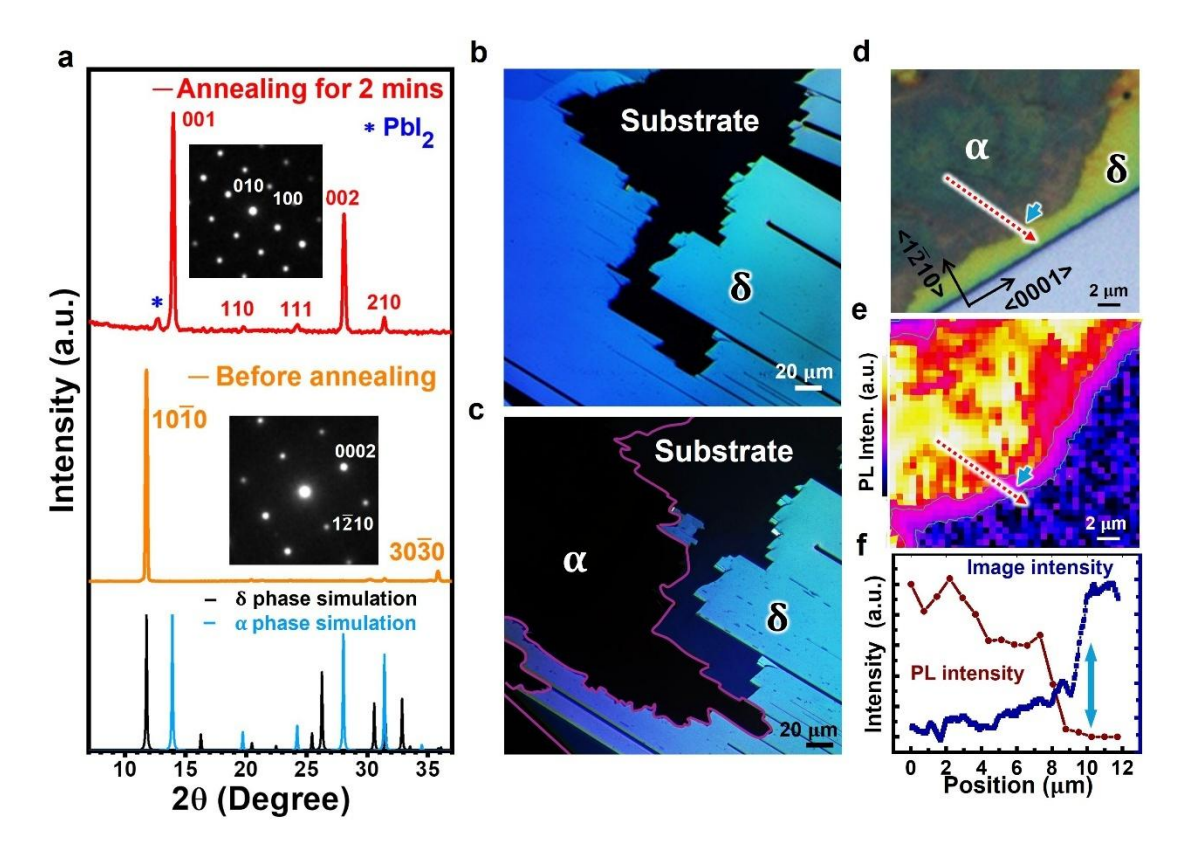


Figure 3.5 (a) Ex situ XRD of a FAPbI₃ thin film before (yellow) and after (red) annealing at 160 °C, showing δ -to- α phase transition as indicated by the reference XRD at the bottom. Insets: electron diffraction patterns taken from corresponding samples. (b,c) PLM on a FAPbI₃ thin film (b) before and (c) after annealing, showing δ -to- α phase transition at the upper-right corner. (d-f) Confocal PL mapping on a δ -to- α transition front with (d) the optical image, (e) PL intensity map from the same region,



and **(f)** PL (brown) and image intensity (blue) profiles along the red dotted arrows in **(e)** and **(d)**, respectively, with the position of the boundary indicated by the cyan arrow.

By annealing the δ -FAPbI₃ films in N₂ atmosphere, δ -to- α phase transition occurs as indicated by the dominant α -FAPbI₃ (Pm $\overline{3}$ m, #221)¹²¹ signal from XRD (red curve in **Figure 3.5a**). With the isotropic structure, α -FAPbI₃ appears dark under polarized light microscopy (PLM), which can be distinguished from the anisotropic δ -FAPbI₃ that appears bright (**Figure 3.5b and Figure 3.6**).

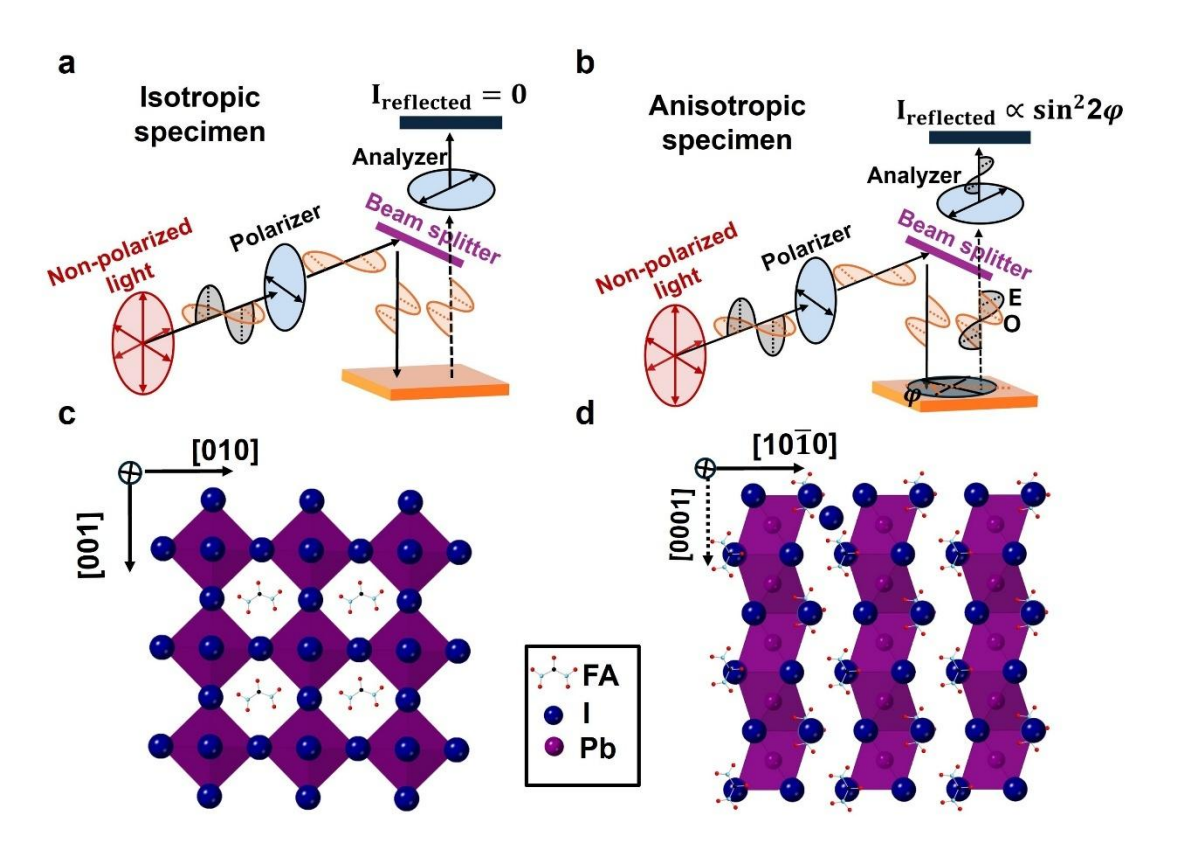


Figure 3.6 Illustration of the PLM mechanism on distinguish δ/α FAPbI₃¹²²: (a,b) Schematics showing (a) unchanged light polarization direction from an isotropic specimen, resulting in extinction in PLM, and (b) polarized light separation into



ordinary (O) and extraordinary (E) rays from an anisotropic material, showing no extinction in PLM. (c,d) Atomic structure of (c) isotropic α -FAPbI₃ and (d) anisotropic δ -FAPbI₃ with a single optical axis along the <0001> direction.

This contrast interpretation has been explicitly confirmed by photoluminescence (PL): the dark area exhibits the characteristic α -FAPbI₃ signal at \sim 800 nm, whose intensity diminishes across the boundary towards the bright δ -FAPbI₃ regions (**Figure 3.4e, f** and **Figure 3.7**).

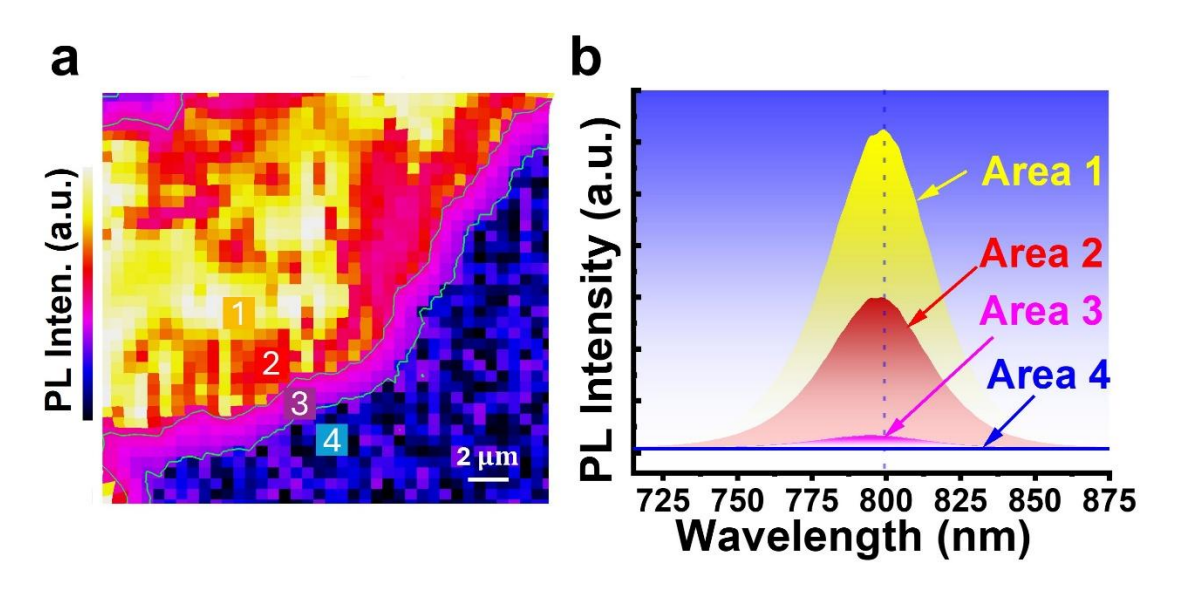


Figure 3.7 (a) Confocal PL map with the selected area highlighted. (b) Corresponding PL spectra for the indicated areas in a.

Compared to the normal optical image in **Figure 3.4d**, PLM offers substantially enhanced contrast that can be utilized to track the phase transition dynamics using *in situ* heating. **As shown in Figure 3.8a**, the dark α -FAPbI₃ phase nucleates at the lower-



left corner, reflecting heterogeneous nucleation, and preferentially propagates along the <0001> direction. The stark contrast between the pristine and transformed regions suggests that phase transition happens through the whole thickness along the <10 $\bar{1}$ 0> direction, forming sharp boundaries between the two regions without overlapping (also seen in Figure 3.4c). The dark α -FAPbI₃ regions propagates continuously and gradually, indicating that δ -to- α phase transition is achieved through atom diffusion (or diffusional transformation) instead of collective structure transformation (or displacive transformation). Using the fraction of α -FAPbI₃ area to indicate the transition progress, it consistently exhibits the exponential increase with time at various temperatures, with the faster increase at higher temperature as shown in Figure 3.8b.

$$x(t) = 1 - exp\left[-(k_0 exp\left(\frac{-E_a}{RT}\right)t)^n\right]$$
 (1)

where E_a represents the activation energy, R is the gas constant, n is the growth exponent, k_0 is the rate constant prefactor, and x corresponds to the transition state represented by the α -FAPbI₃ area fraction. The three curves measured at different temperatures in **Figure 3.8b** enable the derivation of E_a for δ -to- α transition to be \sim 1.475 eV (see **Section 3.3.3**). We note that this E_a value is comparable to the reported activation energy for polycrystalline FAPbI₃ thin films (\sim 1.814 eV)³⁹, but higher than what has been reported for 1D FAPbI₃ microwires (\sim 0.84 eV).⁴⁰ Despite the dimension



difference, the latter work also used the simple fitting with an Arrhenius function, which is different from the dedicated JMA model adopted here for diffusional transformation. 124

The observed δ -to- α transition in **Figure 3.8a** is dominated by <0001> propagation, consistent with the work by Lai et al. that demonstrated the preferential growth of δ -FAPbI₃ nanowires and the preferential δ -to- α phase transition both along <0001>. ⁴⁰ The measured average propagation rate along <0001> is ~3.18 μm/s that is also remarkably close to their measured rate (~3 µm/s at 163 °C) on 1D microwires. Such preferential phase propagation has been attributed to the face-sharing PbI₆ octahedra along <0001> in δ-FAPbI₃, which should transform into corner-sharing octahedra during δ-to-α transition. On the other hand, due to the limited dimension of their microwires, only 1D phase transition behavior was studied. 40 In contrast, our FAPbI3 thin films allow us to investigate the anisotropic phase transition along different directions, such as the much slower propagation of α -FAPbI₃ along the perpendicular <1 $\bar{2}$ 10> direction (~0.22 µm/s). The difference in the propagation speeds leads to stair-like transition front with shorter steps along $\langle 1\bar{2}10 \rangle$, as observed at the late stage of transition (Figure 3.8a). Beam effect analysis on our δ -FAPbI₃ films also reveals higher stability of $\{1\overline{2}10\}$ stacking ordering than {0002} (see Section 3.3.4). The relatively unstable {0002} stacking may facilitate the phase transition to α-FAPbI₃, resulting in the preferential propagation of



transition front along <0001>. To better understand such anisotropic transition behavior, we further measure the area propagation rates along both <0001> and <1 $\bar{2}$ 10> directions and derive the corresponding E_a values based on the JMA model. As shown in **Figure 3.8c**, E_a is ~1.439 eV along <0001> and ~1.658 eV along <1 $\bar{2}$ 10>, explaining the preferential phase transition along <0001>. To our best knowledge, this is the first measurement of anisotropic activation energies for δ -to- α FAPbI₃ phase transition.

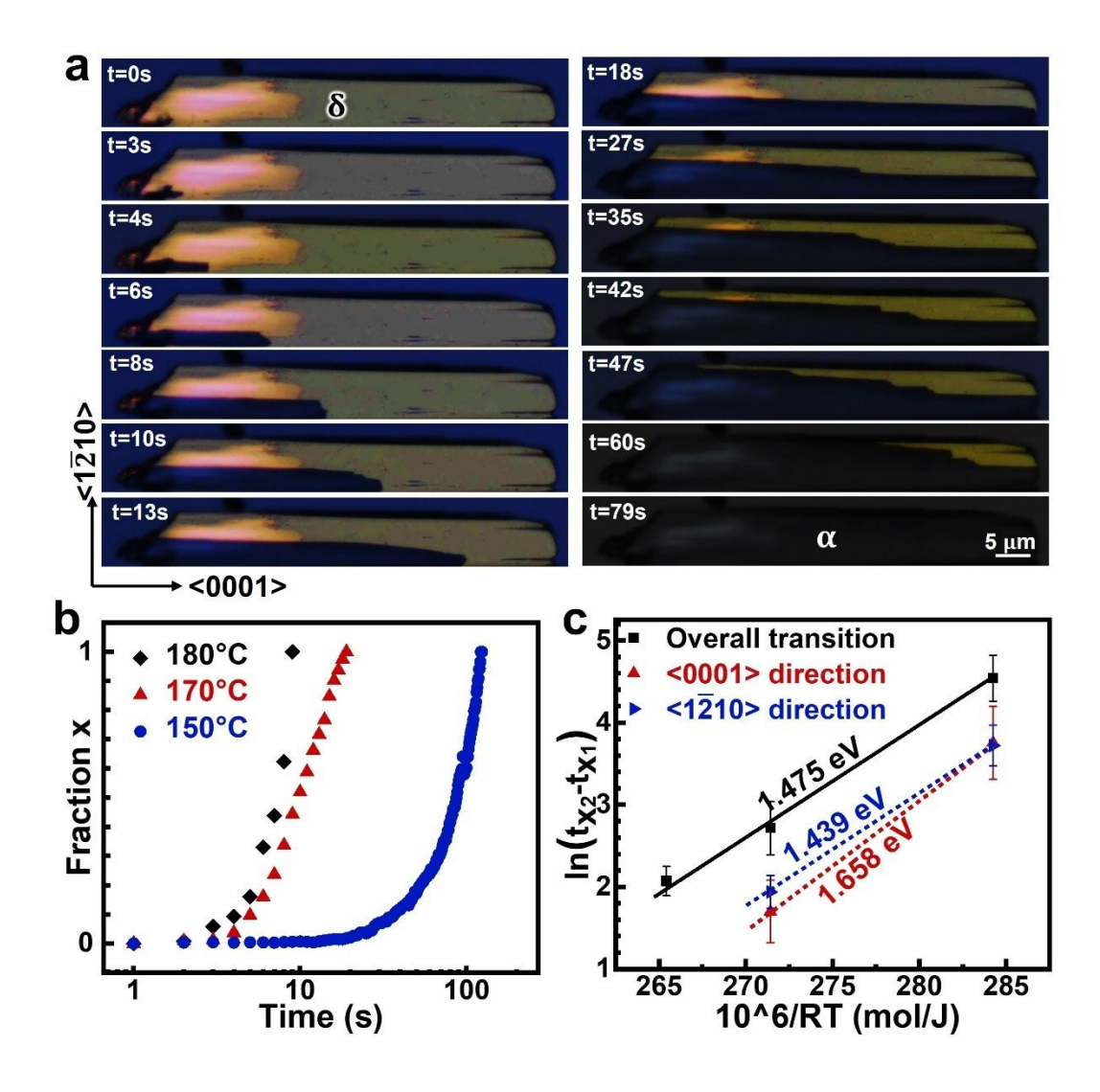


Figure 3.8 (a) Time-series PLM images showing δ -to- α phase transition induced by *in*



situ annealing at 170 °C. (b) Measured α -FAPbI₃ area fraction as functions of annealing time at 150, 170, and 180 °C, respectively. (c) Derivation of activation energies for δ -to- α phase transition along <0001> and <1 $\overline{\mathbf{2}}$ 10> based on the JMA model (see section 3.3.3).

It is noted that XRD in Figure 3.5a reveals the preferential orientation of the transformed α-FAPbI₃ along the {001} plane normal. It indicates the orientation relationship of $<10 \,\overline{1}\,0>_{\delta}//<001>_{\alpha}$, which does not follow the typical basal-type transition $(<0.002>_{H}/<1.11>_{C}, \{1 \bar{2} 10\}_{H}//\{1.10\}_{C},$ hexagonal-to-cubic $\{10 \ \overline{1} \ 0\}_{H}//\{211\}_{C}\}$ or the prismatic-type transition $(<0001>_{H}//<001>_{C}$ and $\{10\overline{1}0\}_{H}//\{1\overline{1}0\}_{C}$). ¹²⁵⁻¹²⁷ We further explore the orientation relationship using 4D-STEM with spatially-resolved diffraction across the transition front between δ and α phases. A special low-dose condition is used with minimized beam effect on FAPbI₃ (see Method, Supporting Information). Figure 3.9e is the dark-field image generated using 0002 diffraction, which shows dark α-FAPbI₃ on top and bright δ-FAPbI₃ at the bottom. δ -FAPbI₃ is oriented along <10 $\overline{1}$ 0> (**Figure 3.9b**) while α -FAPbI₃ is oriented along <001> (Figure 3.9c), consistent with the orientations detected by XRD. The two phases are well separated by the sharp transition front, with no overlap identified on either side, confirming the complete phase transition through the whole thickness (also see **Figure 3.11**). The longest transition front is along $\{1\overline{2}10\}_{\delta}$ in parallel with $\{210\}_{\alpha}$



(yellow lines in Figure 3.9a), consistent with the preferential propagation along the $<0001>_{\delta}$ direction. Perpendicular to $<0001>_{\delta}$, the transition front consists of a few segments with various orientations. Some segments show well-defined orientation relationship (i.e., $\{0002\}_{\delta}//\{120\}_{\alpha}$ for the red lines) while others do not (blue and cyan lines in Figure 3.9a), showing rather complicated transition behavior between δ- and α-FAPbI₃. Interestingly, despite the orientation variations, the majority of the transition front is aligned with $\{210\}_{\alpha}$, suggesting that they are habit planes of α-FAPbI₃ with lower δ/α interfacial energy. Due to the susceptible nature of FAPbI₃, we cannot achieve atomic-resolution imaging at the transition front to reveal the interfacial structure. On the other hand, even for the rational interfaces with $<10\overline{1}0>_{\delta}//<001>_{\alpha}$, $\{1\overline{2}10\}_{\delta}//\{210\}_{\alpha}$, and $\{0002\}_{\delta}//\{120\}_{\alpha}$, we cannot find the way to form coherent interfaces between δ- and α-FAPbI₃.

The incoherent δ/α -FAPbI₃ interfaces have been proposed by Lai et al., who observed the same orientation relationship of $<10\overline{1}0>_{\delta}//<001>_{\alpha}$ as our work. Howe et al. have considered the incoherent interfaces to be like high-angle grain boundaries, which may form liquid-like interfaces at high temperature. The liquid-like interfaces have been shown to facilitate the ion diffusion and the underpinned phase transition, as demonstrated by molecular dynamics simulations on CsPbBr₃. Such incoherent interfaces also implies rather low interfacial energy between δ - and α -FAPbI₃, so that



the transition behavior should be dominated by the surface energy that leads to $\{001\}$ -terminated α -FAPbI₃. The preferred $\{001\}$ -termination for α -FAPbI₃ has been reported by many works, $^{130\text{-}133}$ indicating its lower surface energy. This has been explicitly verified by density functional theory (DFT) calculations showing lower surface energy for both $\{001\}$ and $\{210\}$ planes (**Figure 3.9d**), which explains the observed <001>-oriented α -FAPbI₃ with $\{210\}$ -dominant habit planes at the transition front.



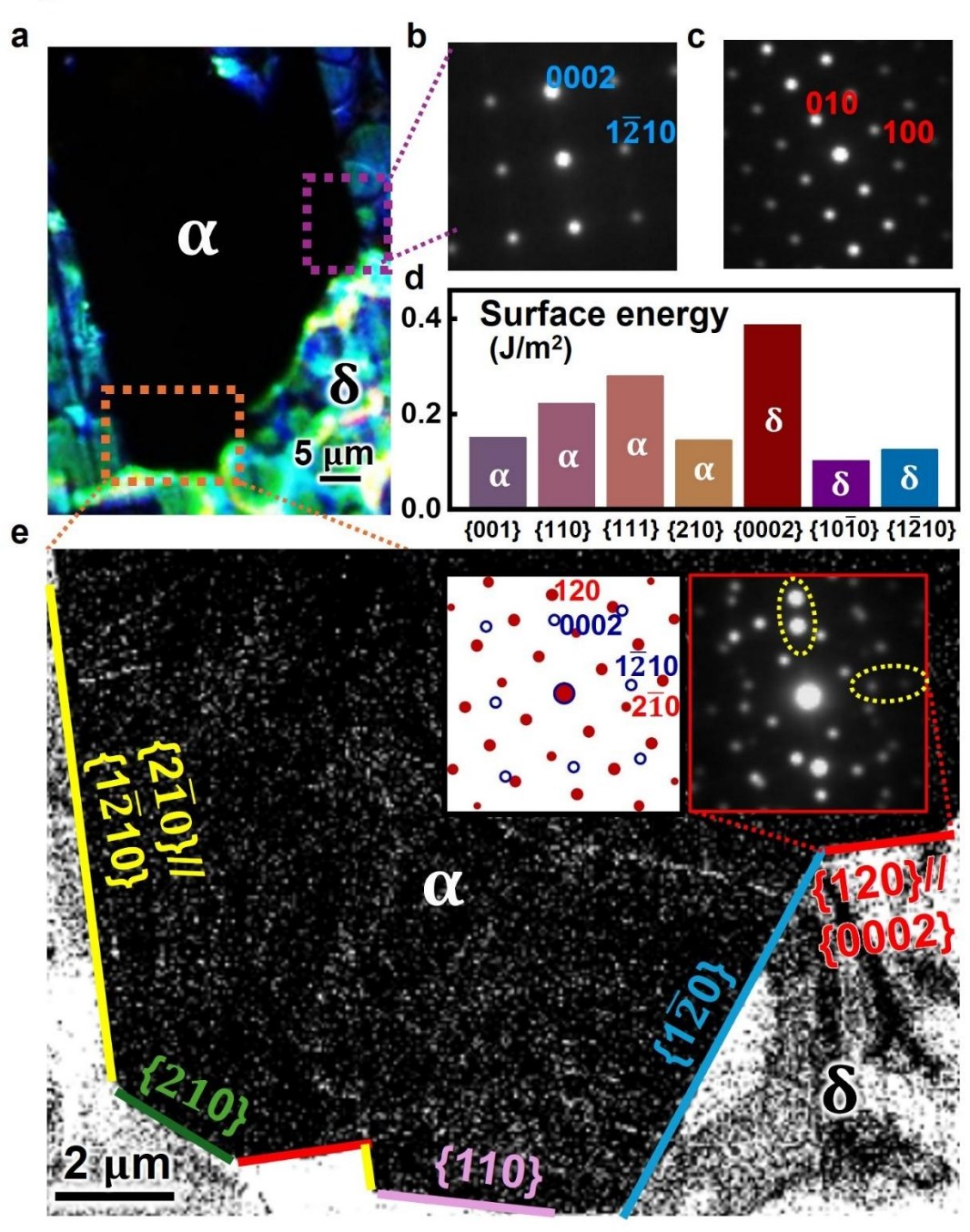


Figure 3.9 (a) PLM image showing a transition front between the colored δ-FAPbI₃ and black α-FAPbI₃. (b,c) Diffraction patterns from 4D-STEM showing (b) $<1\overline{1}00>$ and (c) <001> zone axes for α- and δ-FAPbI₃, respectively. (d) DFT calculation on surface energies of α- and δ-FAPbI₃. (e) Dark-field image reconstructed using 0002 diffraction, showing the morphology of the transition front with the orientation



relationship labelled in different colors. The upper-right inset is a diffraction pattern across the red boundary, showing the overlap of two phases with $<10\overline{\bf 1}0>_{\delta}//<001>_{\alpha}$, $<1\overline{\bf 2}10\}_{\delta}//\{210\}_{\alpha}$, and $<0002\}_{\delta}//\{120\}_{\alpha}$, as illustrated by the schematic on left.

Careful inspection on the PL map in Figures 3.5d-f reveals a decrease of PL intensity inside α-FAPbI₃ near the transition front, which suggests the presence of defects acting as the non-radiative recombination centers. This has been explicitly confirmed by 4D-STEM at the transition front: as shown by the reconstructed bright-field image in Figure 3.10b, α-FAPbI₃ adjacent to the transition front exhibits high-density dark lines along <110>, corresponding to planar defects such as stacking faults and twin boundaries. Planar defects have been identified along {111} in α-FAPbI₃, ^{26, 27} whose intersection with {001} is indeed along <110>, 134 consistent with the observed darkline contrast in Figure 3.10b. Such high-density planar defects break the long-range order perpendicular to the line direction, leading to the broadening of diffraction peaks along $<1\overline{1}0>$ that has been observed in 4D-STEM diffraction patterns (lower-right inset of **Figure 3.10c**). Using the width of 020 diffraction along $<1\overline{1}0>$ to reflect the defect density (or the degree of disorder), Figure 3.10c clearly unveils an increase of defect density in α-FAPbI₃ towards the transition front. Since planar defects especially stacking faults have been identified as the deep recombination centers in α-FAPbI₃,²⁷



their increased density explains the reduced PL intensity near the transition front.

Observation in Figure 3.10 evinces that the initially formed α-FAPbI₃ near the transition front is highly defective with lower crystallinity. In particular, {111} planar defects such as stacking faults and twin boundaries change the local {111} stacking from A-B-C-A-B-C (cubic) to A-B-A-B (hexagonal), and can be considered as the intergrowth of δ phases within α-FAPbI₃. It is thus not a surprise to see such highdensity planar defects near the transition front, which may serve as an intermediate state that is typically observed during the basal-type hexagonal-to-cubic transition. ¹³⁵⁻¹³⁷ On the other hand, with the observed orientation relationship distinct from the basal-type transition, such planar-defect-facilitated phase transition should be accompanied by the reorientation or even recrystallization process, which reorients the formed α-FAPbI₃ to <001> with minimized surface energy. With further annealing, the initially formed defective α-FAPbI₃ will develop better crystallinity with reduced defect density, as reflected by much narrower diffraction peak width farther away from the transition front (**Figure 3.10c**), while the defective transition front further propagates into δ -FAPbI₃ to continue the phase transformation.



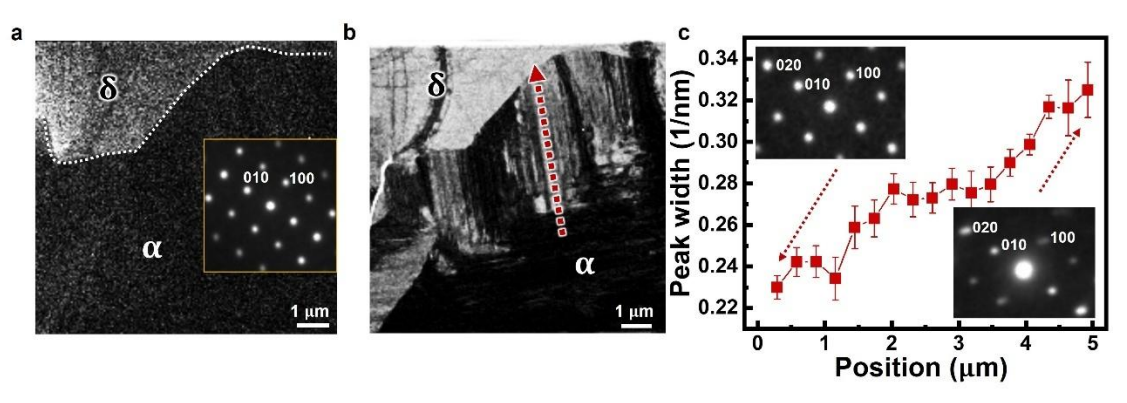


Figure 3.10 (a) Dark-field image reconstructed using 0002 diffraction, showing the δ-to-α transition front along the dotted line. (b) Reconstructed bright-field image from the same region as (a), showing high-density planar defects in the newly formed α-FAPbI₃ near the transition front. (c) Measured 020 diffraction peak width along the red arrow in (b), showing increased defect density towards the transition front. The initial and final diffraction patterns are shown in the insets.

3.3.3 Kinetics analysis using JMA model

Analysis of kinetics of solid-state phase transformation relies on the precise determination of reaction fraction.³⁸ Here transformation fraction x_t is defined as the over-time phase transition area of α -FAPbI₃ (A_t as measured from *in situ* heating PLM) normalized by the total observation area $x_t = A_t/A_{total}$. Such 2D area fraction can represent 3D volume fraction if the transformation happens thoroughly along the thickness that is <100 nm. This has been confirmed by 4D-STEM as shown in **Figure** 3.11: with the scan step ~94 nm, a sharp transition front can still be identified, with



overlapped diffraction from the two phases only observed at one position. With much lower resolution in PLM images, it is thus reasonable to assume a sharp transition front with complete phase transition through the whole thickness. Single nucleation is selected in all experiments, so the kinetics reflect the crystal growth process solely without considering the nucleation rates.

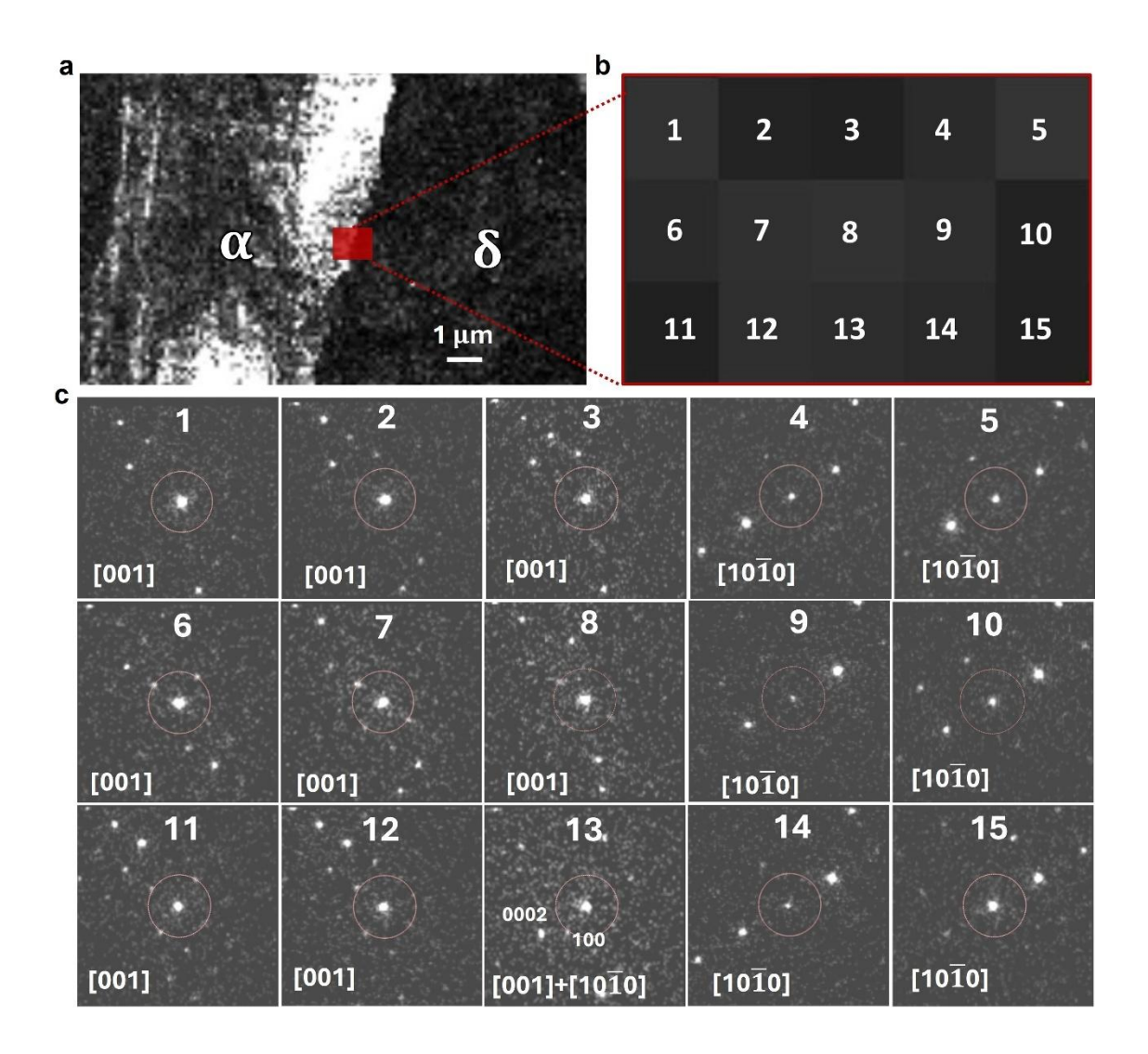


Figure 3.11 (a) Reconstructed dark-field image using 001 diffraction showing the δ -to- α transition front in FAPbI₃. **(b)** Selected 5x3 scan region across the transition front. **(c)**



Corresponding electron diffraction patterns at each scan position, where the radius of the circles represents $1/d_{100}$.

In this work, we employ the isothermal derivation of JMA equation performed by Mittemeijer et al: 138

$$ln(t_{x2} - t_{x1}) = \frac{E_a}{RT} - lnk_0 + ln (\beta_{x2} - \beta_{x1})$$

where t_{xn} represents the time at which the transformation fraction x_n is achieved, and β_{xt} is a state property corresponding to the transformation fraction x_t in this study. Other parameters are the same as the equation (1) in the main text. This equation allows us to derive the activation energies E_a using the plot in **Figure 3.8c**. In particular, by separating and extracting the transformation rates along the <0001> and <1 $\overline{2}$ 10> directions, we can derive the anisotropic E_a values along the two directions. It's worth noting that the measured transformation rate along <0001> based on our observation (~3.18 µm/s) is very close to the reported results from Lai et al (~3 µm/s).

Figure 3.12 plots the transformation fraction data along with the derivation of the growth exponent n from the JMA equation (1): $ln(-ln(1-x)) = ln\left(k_0exp\left(\frac{-E_a}{RT}\right)\right) + nln(t)$. It yields $n \sim 2.09$ at 150°C and ~ 2.12 at 170°C respectively. In contrast to n = 3 for typical isotropic phase transformations, $n \sim 2$ here is attributed to the slow transition rate along $<1\overline{2}10>$, which leads to 2D growth along the other two



orthogonal directions (<0002> and $<10\overline{1}0>$). It unambiguously demonstrates the anisotropic phase transition in our epitaxial FAPbI₃ thin films.¹³⁹

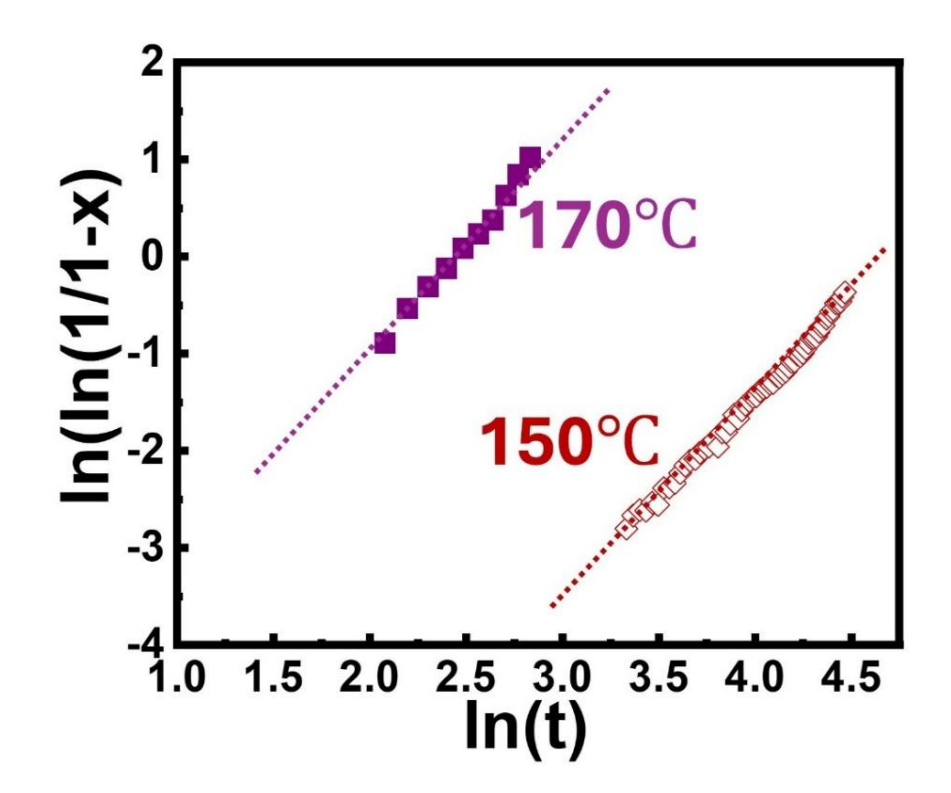


Figure 3.12 Estimation of the growth exponent n from the plot of the δ -to- α phase transition at 150 °C and 170 °C.

3.3.4 Beam effect analysis on stacking stability of $\{1\overline{2}10\}$ and $\{0002\}$

Beam effect on δ -FAPbI₃ films was examined with continuous exposure of electron beam until dose accumulates to ~ 11 e/Å². With increasing electron dose, 0002 and $1\overline{2}10$ diffraction signals exhibit distinct behavior. As shown by the intensity profiles in **Figure 3.13a**, intensity of 0002 diffraction decreases rapidly to 82% at ~ 11 e/Å², while



 $1\overline{2}10$ diffraction shows a steady response without significant changes. Notably, at this electron dose, no additional diffraction spots or positional shifts of existing diffraction was observed. This is consistent with the work done by Yang *et al.* who derived a critical dose of approximately 12.6 e/Å^2 in their beam effect study on α -FAPbI₃. 92

Figure 3.13b plots the relative peak width of 0002 and $1\bar{2}10$, showing the elongation of 0002 diffraction but not for $1\bar{2}10$. It is also inline with the observation of Yang *et al.*, who identified more stacking faults induced by the electron dose ranging from 2.1 to 16.8 e/Å^2 along <111> in α-FAPbI₃, which corresponds to <0001> in our δ-FAPbI₃. Our observation clearly indicates the relatively unstable {0002} stacking compared with {1 $\bar{2}10$ } stacking, which may promote FAPbI₃ phase transition preferentially along <0001>.

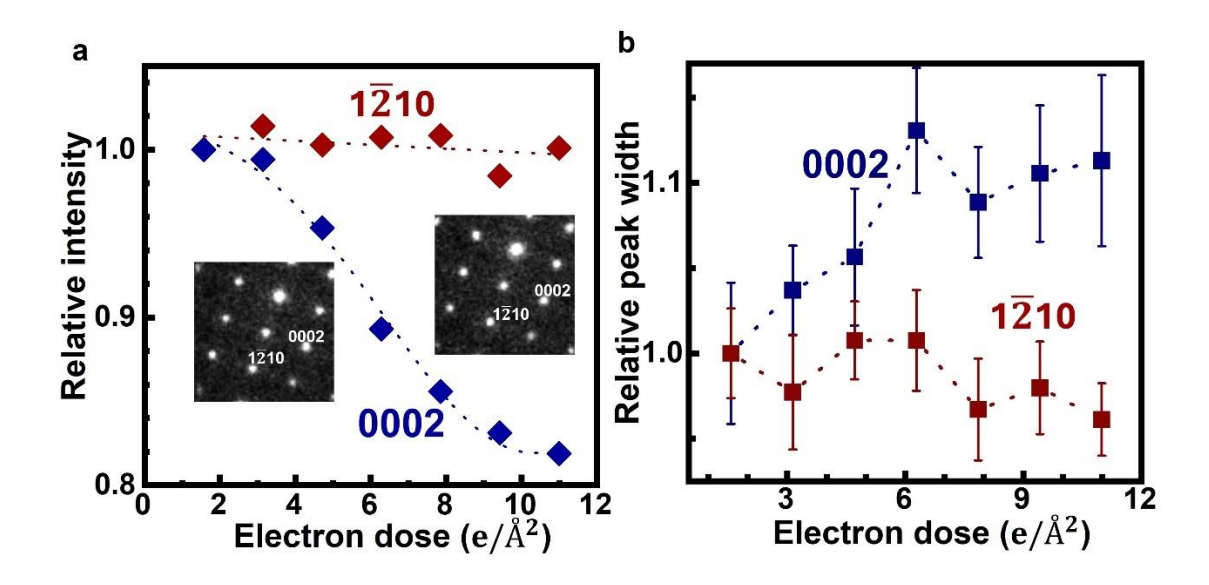


Figure 3. 13 (a) Normalized intensity of $1\overline{2}10$ and 0002 diffraction as a function of



accumulated electron dose. The inset shows the diffraction patterns captured at the initial (left) and final (right) stages of beam exposure. (b) Measured 0002 and $1\overline{2}10$ peak width along <0001> and < $1\overline{2}10$ > respectively.

3.4 Conclusion

In summary, we have combined multiscale microscopy with *in situ* heating to directly observe the anisotropic behavior of δ -to- α phase transition in FAPbI₃ thin films. Our findings show that α -FAPbI₃ nucleates heterogeneously upon heating, followed by a diffusional transformation that preferentially propagates along the <0001> direction, which is underpinned by the lower activation energy along the face-sharing direction of PbI₆ octahedra. 4D-STEM further unveils the morphology and orientation relationship at the δ -to- α transition front, indicating the incoherent δ/α interfaces with potentially lower interface energy. The orientation of the transformed α -FAPbI₃ is thus determined by the surface energy that favors <001>-oriented α -FAPbI₃. We have also identified high-density planar defects in newly formed α -FAPbI₃ near the transition front, which appears to be an intermediate state promoting the δ -to- α transition. Our work not only deepens the understanding of the δ -to- α phase transition mechanism in



FAPbI₃, but also demonstrate a powerful approach combining in situ PLM and 4D-

STEM to probe various phase changes in hybrid perovskites at multiscale.



Chapter 4 Polycrystalline perovskite thin film degradation

4.1 Introduction

FAPbI₃-based perovskites have been achieving remarkable outcomes, primarily attributable to their exceptional optoelectronic properties and suitable bandgap. However, materials based on FAPbI₃ hybrid perovskites often suffer significant degradation, transitioning from the black (α) phase to the yellow (δ) phase, which consequently leads to device failure. This degradation process is reported to be accelerated when exposed to moisture, and illumination. 43, 44, 140, 141 Nevertheless, the degradation process and its elucidation at the structural level remain inadequately explored. Grain boundaries function as structure defects, 43, 142 while planar defects also significantly facilitate dislocation movement, as reported in alloy perovskite oxide materials. 45, 143 In the realm of TEM characterization for perovskites, the methodologies employed for sample preparation, such as direct spin coating onto TEM grids, ¹⁴⁴ do not entirely reproduce the morphological characteristics of FAPbI₃ as observed during device fabrication. This discrepancy is primarily attributed to the influence of the substrate on the nucleation and subsequent growth processes of the perovskite



In this study, we refined the preparation methodology for perovskite TEM samples, yielding free-standing specimens that emulate the growth environments seen in actual device configurations. Moreover, the research conducted a detailed analysis of stacking faults and their association with degradation under exposure to illumination and moisture. This advancement clarifies the phase transition from α - to δ -FAPbI3 and is poised to significantly aid further research into this versatile material.

4.2 Material preparation and characterization

4.2.1 Precursor preparation

For FA_xMA_(1-x)PbI₃, the precursor solutions were fabricated by dissolving 0.4 M FAI, 0.4(1-x) M MACl, and 0.4 M PbI₂ in the mixed solvent of DMF: DMSO=4:1. PTAA solution is obtained by dissolving 30 mg PTAA in 1ml chlorobenzene. All solutions were stirred overnight and filtered by a 0.2 μm filter before further use.

4.2.2 Device fabrication



30 mg/ml PTAA (served as sacrifice layer) was deposited onto UV-ozone treated ITO substrate by spin coating at a rate of 3500 rpm for 30 s with a ramping speed of 2000 rpm s⁻¹ and then annealing at 100 °C for 10mins. Before perovskite deposition, 50 μl DMF was dropped onto PTAA/ITO, stayed stationary for 30 s to enhance wettability, and followed up with spin coating at 1000 rpm to remove the DMF solution.

The perovskite precursor solution was deposited onto the PTAA-coated ITO substrate through a two-step program at 1000 rpm for 10s with a ramping rate of 500 rpm s⁻¹ and 6000 rpm for 35 s with a ramping rate of 3000 rpm s⁻¹, 75 μl CB was flushed onto the surface of perovskite at 10s from the end of spin coating. The sample was then transferred onto a hotplate and annealed at 100 °C; the temperature was then elevated to 150 °C at a rate of 10 °C /min and kept annealing for 60 mins.

4.2.3 Free standing TEM sample preparation

As obtained perovskite/PTAA/ITO was rinsed by 200 μl CB for 2 mins to dissolve the PTAA layer. 30 μl of perovskite/CB was then dropped onto the surface of the TEM copper grid (without any coating). The sample was kept stationary inside the glove box chamber under a vacuum condition for 30 mins to obliterate the remaining solvent. The sample was transferred from the glove box to the TEM room inside a sealed container filled with inert gas. Sample loading time was strictly controlled within



2 mins. Thickness of perovskite layer can be adjusted by tuning perovskite precursor concentration from 0.32 M to 0.47 M. A blade was used to eliminate the near boundary region of perovskite/PTAA/ITO slice before CB washing.

4.2.4 *Ex-situ* TEM

The prepared free standing perovskite thin film TEM sample was encapsulated within a desiccated environment prior to its transfer to the analytical chamber of the Jeol-2100F electron microscope, which functions at an accelerating voltage of 200 kV. The transfer duration was stringently limited to a maximum of two minutes to curtail exposure to environmental contaminants. Data acquisition for SAED and TEM was executed with the sample maintained in a fixed orientation to ensure uniform and dependable imaging throughout the investigative procedures.

4.2.5 Ex-situ XRD and in-situ XRD

Ex-situ XRD measurements were performed using a Rigaku SmartLab, which features a 9-kW source and operates at a wavelength of approximately 1.54 Å. The system's one-dimensional detector design, paired with a rotatable substrate, facilitated comprehensive in-plane and out-of-plane analyses. Before executing the θ -2 θ scans, precise optical alignments and adjustments to the sample height were made to correct



any omega offsets and to enhance the clarity of the signal contrast. The sample on TEM grid and ITO/PTAA are measured using θ -2 θ method.

In-situ annealing XRD was performed on a single crystal prism using a Rigaku SmartLab, which is outfitted with a two-dimensional detector and a precise temperature control system. The temperature of the prism was varied from room temperature to over 150° C, employing the θ - 2θ method, and tests were executed under conditions of both vacuum and normal atmospheric pressure.

4.3 Results and discussion

In our investigation of the structural characteristics of as-grown FA_xMA_{1-x}PbI₃ devices through TEM, we implemented an advanced method for the preparation of perovskite TEM samples, diverging from the conventional practice of direct spin-coating onto carbon-coated TEM grids. This method is informed by prior research into perovskite buried interfaces. ¹⁴⁶ Our protocol involved the deposition of a substantial PTAA layer onto an ITO substrate via spin-coating, followed by the subsequent application of the perovskite layer. The precursor concentration of the perovskite was regulated to achieve a target film thickness of approximately 150 nm, verified using a surface profiler. Post-deposition, the sample underwent a rinsing process with CB, which facilitated the



detachment of the perovskite layer, enabling it to float on the solvent surface. This film was then carefully transferred onto a pristine TEM copper grid (**Figure 4.1**). This technique not only guarantees a consistent foundation for perovskite crystal growth—leveraging PTAA, a prevalent hole transport layer in inverted perovskite solar cells, ¹⁴⁷, but also employs CB, a conventional anti-solvent for FA_xMA_{1-x}PbI₃ that does not compromise the structural integrity of the perovskite.

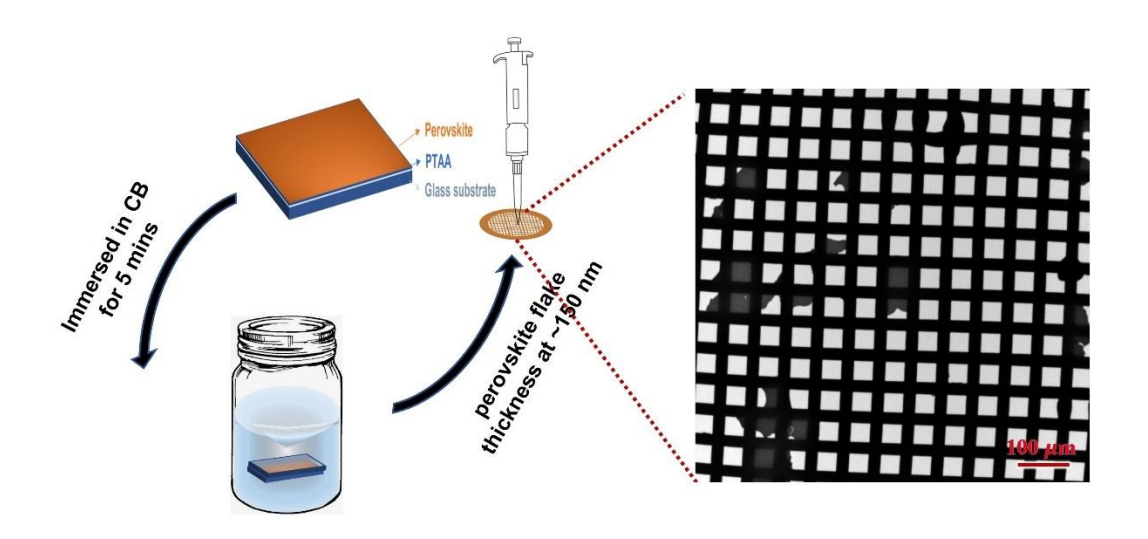


Figure 4. 1 Illustration of free-standing FA_xMA_{1-x}PbI₃ TEM sample preparation

Numerous stacking faults exhibit in the polycrystalline FAPbI₃ film without additives, reflecting in continuous streak toward $<111>_{\alpha}$ (Figure 4.2a). In contrast, the introduction of 20% MA doping led to a diminished presence of these faults, with clearly reduced streak along $<111>_{\alpha}$ (Figure 4.2b,d). The nomenclature for twinning in relation to the matrix plane in this system can be summarized as follows:

$$[\overline{\boldsymbol{g}}_{\boldsymbol{T}^{\text{-}}}(\text{-}\ \overline{\boldsymbol{g}}_{\boldsymbol{M}})]/\!/\ \bar{g}_{p}\ \rightarrow h_{2}+h_{1}=k_{2}+k_{1}=l_{2}+l_{1}$$



And $\overline{g}_T \cdot \overline{g}_p = \overline{g}_M \cdot \overline{g}_p \rightarrow h_1 + k_1 + l_1 = h_2 + k_2 + l_2$; thus

$$h_2 = -h_1 + \frac{2}{3}(h_1 + k_1 + l_1), \ k_2 = -k_1 + \frac{2}{3}(h_1 + k_1 + l_1) \ \text{and} \ l_2 = -l_1 + \frac{2}{3}(h_1 + k_1 + l_1)$$

$$k_1 + l_1)$$

According to above calculation, twin point was derived as:

(111)
$$M \rightarrow (111)$$
 T; (110) $M \rightarrow (\frac{1}{3} \quad \frac{1}{3} \quad \frac{4}{3})$ T and (001) $M \rightarrow (\frac{2}{3} \quad \frac{2}{3} \quad \frac{1}{3})$ T.

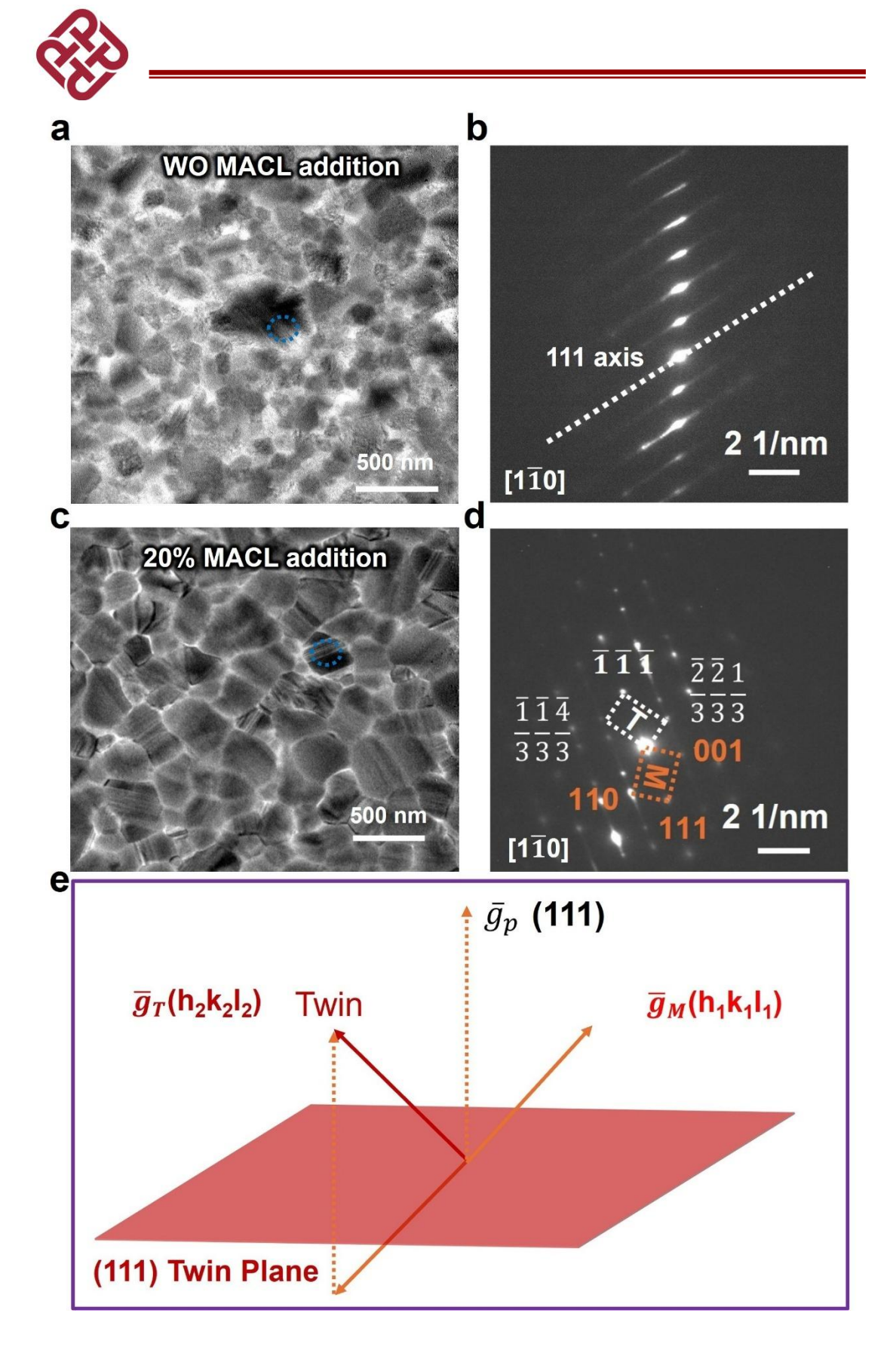


Figure 4.2 SAED analysis of polycrystalline $FA_XMA_{1-X}PbI_3$ thin films. **(a,b)** the SAED patterns of $FAPbI_3$ along the $[1\overline{\bf 1}0]_\alpha$ zone axis, highlighting stacking faults.



(c,d) depict the SAED patterns for FA_{0.8}MA_{0.2}PbI₃ along the same zone axis. (e) provides a schematic representation of twin formation in relation to the $(111)_{\alpha}$ plane along the $[1\overline{1}0]_{\alpha}$ zone axis.

Along <111> $_{\alpha}$ direction of α -FAPbI $_3$, the structure adheres to an abc stacking sequence, in comparison to ab stacking of δ -FAPbI $_3$ along <0001> $_{\delta}$ direction. In a simplified model, {111} $_{\alpha}$ twining structure can be explained as:[10 $\overline{10}$] $_{\delta}$ // [2 $\overline{11}$] $_{\alpha}$, [2 $\overline{110}$] $_{\delta}$ // [1 $\overline{110}$] $_{\alpha}$, and [0001] $_{\delta}$ // [111] $_{\alpha}$ (**Figure 4.3a,b**). Our empirical data indicate that the minimum iodide-iodide distance in the δ -FAPbI $_3$ is approximately 4.273Å, which represents a reduction of 5% relative to the α -FAPbI $_3$, illustrating that twin formation is concomitant with appreciable lattice distortion.



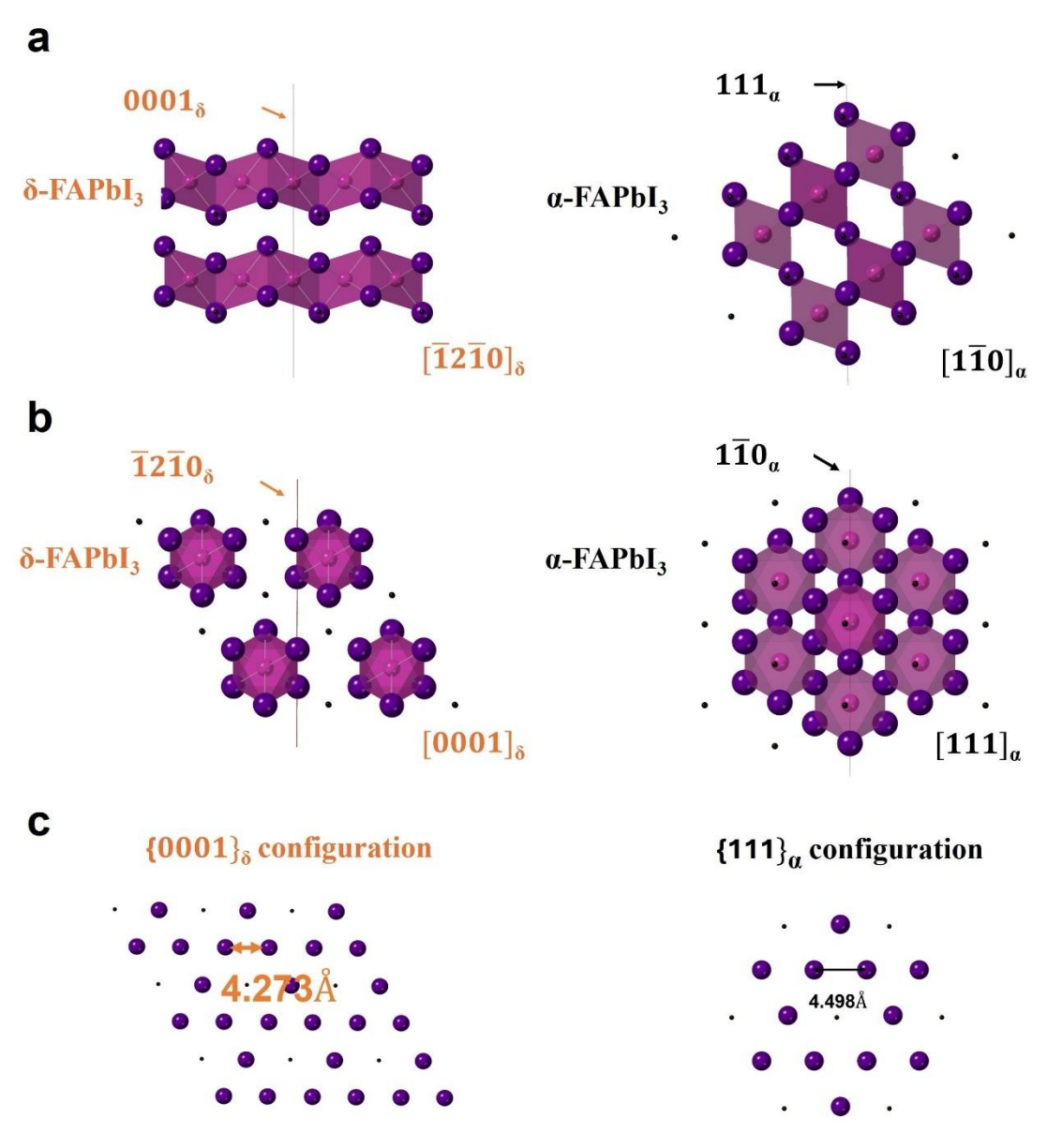


Figure 4.3 The molecular diagrams of α - and δ -FAPbI₃, displayed along their respective zone axes. (a) $[\overline{1210}]_{\delta}$ // $[\overline{110}]_{\alpha}$. (b) $[0001]_{\delta}$ // $[111]_{\alpha}$. (c) single layer atomic distribution of the $\{111\}_{\alpha}$ and $\{0001\}_{\delta}$.

The findings shown in **Figure 4.4a** demonstrate a marked reduction in the residual δ -FAPbI₃ as MA doping increases. Nonetheless, for MA doping levels below 40%, the



residual δ -FAPbI₃ persists, identifiable in XRD by the characteristic $\{10\overline{1}0\}_{\delta}$ peak. The XRD spectra of FAPbI₃, FA_{0.8}MA_{0.2}PbI₃, and FA_{0.6}MA_{0.4}PbI₃, highlighted a coexisting peak at $2\theta=11.4098^{\circ}$ alongside the typical $\{10\overline{1}0\}_{\delta}$ peak at $2\theta=11.78^{\circ}$. This unexpected diffraction was predominantly interpreted as indicative of the hydrate phase of FAPbI₃. ⁴⁶ TEM and SAED analysis of 20% MA-doped samples revealed stacking faults and an additional diffraction spot between $\{001\}_{\alpha}$ and $\{\frac{\bar{2}}{3}, \frac{\bar{2}}{3}, \frac{1}{3}\}_{\alpha}$ points, correlating with the XRD findings at 2θ=11.4098°. Employing the established crystallographic orientation relationship, the simulated SAED data from the $[1\bar{1}0]_{\alpha}$ was integrated with the corresponding $[2\overline{11}0]_{\delta}$ diffraction. The $\{10\overline{1}0\}_{\delta}$ diffraction point slightly shifted from the midpoint between $\{001\}_{\alpha}$ and $\{\frac{\overline{2}}{3}, \frac{\overline{2}}{3}, \frac{1}{3}\}_{\alpha}$, aligning with the discussions on lattice spacing variances between ideal δ - and α -FAPbI₃ on the $\{2\overline{11}\}_{\alpha}$, $\{10\overline{1}0\}_{\delta}$. Distortion of embedded δ-FAPbI₃ in order to match α-FAPbI₃ lattice leads to an enhancement in the lattice spacing of the $\{10\overline{1}0\}_{\delta}$, resulting in the observed peak splitting in XRD. Both our XRD and SAED results corroborate this theoretical δ - α embedded structure. To further examine whether the XRD observed phenomena are associated with moisture interaction, degradation experiments on polycrystalline films were performed under high humidity conditions to gather additional experimental evidence.



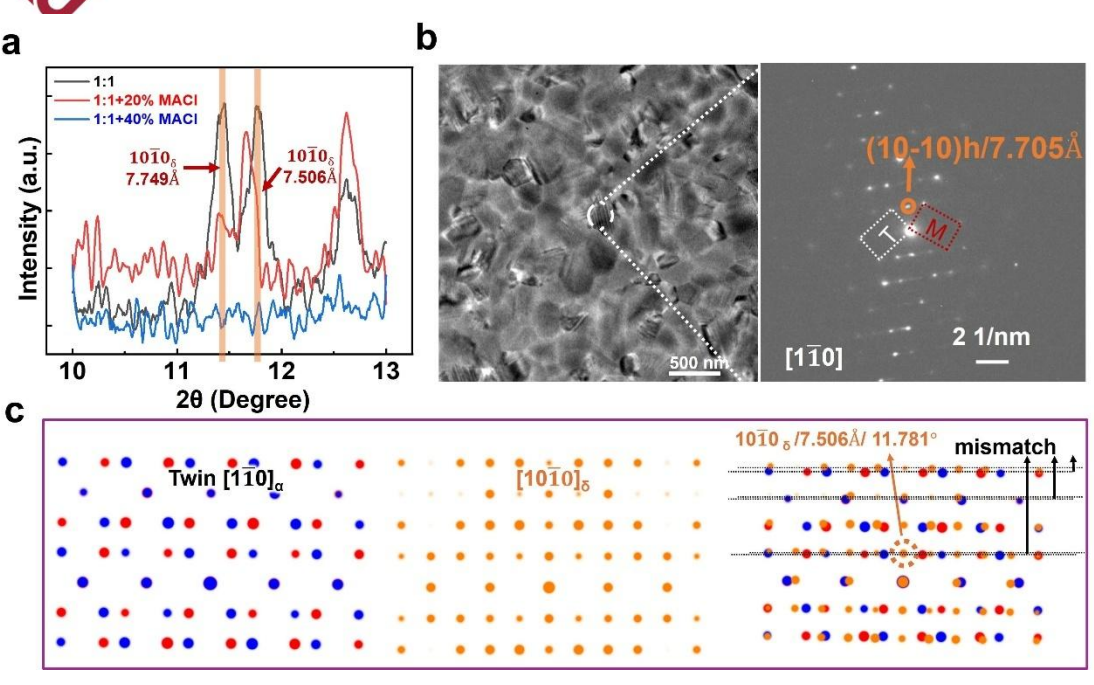


Figure 4.4 Illustration of the α-δ-FAPbI₃ heterojunction. (a) presents the XRD spectra for FAPbI₃, FA_{0.8}MA_{0.2}PbI₃, and FA_{0.6}MA_{0.4}PbI₃. (b) depict the TEM and SAED images for FA_{0.8}MA_{0.2}PbI₃, respectively. (c) shows a combined simulated SAED pattern featuring $[1\overline{\bf 1}0]_{\alpha}$ and $[2\overline{\bf 1}\overline{\bf 1}0]_{\delta}$ zone axis.

In the conducted degradation experiments, the deterioration of FAPbI₃ was accelerated through exposure to ultraviolet light and humidity, both factors known to facilitate the δ to α phase transition. The degradation process of FAPbI₃ was monitored by tracking changes in peak intensities at 2θ =11.40° and 2θ =11.78°. It was previously postulated that the 2θ =11.40° peak corresponds to a fixed-orientation and distorted δ -FAPbI₃. XRD data shown in **Figure 4.5a** indicated that the intensities of both the 2θ =11.40° and 2θ =11.78° peaks initially increased with prolonged exposure, suggesting



a probable growth of the embedded δ -FAPbI₃ due to its greater lattice instability.

As the experiments progressed, the intensity of the 2θ =11.40° peak gradually diminished to zero, signifying the completion of the crystal growth from the embed and distorted δ -FAPbI₃ and the subsequent alleviation of stress, ultimately leaving no residual δ -FAPbI₃ signal. This experimental finding challenges the prior assertion that the 2θ =11.40° peak was indicative of water hydrates. The findings suggest that water preferentially forms a more stable interaction with PbI₂, resulting in the formation of a non-crystalline compound. This is corroborated by experimental results showing a gradual decline in the PbI₂ peak, with all FAPbI₃ $\{10\overline{1}0\}_{\delta}$ peaks stabilizing at 2θ =11.78° following the phase transition, even amidst ample water presence.

Shown in **Figure 4.4a**, with the increasing MA doping ratio, the embedded δ -FAPbI₃ intensity diminishes, which aligns with the findings presented in **Figure 4.2**. Even when the MA ratio reaches 20%, a residual portion of distorted δ -FAPbI₃ persists. Consequently, the degradation experiment on FA_{0.8}MA_{0.2}PbI₃ was performed to further investigate these effects.



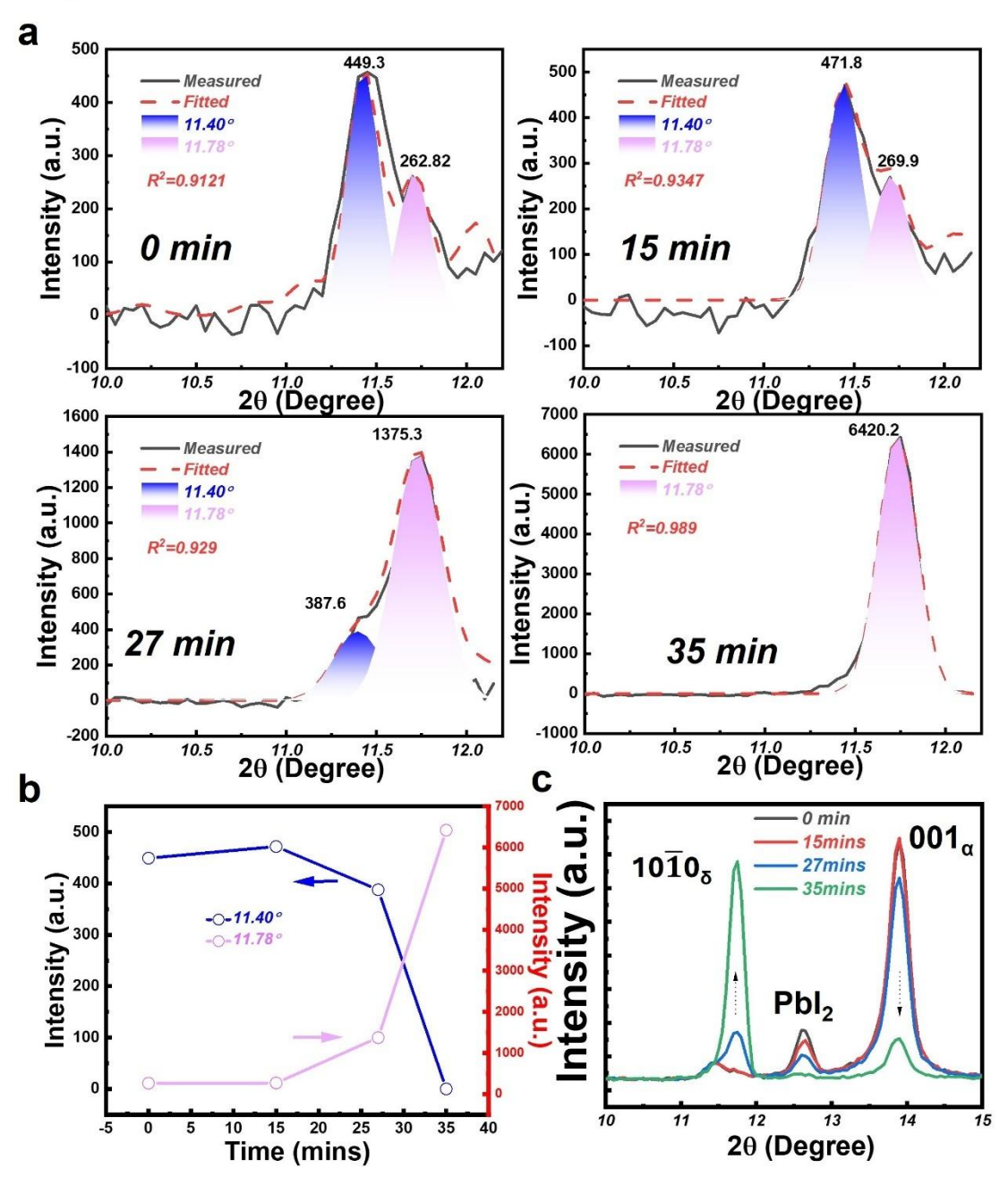


Figure 4.5 Degradation of FAPbI₃ under UV and relative humidity of 88%. (a) XRD results of pristine FAPbI₃ polycrystal thin film, and under UV and water exposure for 0, 15, 27, and 35 minutes, with peak split analysis of the $\{10\overline{\mathbf{1}}0\}_{\delta}$ peak. (b) change in intensity of the split peak in relation to degradation time. (c) XRD of FAPbI₃ thin film from 20 ranging from 10° to 15°, indicating changes



in both δ -, α -FAPbI₃ and PbI₂ diffraction.

The results of FA_{0.8}MA_{0.2}PbI₃ degradation under UV and moisture conditions are shown in **Figure 4.6**, which exhibit consistency with the results of pure FAPbI₃. Initially, there is an increase in the intensity of the distorted δ -FAPbI₃. As the degradation process progresses, the intensity of the embedded δ -FAPbI₃ diminishes, indicating the relaxation of the crystal lattice.

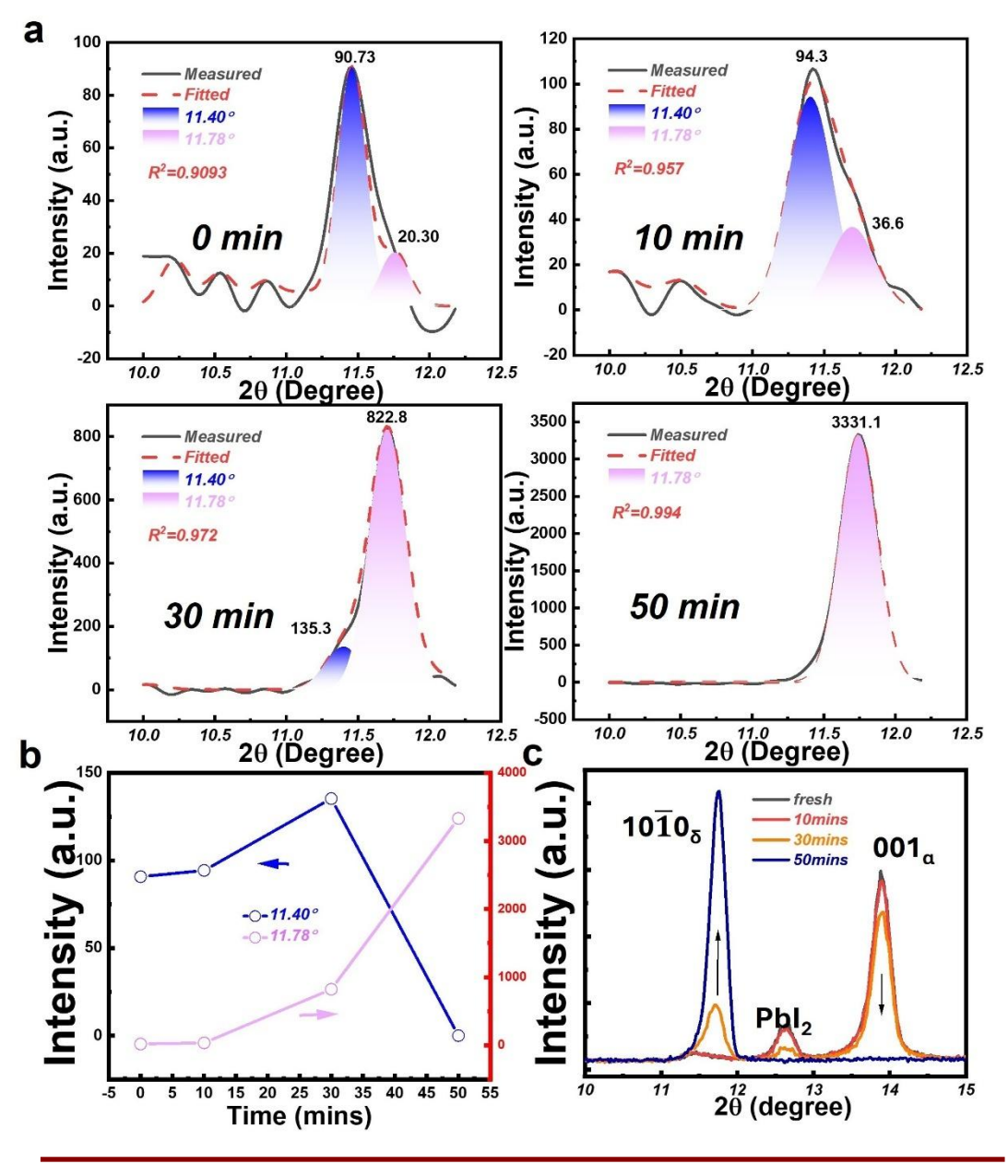




Figure 4.6 Degradation of FA_{0.8}MA_{0.2}PbI₃ under UV and relative humidity of 88%. (a) XRD results of pristine polycrystal thin film, and under UV and water exposure for 0, 10, 30, and 50 minutes, with peak split analysis of the {10**1**0}_δ peak. (b) change in intensity of the split peak in relation to degradation time. (c) XRD of FA_{0.8}MA_{0.2}PbI₃ thin film from 2θ ranging from 10° to 15°, indicating changes in both δ-, α-FAPbI₃, and PbI₂ diffraction.

The results, integrating TEM and XRD analyses, reveal the formation of degradation nucleation in a distorted δ -FAPbI $_3$ formation, previously overlooked in investigations of hybrid perovskites. Moreover, this distorted δ -FAPbI $_3$ acts as a potential instability factor, serving as a nucleation site that favors transformation during the initial stages of the degradation process. In-situ annealing TEM and in-situ annealing XRD were conducted to investigate the transformations under vacuum conditions using the previously prepared epitaxial δ -FAPbI $_3$ thin film to examine the phase transition behavior under low pressure condition. Results depicted in **Figure 4.7** show a direct transformation of the δ -FAPbI $_3$ into PbI $_2$ at elevated temperatures, indicating that the vacuum conditions altered the thermodynamic behavior of the δ to α phase transition due to the volatile characteristics of the organic component. 150



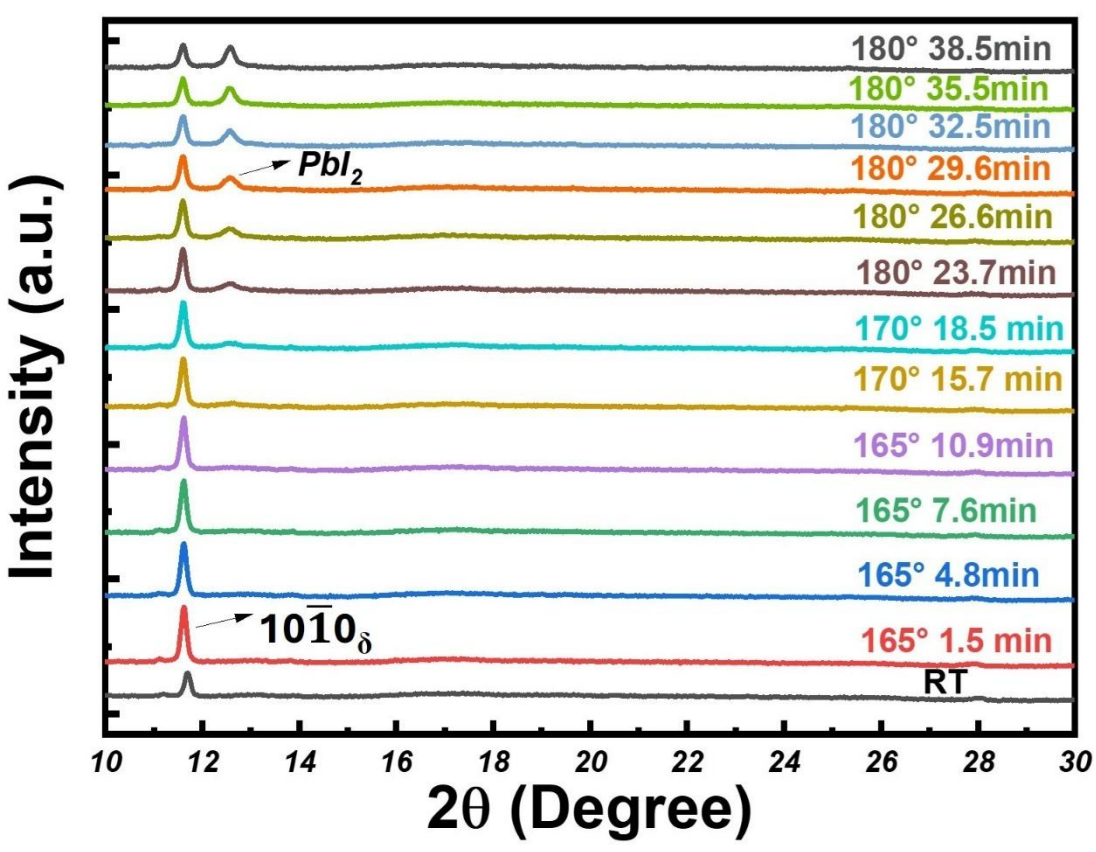


Figure 4.7 In-situ annealing XRD performed on epitaxial δ -FAPbI₃ thin film under a vacuum condition (<10⁻⁵ torr). The temperature was increased from room temperature to 180°C.

The in-situ annealing TEM experiment, as depicted in **Figure 4.8**, confirms the direct decomposition of FAPbI₃. Initially aligned along the $[10\overline{1}0]_{\delta}$ zone axis, the sample post-annealing exhibited a diffraction pattern similar to those observed in electron beam damage experiments. Notably, the intensity of the $\{0002\}_{\delta}$ diffraction point decreased, transitioning to a smaller d-spacing at diffraction point 'a'. Moreover, an additional



diffraction point, at double the d-spacing of point 'a' and denoted as point 'b', emerged, as highlighted in **Figure 4.8d**. These changes are indicative of the formation of distorted PbI₂. In contrast, the $2\overline{11}0_{\delta}$ point remained stable in position, albeit with a reduced diffraction intensity.

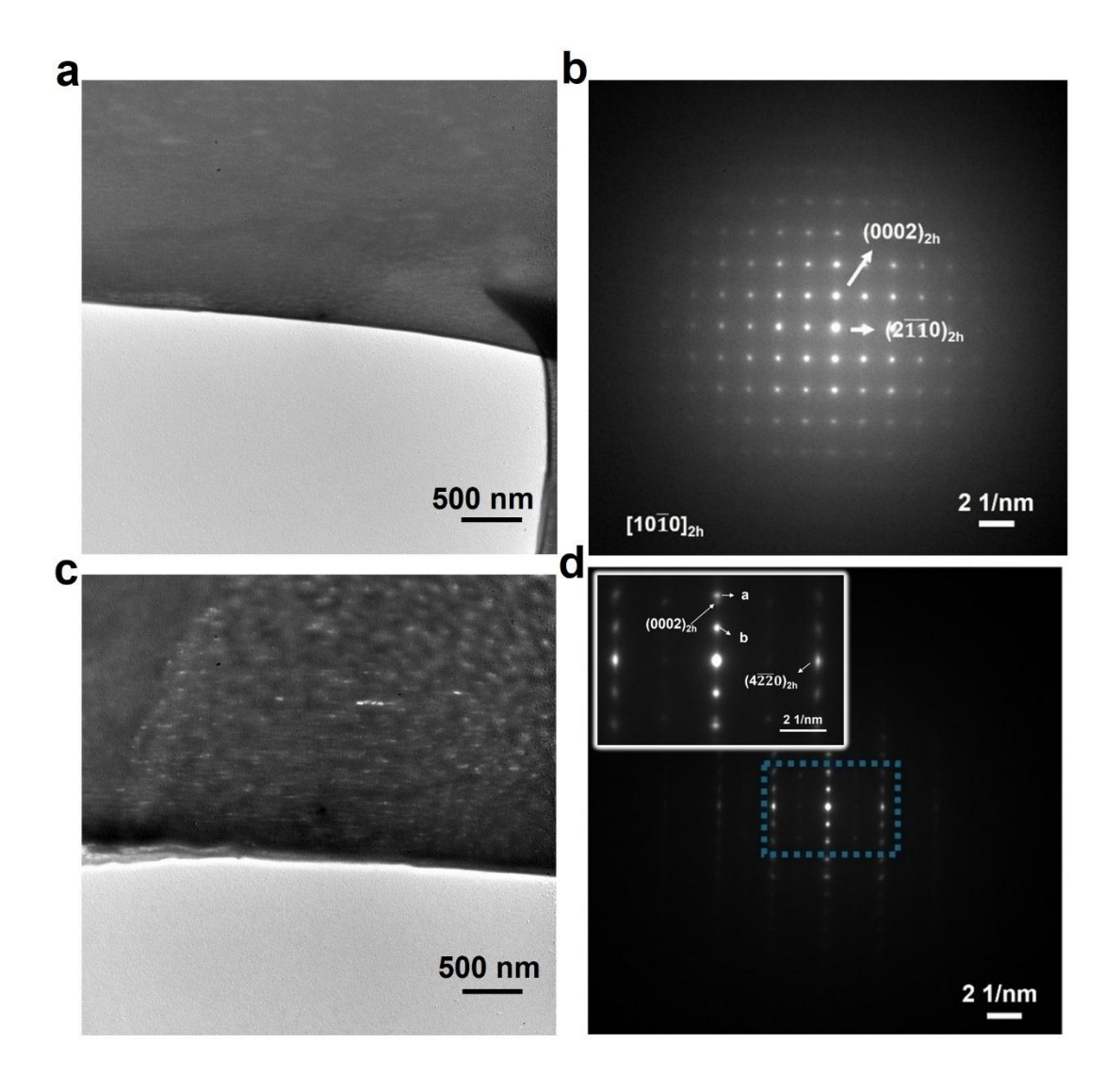


Figure 4.8 In-situ annealing TEM on a single crystal δ-FAPbI₃ thin film at a temperature of 150°C. (a,c) TEM image of the sample before and after annealing. (b,d) SAED of the sample before and after annealing at 150°C. (inset) enlarged



electron diffraction pattern of the area highlighted by the blue dashed box.

4.4 Conclusion

This investigation elucidates the degradation mechanisms of FAPbI3, including its MA-doped derivatives, under ultraviolet radiation and moisture exposure. Advancements in the fabrication methods for hybrid perovskite TEM samples enabled the generation of specimens suitable for extensive TEM analysis, closely simulating the growth conditions typical of device architectures. Subsequent analytical evaluations identified the simultaneous presence of distorted δ -FAPbI3 embedded within a α -FAPbI3 matrix. Degradation studies indicated that the embedded δ -FAPbI3 act as nucleation centers for degradation processes, with these signals dissipating upon the completion of degradation. Moreover, it was observed that under vacuum conditions, FAPbI3 does not transition from δ to α phases. Instead, akin to alterations induced by electron beam exposure, FAPbI3 decomposes directly into PbI2, highlighting that modifications in ambient pressure critically influence the dynamics of phase transitions.

These findings elucidate the structural morphology of residual δ -FAPbI $_3$ and their consequential impact on the degradation processes of perovskite materials. This knowledge provides critical insights and methodological advancements that are pivotal



for refining perovskite compositions and enhancing the analytical capabilities of TEM in future studies.



Chapter 5 Conclusions and future work

5.1 Summary of work

The investigation of phase transitions in hybrid perovskites, particularly FAPbI₃, is increasingly recognized as critical for enhancing material properties and elucidating unique phenomena. In this dissertation, the research emphasis is placed on synthesizing high-quality epitaxial δ -FAPbI₃ thin films, coupled with *in situ* observations of phase transformations, detailed kinetic studies, and mechanistic elucidations. Additionally, this work examines the degradation processes observed in polycrystalline FAPbI₃ thin films fabricated under conventional device conditions. Drawing on both *in-situ* and *ex-situ* experimental observations, the study rigorously examined the anisotropic phase transition of δ - to α - FAPbI₃ and explored its association with the emergence of intragrain defects. Additionally, crystallographic analyses across the interphase interfaces were conducted, offering detailed insights into the underlying mechanisms of this distinctive phase transition.

Initially, the synthesis of single crystal δ -FAPbI₃ prism was conducted using an antisolvent crystallization methodology, employing GBL as the solvent and CB as the antisolvent. Comprehensive characterization of these crystals was performed using



XRD with an adjustable platform and steady-state PL analysis. This approach consistently produced pure prismatic single crystals δ -FAPbI₃ (yellow). Upon annealing these crystals at temperatures above 150°C, a transformation into the δ -FAPbI₃ (black) was observed. Following the successful synthesis of single-crystal δ -FAPbI₃, refinements were made to the synthesis protocol by incorporating additional pressure within a space confined environment. This modification significantly enhanced the capability for large-scale fabrication of single-crystal δ -FAPbI₃ thin films, specifically oriented along the $\lceil 10\overline{1}0 \rceil_{\delta}$ crystallographic direction.

Secondly, leveraging the distinct crystallographic structures of the δ - and α - FAPbI₃, *insitu* polarized optical microscopy was employed. This technique effectively delineated the dynamic phase transitions between these two phases during annealing, facilitating continuous observation of the structural transformations. With the crystallographic orientations of the thin films accurately determined, dynamic analyses were conducted at various annealing temperatures. The JMA model was applied to calculate the activation energies for phase transitions oriented towards the $\langle 1\bar{2}10\rangle_{\delta}$ and $\langle 0001\rangle_{\delta}$ directions, respectively. The results indicated that the phase transition was more readily initiated in the $\langle 0001\rangle_{\delta}$ direction. The Avrami exponent of n was calculated to be near 2, combining with this manifestation of sporadic nucleation underscores the anisotropic nature of the phase transformation from δ - to α -FAPbI₃, aligning with the observed



images of phase transition. Following the initial confirmation of the anisotropic phase transformations, further investigation was performed by confocal PL mapping near the transition front, which contains numerous recombination centers near the front compared to earlier transformed regions.

Thirdly, the single crystal δ-FAPbI₃ thin film, initially grown on a SiO₂ substrate, was transferred onto a TEM grid using PS and subsequently cleaned by rinsing with CB. TEM analysis of the prepared sample confirmed the exclusive presence of the δ -FAPbI₃ oriented along the $[10\overline{1}0]_{\delta}$ zone axis, with no impurities detected. Subsequently, transition fronts were examined using 4D-STEM and the electron dose was controlled at extremely low level ($\sim 1.57 \text{ e}^{-1}/\text{Å}^2$) to prevent beam effect damage. This examination revealed that the distribution of intragrain defects, identified by numerous streaks along $<001>_{\alpha}$ direction, was near the transition front. Additionally, amorphous degree analysis based on the diffraction patterns from the same position suggested a decrease in degree of crystallinity along the $<1\overline{2}10>_{\delta}$ direction, was consistent with observation of confocal PL. This study also investigate on the crystallographic relationships across the transition front, the rational interfaces $<10\overline{1}0>_{\delta}//<001>_{\alpha}$, $\{1\overline{2}10\}_{\delta}//\{210\}_{\alpha}$ combined with DFT calculation on surface energy of δ - and α -FAPbI₃, we elucidate that the phase transition was dominated mostly by surface energy other than interface energy.. Additionally, the stability of the single crystal δ-FAPbI₃ under electron beam exposure



was assessed. The experiments revealed accelerated degradation of the $\{0002\}_{\delta}$ plane, with significant structural collapse at an electron dose of approximately 72.2 e⁻¹/Å². In contrast, the $\{1\overline{2}10\}_{\delta}$ lattice demonstrated enhanced stability during electron irradiation, confirming the faster transition rate along <0001> direction due to the reconstruction nature of this phase transition. This work not only deepens the understanding of the δ -to- α phase transition mechanism in FAPbI₃ but also demonstrate a powerful approach combining *in situ* PLM and 4D-STEM to probe various phase changes in hybrid perovskites at multiscale.

Lastly, the degradation of FAPbI₃ polycrystalline thin films under ultraviolet and moisture environment was systematically evaluated through the integrated application of XRD and TEM coupling with SAED. The preparation of TEM specimens was conducted by an innovative method, wherein FAPbI₃ was initially deposited onto a PTAA, subsequently rinsed and extracted using CB. XRD results elucidated a peak split in the residual $\{10\ \bar{1}\ 0\}_{\delta}$ diffraction within both FAPbI₃ and the mixed-cation formulation FA_{0.8}MA_{0.2}PbI₃. These findings were substantiated by TEM and SAED, which demonstrated a distortion of the δ -FAPbI₃ embedded within a α -FAPbI₃, preserving a basal orientation relationship. This phase distortion acts as the initial nucleation site for degradation, ultimately transitioning to a liberated δ -FAPbI₃ at the



conclusion of the degradation process as elucidated by ex-situ XRD measurements conducted under conditions of illumination and moisture exposure.

Surprisingly, our findings demonstrate the direct formation of phase-pure α -FAPbI₃ with preferential orientation along the $[001]_{\alpha}$ direction, achieved simply by annealing epitaxial δ -FAPbI₃ without the need for additives or controlled atmosphere. This discovery holds significant implications, not only for fundamental mechanistic studies but also for practical applications in perovskite device fabrication. This study has advanced the understanding of the phase transition process in FAPbI₃ and introduced a promising methodology for investigating hybrid perovskites.

5.2 Future work

5.2.1 Synthesis of single crystal α -FAPbI $_3$ thin film

In this section, we plan to extend our approach by employing space-confined multiple inverse temperature annealing at elevated temperatures for the synthesis of single-crystal α -FAPbI $_3$ thin film. This will be achieved by inserting a small volume of supersaturated FAPbI $_3$ precursor into the center of the same setup, placing it into a furnace with an N $_2$ atmosphere, and gradually elevating the temperature to allow for the formation of α -FAPbI $_3$.



5.2.2 Degradation of single crystal α-FAPBI₃ thin films

In-situ gas-phase TEM experiments based on single crystal thin films can provide definitive crystallographic orientation information and more observable positions. Therefore, we will conduct in-depth studies on the gas-phase (H₂O) degradation of FAPbI₃ using in-situ TEM techniques as well as polarized optical microscopy.

5.2.3 Low-dose high resolution imaging

Further investigation at atomic resolution will be conducted to elucidate the transition front mechanism, which is expected to provide deeper insights and advance this research field.

5.2.4 Mixed halide and cation system

Beyond pure FAPbI₃, our synthesis method is adaptable to mixed halide/cation perovskites by optimizing the formulation, enabling studies of structural evolution and photovoltaic applications.



Reference

- (1) (IEA), I. E. A. *Electricity 2024: Executive Summary*. 2024. https://www.iea.org/reports/electricity-2024/executive-summary (accessed.
- (2) Enerdata. *Global Energy Trends 2024: Consolidated Energy Statistics & World Trends*. 2024. https://www.enerdata.net/publications/reports-presentations/world-energy-trends.html (accessed.
- (3) Hughes, D.; Rosner, R.; Weiss, N. The Solar Tachocline Cambridge University Press. *Cambridge, UK (Cited on pages 2, 4, 5, 6 and 243)* **2007**.
- (4) (IEA-PVPS), I. P. P. S. P. Snapshot 2024. 2024. https://iea-pvps.org/snapshot-reports/snapshot-2024/ (accessed.
- (5) (IEA), I. E. A. IEA Sees Great Potential for Solar, Providing Up to a Quarter of World Electricity by 2050. 2024. https://www.iea.org/news/iea-sees-great-potential-for-solar-providing-up-to-a-quarter-of-world-electricity-by-2050 (accessed.
- (6) (IRENA), I. R. E. A. Renewable Capacity Statistics 2024. 2024. https://www.irena.org/Publications/2024/Mar/Renewable-capacity-statistics-2024?trk=public post comment-text (accessed.
- (7) (IRENA), I. R. E. A. Renewable Power Generation Costs in 2020. 2021. https://www.irena.org/publications/2021/Jun/Renewable-Power-Costs-in-2020 (accessed.
- (8) Green, M.; Dunlop, E.; Hohl-Ebinger, J.; Yoshita, M.; Kopidakis, N.; Hao, X. Solar cell efficiency tables (version 57). *Progress in photovoltaics: research and applications* **2021**, *29* (1), 3-15.
- (9) Kojima, A.; Teshima, K.; Shirai, Y.; Miyasaka, T. Organometal halide perovskites as visible-light sensitizers for photovoltaic cells. *Journal of the american chemical society* **2009**, *131* (17), 6050-6051.
- (10) Jeong, J.; Kim, M.; Seo, J.; Lu, H.; Ahlawat, P.; Mishra, A.; Yang, Y.; Hope, M. A.; Eickemeyer, F. T.; Kim, M. Pseudo-halide anion engineering for α -FAPbI3 perovskite solar cells. *Nature* **2021**, *592* (7854), 381-385.
- (11) (NREL), N. R. E. L. Best Research-Cell Efficiency Chart. 2024. https://www.nrel.gov/pv/cell-efficiency.html (accessed.
- (12) Eperon, G. E.; Stranks, S. D.; Menelaou, C.; Johnston, M. B.; Herz, L. M.; Snaith, H. J. Formamidinium lead trihalide: a broadly tunable perovskite for efficient planar heterojunction solar cells. *Energy & Environmental Science* **2014**, *7* (3), 982-988.
- (13) Li, Z.; Yang, M.; Park, J.-S.; Wei, S.-H.; Berry, J. J.; Zhu, K. Stabilizing perovskite

103



- structures by tuning tolerance factor: formation of formamidinium and cesium lead iodide solid-state alloys. *Chemistry of Materials* **2016**, *28* (1), 284-292.
- (14) Kim, J. Y.; Lee, J.-W.; Jung, H. S.; Shin, H.; Park, N.-G. High-efficiency perovskite solar cells. *Chemical Reviews* **2020**, *120* (15), 7867-7918.
- (15) Goldschmidt, V. The laws of crystal chemistry. *Naturwissenschaften* **1926**, *14* (21), 477-485.
- (16) Goldschmidt, V. M. Die gesetze der krystallochemie. *Naturwissenschaften* **1926**, *14* (21), 477-485.
- (17) Kieslich, G.; Sun, S.; Cheetham, A. K. Solid-state principles applied to organic-inorganic perovskites: new tricks for an old dog. *Chemical Science* **2014**, *5* (12), 4712-4715.
- (18) Travis, W.; Glover, E.; Bronstein, H.; Scanlon, D.; Palgrave, R. On the application of the tolerance factor to inorganic and hybrid halide perovskites: a revised system. *Chemical Science* **2016**, *7* (7), 4548-4556.
- (19) Pauling, L. The Nature of the Chemical Bond and the Structure of Molecules and Crystals, 12. print. Cornell University Press, Ithaca: 1993.
- (20) Zheng, Z.; Wang, S.; Hu, Y.; Rong, Y.; Mei, A.; Han, H. Development of formamidinium lead iodide-based perovskite solar cells: Efficiency and stability. *Chemical Science* **2022**, *13* (8), 2167-2183.
- (21) Søndenå, R.; Stølen, S.; Ravindran, P.; Grande, T.; Allan, N. L. Corner-versus face-sharing octahedra in A Mn O 3 perovskites (A= Ca, Sr, and Ba). *Physical Review B* **2007**, *75* (18), 184105.
- (22) Lu, H.; Liu, Y.; Ahlawat, P.; Mishra, A.; Tress, W. R.; Eickemeyer, F. T.; Yang, Y.; Fu, F.; Wang, Z.; Avalos, C. E. Vapor-assisted deposition of highly efficient, stable black-phase FAPbI3 perovskite solar cells. *Science* **2020**, *370* (6512), eabb8985.
- (23) Masi, S.; Gualdrón-Reyes, A. F.; Mora-Sero, I. Stabilization of black perovskite phase in FAPbI3 and CsPbI3. *ACS Energy Letters* **2020**, *5* (6), 1974-1985.
- (24) Zheng, X.; Wu, C.; Jha, S. K.; Li, Z.; Zhu, K.; Priya, S. Improved phase stability of formamidinium lead triiodide perovskite by strain relaxation. *ACS Energy Letters* **2016**, *1* (5), 1014-1020.
- (25) Du, T.; Macdonald, T. J.; Yang, R. X.; Li, M.; Jiang, Z.; Mohan, L.; Xu, W.; Su, Z.; Gao, X.; Whiteley, R. Additive-Free, Low-Temperature Crystallization of Stable α -FAPbI3 Perovskite. *Advanced Materials* **2022**, *34* (9), 2107850.
- (26) Pham, H. T.; Yin, Y.; Andersson, G.; Weber, K. J.; Duong, T.; Wong-Leung, J. Unraveling the influence of CsCl/MACl on the formation of nanotwins, stacking faults and cubic supercell structure in FA-based perovskite solar cells. *Nano Energy* **2021**, *87*, 106226.
- (27) Li, W.; Rothmann, M. U.; Zhu, Y.; Chen, W.; Yang, C.; Yuan, Y.; Choo, Y. Y.; Wen,

- X.; Cheng, Y.-B.; Bach, U. The critical role of composition-dependent intragrain planar defects in the performance of MA1–x FA x PbI3 perovskite solar cells. *Nature Energy* **2021**, 6 (6), 624-632.
- (28) Burgers, W. On the process of transition of the cubic-body-centered modification into the hexagonal-close-packed modification of zirconium. *Physica* **1934**, *1* (7-12), 561-586.
- (29) Pool, V. L.; Dou, B.; Van Campen, D. G.; Klein-Stockert, T. R.; Barnes, F. S.; Shaheen, S. E.; Ahmad, M. I.; Van Hest, M. F.; Toney, M. F. Thermal engineering of FAPbI3 perovskite material via radiative thermal annealing and in situ XRD. *Nature communications* **2017**, *8* (1), 14075.
- (30) Bischak, C. G.; Lai, M.; Fan, Z.; Lu, D.; David, P.; Dong, D.; Chen, H.; Etman, A. S.; Lei, T.; Sun, J. Liquid-like interfaces mediate structural phase transitions in lead halide perovskites. *Matter* **2020**, *3* (2), 534-545.
- (31) Huang, T.; Tan, S.; Nuryyeva, S.; Yavuz, I.; Babbe, F.; Zhao, Y.; Abdelsamie, M.; Weber, M. H.; Wang, R.; Houk, K. N. Performance-limiting formation dynamics in mixed-halide perovskites. *Science advances* **2021**, *7* (46), eabj1799.
- (32) Szostak, R.; de Souza Gonçalves, A.; de Freitas, J. N.; Marchezi, P. E.; de Araújo, F. L.; Tolentino, H. C. N.; Toney, M. F.; das Chagas Marques, F.; Nogueira, A. F. In situ and operando characterizations of metal halide perovskite and solar cells: insights from lab-sized devices to upscaling processes. *Chemical reviews* **2023**, *123* (6), 3160-3236.
- (33) Yadavalli, S. K.; Dai, Z.; Hu, M.; Dong, Q.; Li, W.; Zhou, Y.; Zia, R.; Padture, N. P. Mechanisms of exceptional grain growth and stability in formamidinium lead triiodide thin films for perovskite solar cells. *Acta Materialia* **2020**, *193*, 10-18.
- (34) Ahlawat, P.; Hinderhofer, A.; Alharbi, E. A.; Lu, H.; Ummadisingu, A.; Niu, H.; Invernizzi, M.; Zakeeruddin, S. M.; Dar, M. I.; Schreiber, F. A combined molecular dynamics and experimental study of two-step process enabling low-temperature formation of phase-pure α-FAPbI3. *Science Advances* **2021**, *7* (17), eabe3326.
- (35) Han, Q.; Bae, S.-H.; Sun, P.; Hsieh, Y.-T.; Yang, Y. M.; Rim, Y. S.; Zhao, H.; Chen, Q.; Shi, W.; Li, G. Single Crystal Formamidinium Lead Iodide (FAPbI3): Insight into the Structural, Optical, and Electrical Properties. *Advanced Materials (Deerfield Beach, Fla.)* **2016**, *28* (11), 2253-2258.
- (36) Mandal, T. N.; Heo, J. H.; Im, S. H.; Kim, W. S. Highly Efficient and Stable Inverted Perovskite Solar Cell Using Pure δ -FAPbI3 Single Crystals. *Small* **2023**, 19 (52), 2305246.
- (37) Chen, Y.-X.; Ge, Q.-Q.; Shi, Y.; Liu, J.; Xue, D.-J.; Ma, J.-Y.; Ding, J.; Yan, H.-J.; Hu, J.-S.; Wan, L.-J. General space-confined on-substrate fabrication of thickness-adjustable hybrid perovskite single-crystalline thin films. *Journal of the American*



Chemical Society 2016, 138 (50), 16196-16199.

- (38) Moore, D. T.; Sai, H.; Tan, K. W.; Smilgies, D.-M.; Zhang, W.; Snaith, H. J.; Wiesner, U.; Estroff, L. A. Crystallization kinetics of organic–inorganic trihalide perovskites and the role of the lead anion in crystal growth. *Journal of the American Chemical Society* **2015**, *137* (6), 2350-2358.
- (39) Sánchez, S.; Cacovich, S.; Vidon, G.; Guillemoles, J.-F.; Eickemeyer, F.; Zakeeruddin, S. M.; Schawe, J. E.; Löffler, J. F.; Cayron, C.; Schouwink, P. Thermally controlled growth of photoactive FAPbI 3 films for highly stable perovskite solar cells. *Energy & Environmental Science* **2022**, *15* (9), 3862-3876.
- (40) Lai, M.; Lei, T.; Zhang, Y.; Jin, J.; Steele, J. A.; Yang, P. Phase transition dynamics in one-dimensional halide perovskite crystals. *MRS Bulletin* **2021**, *4*6, 310-316.
- (41) Málek, J. The applicability of Johnson-Mehl-Avrami model in the thermal analysis of the crystallization kinetics of glasses. *Thermochimica acta* **1995**, *267*, 61-73.
- (42) Wang, X.; Liu, Y.; Liu, N.; Sun, R.; Zheng, W.; Liu, H.; Zhang, Y. Revisiting the nanocrystal formation process of zero-dimensional perovskite. *Journal of Materials Chemistry A* **2021**, 9 (8), 4658-4663.
- (43) Ho, K.; Wei, M.; Sargent, E. H.; Walker, G. C. Grain transformation and degradation mechanism of formamidinium and cesium lead iodide perovskite under humidity and light. *ACS Energy Letters* **2021**, 6 (3), 934-940.
- (44) Yun, J. S.; Kim, J.; Young, T.; Patterson, R. J.; Kim, D.; Seidel, J.; Lim, S.; Green, M. A.; Huang, S.; Ho Baillie, A. Humidity induced degradation via grain boundaries of HC (NH2) 2PbI3 planar perovskite solar cells. *Advanced Functional Materials* **2018**, *28* (11), 1705363.
- (45) Feng, L.; Kannan, S. B.; Egan, A.; Smith, T.; Mills, M. J.; Ghazisaeidi, M.; Wang, Y. Localized phase transformation at stacking faults and mechanism-based alloy design. *Acta Materialia* **2022**, *240*, 118287.
- (46) Schelhas, L. T.; Li, Z.; Christians, J. A.; Goyal, A.; Kairys, P.; Harvey, S. P.; Kim, D. H.; Stone, K. H.; Luther, J. M.; Zhu, K. Insights into operational stability and processing of halide perovskite active layers. *Energy & Environmental Science* **2019**, *12* (4), 1341-1348.
- (47) Liu, Y.; Akin, S.; Hinderhofer, A.; Eickemeyer, F. T.; Zhu, H.; Seo, J. Y.; Zhang, J.; Schreiber, F.; Zhang, H.; Zakeeruddin, S. M. Stabilization of highly efficient and stable phase pure FAPbI3 perovskite solar cells by molecularly tailored 2D overlayers. *Angewandte Chemie International Edition* **2020**, *59* (36), 15688-15694. (48) Svane, K. L.; Forse, A. C.; Grey, C. P.; Kieslich, G.; Cheetham, A. K.; Walsh, A.; Butler, K. T. How strong is the hydrogen bond in hybrid perovskites? *The journal of physical chemistry letters* **2017**, *8* (24), 6154-6159.

- (49) Chen, Q.; De Marco, N.; Yang, Y. M.; Song, T.-B.; Chen, C.-C.; Zhao, H.; Hong, Z.; Zhou, H.; Yang, Y. Under the spotlight: The organic–inorganic hybrid halide perovskite for optoelectronic applications. *Nano Today* **2015**, *10* (3), 355-396.
- (50) Zhao, Y.; Zhu, K. Organic-inorganic hybrid lead halide perovskites for optoelectronic and electronic applications. *Chemical Society Reviews* **2016**, *45* (3), 655-689.
- (51) Ning, Z.; Gong, X.; Comin, R.; Walters, G.; Fan, F.; Voznyy, O.; Yassitepe, E.; Buin, A.; Hoogland, S.; Sargent, E. H. Quantum-dot-in-perovskite solids. *Nature* **2015**, *523* (7560), 324-328.
- (52) Yu, Y.; Zhang, D.; Yang, P. Ruddlesden–Popper phase in two-dimensional inorganic halide perovskites: a plausible model and the supporting observations. *Nano letters* **2017**, *17* (9), 5489-5494.
- (53) Kim, H.; Lee, S. U.; Lee, D. Y.; Paik, M. J.; Na, H.; Lee, J.; Seok, S. I. Optimal interfacial engineering with different length of alkylammonium halide for efficient and stable perovskite solar cells. *Advanced Energy Materials* **2019**, 9 (47), 1902740.
- (54) Wang, K.; Park, J. Y.; Akriti; Dou, L. Two dimensional halide perovskite quantum-well emitters: a critical review. *EcoMat* **2021**, *3* (3), e12104.
- (55) Wu, G.; Liang, R.; Ge, M.; Sun, G.; Zhang, Y.; Xing, G. Surface passivation using 2D perovskites toward efficient and stable perovskite solar cells. *Advanced Materials* **2022**, *34* (8), 2105635.
- (56) Liu, P.; Han, N.; Wang, W.; Ran, R.; Zhou, W.; Shao, Z. High quality Ruddlesden–Popper perovskite film formation for high-performance perovskite solar cells. *Advanced Materials* **2021**, *33* (10), 2002582.
- (57) Glazer, A. M. The classification of tilted octahedra in perovskites. *Acta Crystallographica Section B: Structural Crystallography and Crystal Chemistry* **1972**, *28* (11), 3384-3392.
- (58) Woodward, P. M. Octahedral tilting in perovskites. I. Geometrical considerations. *Acta Crystallographica Section B: Structural Science* **1997**, *53* (1), 32-43.
- (59) Gao, P.; Grätzel, M.; Nazeeruddin, M. K. Organohalide lead perovskites for photovoltaic applications. *Energy & Environmental Science* **2014**, *7* (8), 2448-2463.
- (60) Sekar, K.; Manisekaran, R.; Nwakanma, O. M.; Babudurai, M. Significance of Formamidinium Incorporation in Perovskite Composition and Its Impact on Solar Cell Efficiency: A Mini Review. *Advanced Energy and Sustainability Research* **2024**. 2400003.
- (61) Fan, Z.; Xiao, J.; Sun, K.; Chen, L.; Hu, Y.; Ouyang, J.; Ong, K. P.; Zeng, K.; Wang,



- J. Ferroelectricity of CH3NH3Pbl3 perovskite. *The journal of physical chemistry letters* **2015**, 6 (7), 1155-1161.
- (62) Strelcov, E.; Dong, Q.; Li, T.; Chae, J.; Shao, Y.; Deng, Y.; Gruverman, A.; Huang, J.; Centrone, A. CH3NH3Pbl3 perovskites: Ferroelasticity revealed. *Science advances* **2017**, *3* (4), e1602165.
- (63) Sutton, R. J.; Filip, M. R.; Haghighirad, A. A.; Sakai, N.; Wenger, B.; Giustino, F.; Snaith, H. J. Cubic or orthorhombic? Revealing the crystal structure of metastable black-phase CsPbI3 by theory and experiment. *ACS Energy Letters* **2018**, *3* (8), 1787-1794.
- (64) Quarti, C.; Mosconi, E.; Ball, J. M.; D'Innocenzo, V.; Tao, C.; Pathak, S.; Snaith, H. J.; Petrozza, A.; De Angelis, F. Structural and optical properties of methylammonium lead iodide across the tetragonal to cubic phase transition: implications for perovskite solar cells. *Energy & Environmental Science* **2016**, 9 (1), 155-163.
- (65) Prathapani, S.; Choudhary, D.; Mallick, S.; Bhargava, P.; Yella, A. Experimental evaluation of room temperature crystallization and phase evolution of hybrid perovskite materials. *CrystEngComm* **2017**, *19* (27), 3834-3843.
- (66) Ghosh, S.; Mishra, S.; Singh, T. Antisolvents in perovskite solar cells: importance, issues, and alternatives. *Advanced materials interfaces* **2020**, *7* (18), 2000950.
- (67) Xiao, M.; Huang, F.; Huang, W.; Dkhissi, Y.; Zhu, Y.; Etheridge, J.; Gray-Weale, A.; Bach, U.; Cheng, Y. B.; Spiccia, L. A fast deposition-crystallization procedure for highly efficient lead iodide perovskite thin film solar cells. *Angewandte Chemie International Edition* **2014**, 53 (37), 9898-9903.
- (68) Si, H.; Zhang, Z.; Liao, Q.; Zhang, G.; Ou, Y.; Zhang, S.; Wu, H.; Wu, J.; Kang, Z.; Zhang, Y. A site management for highly crystalline perovskites. *Advanced Materials* **2020**, *32* (4), 1904702.
- (69) Li, B.; Dai, Q.; Yun, S.; Tian, J. Insights into iodoplumbate complex evolution of precursor solutions for perovskite solar cells: from aging to degradation. *Journal of Materials Chemistry A* **2021**, 9 (11), 6732-6748.
- (70) Taylor, A. D.; Sun, Q.; Goetz, K. P.; An, Q.; Schramm, T.; Hofstetter, Y.; Litterst, M.; Paulus, F.; Vaynzof, Y. A general approach to high-efficiency perovskite solar cells by any antisolvent. *Nature communications* **2021**, *12* (1), 1878.
- (71) Dhull, J.; Sharma, D. Dielectric relaxation and dipole moment of N, N-dimethylformamide in benzene, dioxane and carbon tetrachloride solutions from microwave absorption studies. *Journal of Physics D: Applied Physics* **1982**, *15* (11), 2307.
- (72) Jaw, C.-G.; Chen, I.-M.; Yen, J.-H.; Wang, Y.-S. Partial solubility parameters of

- chlorobenzene and chlorophenol compounds at equilibrium distribution in two immiscible phases. *Chemosphere* **1999**, 39 (15), 2607-2620.
- (73) Taherianfard, H.; Kim, G.-W.; Byranvand, M. M.; Choi, K.; Kang, G.; Choi, H.; Tajabadi, F.; Taghavinia, N.; Park, T. Effective management of nucleation and crystallization processes in perovskite formation via facile control of antisolvent temperature. *ACS Applied Energy Materials* **2020**, *3* (2), 1506-1514.
- (74) Zhang, F.; Zhu, K. Additive engineering for efficient and stable perovskite solar cells. *Advanced Energy Materials* **2020**, *10* (13), 1902579.
- (75) Lyu, M.; Park, N.-G. Effect of additives AX (A= FA, MA, Cs, Rb, NH4, X= Cl, Br, I) in FAPbI3 on photovoltaic parameters of perovskite solar cells. *Solar RRL* **2020**, *4* (10), 2000331.
- (76) Wang, Y.; Mei, X.; Qiu, J.; Zhou, Q.; Jia, D.; Yu, M.; Liu, J.; Zhang, X. Insight into the interface engineering of a SnO2/FAPbI3 perovskite using lead halide as an interlayer: a first-principles study. *The Journal of Physical Chemistry Letters* **2021**, *12* (46), 11330-11338.
- (77) Kim, M.; Kim, G.-H.; Lee, T. K.; Choi, I. W.; Choi, H. W.; Jo, Y.; Yoon, Y. J.; Kim, J. W.; Lee, J.; Huh, D. Methylammonium chloride induces intermediate phase stabilization for efficient perovskite solar cells. *Joule* **2019**, *3* (9), 2179-2192.
- (78) Ma, L.; Yan, Z.; Zhou, X.; Pi, Y.; Du, Y.; Huang, J.; Wang, K.; Wu, K.; Zhuang, C.; Han, X. A polymer controlled nucleation route towards the generalized growth of organic-inorganic perovskite single crystals. *Nature communications* **2021**, *12* (1), 2023.
- (79) Xiong, H.; DeLuca, G.; Rui, Y.; Zhang, B.; Li, Y.; Zhang, Q.; Wang, H.; Reichmanis, E. Modifying perovskite films with polyvinylpyrrolidone for ambient-air-stable highly bendable solar cells. *ACS applied materials & interfaces* **2018**, *10* (41), 35385-35394.
- (80) Zhang, W.; Xiong, J.; Li, J.; Daoud, W. A. Guanidinium induced phase separated perovskite layer for efficient and highly stable solar cells. *Journal of Materials Chemistry A* **2019**, *7* (16), 9486-9496.
- (81) Syzgantseva, O. A.; Saliba, M.; Grätzel, M.; Rothlisberger, U. Stabilization of the perovskite phase of formamidinium lead triiodide by methylammonium, Cs, and/or Rb doping. *The journal of physical chemistry letters* **2017**, *8* (6), 1191-1196.
- (82) Mei, F.; Sun, D.; Mei, S.; Feng, J.; Zhou, Y.; Xu, J.; Xiao, X. Recent progress in perovskite-based photodetectors: the design of materials and structures. *Advances in Physics: X* **2019**, *4* (1), 1592709.
- (83) Gao, Q.; Qi, J.; Chen, K.; Xia, M.; Hu, Y.; Mei, A.; Han, H. Halide perovskite crystallization processes and methods in nanocrystals, single crystals, and thin films. *Advanced Materials* **2022**, *34* (52), 2200720.

- (84) Saidaminov, M. I.; Abdelhady, A. L.; Murali, B.; Alarousu, E.; Burlakov, V. M.; Peng, W.; Dursun, I.; Wang, L.; He, Y.; Maculan, G. High-quality bulk hybrid perovskite single crystals within minutes by inverse temperature crystallization. *Nature communications* **2015**, 6 (1), 7586.
- (85) Han, Q.; Bae, S. H.; Sun, P.; Hsieh, Y. T.; Yang, Y.; Rim, Y. S.; Zhao, H.; Chen, Q.; Shi, W.; Li, G. Single crystal formamidinium lead iodide (FAPbI3): insight into the structural, optical, and electrical properties. *Advanced Materials* **2016**, *28* (11), 2253-2258.
- (86) Konstantakou, M.; Perganti, D.; Falaras, P.; Stergiopoulos, T. Anti-solvent crystallization strategies for highly efficient perovskite solar cells. *Crystals* **2017**, 7(10), 291.
- (87) Chen, Z.; Dong, Q.; Liu, Y.; Bao, C.; Fang, Y.; Lin, Y.; Tang, S.; Wang, Q.; Xiao, X.; Bai, Y. Thin single crystal perovskite solar cells to harvest below-bandgap light absorption. *Nature communications* **2017**, *8* (1), 1890.
- (88) Alsalloum, A. Y.; Turedi, B.; Almasabi, K.; Zheng, X.; Naphade, R.; Stranks, S. D.; Mohammed, O. F.; Bakr, O. M. 22.8%-Efficient single-crystal mixed-cation inverted perovskite solar cells with a near-optimal bandgap. *Energy & Environmental Science* **2021**, *14* (4), 2263-2268.
- (89) Ding, R.; Liu, C.-K.; Wu, Z.; Guo, F.; Pang, S.-Y.; Wong, L. W.; Io, W. F.; Yuan, S.; Wong, M.-C.; Jedrzejczyk, M. B. A general wet transferring approach for diffusion-facilitated space-confined grown perovskite single-crystalline optoelectronic thin films. *Nano Letters* **2020**, *20* (4), 2747-2755.
- (90) Rothmann, M. U.; Li, W.; Zhu, Y.; Liu, A.; Ku, Z.; Bach, U.; Etheridge, J.; Cheng, Y. B. Structural and chemical changes to CH3NH3PbI3 induced by electron and gallium ion beams. *Advanced Materials* **2018**, *30* (25), 1800629.
- (91) Chen, S.; Zhang, Y.; Zhao, J.; Mi, Z.; Zhang, J.; Cao, J.; Feng, J.; Zhang, G.; Qi, J.; Li, J. Transmission electron microscopy of organic-inorganic hybrid perovskites: myths and truths. *Science Bulletin* **2020**, 65 (19), 1643-1649.
- (92) Yang, C. Q.; Zhi, R.; Rothmann, M. U.; Xu, Y. Y.; Li, L. Q.; Hu, Z. Y.; Pang, S.; Cheng, Y. B.; Van Tendeloo, G.; Li, W. Unveiling the intrinsic structure and intragrain defects of organic–inorganic hybrid perovskites by ultralow dose transmission electron microscopy. *Advanced Materials* **2023**, *35* (17), 2211207.
- (93) Rothmann, M. U.; Li, W.; Zhu, Y.; Bach, U.; Spiccia, L.; Etheridge, J.; Cheng, Y.-B. Direct observation of intrinsic twin domains in tetragonal CH3NH3Pbl3. *Nature communications* **2017**, *8* (1), 14547.
- (94) Chen, S.; Zhang, Y.; Zhang, X.; Zhao, J.; Zhao, Z.; Su, X.; Hua, Z.; Zhang, J.; Cao, J.; Feng, J. General decomposition pathway of organic–inorganic hybrid perovskites through an intermediate superstructure and its suppression



mechanism. Advanced Materials 2020, 32 (29), 2001107.

- (95) Camarero, J.; Spendeler, L.; Schmidt, G.; Heinz, K.; De Miguel, J.; Miranda, R. Surfactant-induced suppression of twin formation during growth of fcc Co/Cu superlattices on Cu (111). *Physical review letters* **1994**, *73* (18), 2448.
- (96) Shi, H.; Dong, B.; Wang, W. Features of twins and stacking faults in silver nanorice and electron-beam irradiation effect. *Nanoscale* **2012**, *4* (20), 6389-6392.
- (97) Pham, H. T.; Duong, T.; Weber, K. J.; Wong-Leung, J. Insights into twinning formation in cubic and tetragonal multi-cation mixed-halide perovskite. *ACS Materials Letters* **2020**, *2* (4), 415-424.
- (98) Zhu, K.; Yang, M.; Zhou, Y.; Padture, N. P. Methods for producing perovskite halide films. Google Patents: 2022.
- (99) Lee, J.-W.; Tan, S.; Han, T.-H.; Wang, R.; Zhang, L.; Park, C.; Yoon, M.; Choi, C.; Xu, M.; Liao, M. E. Solid-phase hetero epitaxial growth of α-phase formamidinium perovskite. *Nature communications* **2020**, *11* (1), 5514.
- (100) Wang, P.; Guan, J.; Galeschuk, D. T.; Yao, Y.; He, C. F.; Jiang, S.; Zhang, S.; Liu, Y.; Jin, M.; Jin, C. Pressure-induced polymorphic, optical, and electronic transitions of formamidinium lead iodide perovskite. *The journal of physical chemistry letters* **2017**, *8* (10), 2119-2125.
- (101) Sanchez, R. S.; Gonzalez-Pedro, V.; Lee, J.-W.; Park, N.-G.; Kang, Y. S.; Mora-Sero, I.; Bisquert, J. Slow dynamic processes in lead halide perovskite solar cells. Characteristic times and hysteresis. *The journal of physical chemistry letters* **2014**, *5* (13), 2357-2363.
- (102) Fanfoni, M.; Tomellini, M. The johnson-mehl-avrami-kohnogorov model: a brief review. *Il Nuovo Cimento D* **1998**, *20*, 1171-1182.
- (103) Shirzad, K.; Viney, C. A critical review on applications of the Avrami equation beyond materials science. *Journal of the Royal Society Interface* **2023**, *20* (203), 20230242.
- (104) Xu, A. F.; Liu, N.; Xie, F.; Song, T.; Ma, Y.; Zhang, P.; Bai, Y.; Li, Y.; Chen, Q.; Xu, G. Promoting thermodynamic and kinetic stabilities of FA-based perovskite by an in situ bilayer structure. *Nano Letters* **2020**, *20* (5), 3864-3871.
- (105) Chen, T.; Foley, B. J.; Park, C.; Brown, C. M.; Harriger, L. W.; Lee, J.; Ruff, J.; Yoon, M.; Choi, J. J.; Lee, S.-H. Entropy-driven structural transition and kinetic trapping in formamidinium lead iodide perovskite. *Science advances* **2016**, *2* (10), e1601650.
- (106) Niu, T.; Chao, L.; Xia, Y.; Wang, K.; Ran, X.; Huang, X.; Chen, C.; Wang, J.; Li, D.; Su, Z. Phase-Pure α -FAPbI3 Perovskite Solar Cells via Activating Lead–Iodine Frameworks. *Advanced Materials* **2024**, *36* (13), 2309171.
- (107) Liu, J.; Cao, J.; Zhang, M.; Sun, X.; Hou, T.; Yang, X.; Xiang, L.; Liu, X.; Fu, Z.;

- Huang, Y. Methylammonium-Free Ink for Blade-Coating of Pure-Phase α -FAPbI3 Perovskite Films in Air. *Advanced Science*, 2410266.
- (108) Wang, X.; Zheng, G.; Gao, F.; Li, L.; Luo, C.; Zhan, C.; Li, Y.; Ma, Y.; Gao, X.; Zhou, H. In Situ Study of Purified Phase Transition Path for α FAPbI3 Crystallization. *Advanced Energy Materials* **2024**, *14* (14), 2303949.
- (109) Chen, M.; Niu, T.; Chao, L.; Duan, X.; Wang, J.; Pan, T.; Li, Y.; Zhang, J.; Wang, C.; Ren, B. "Freezing" intermediate phases for efficient and stable FAPbI 3 perovskite solar cells. *Energy & Environmental Science* **2024**, *17* (10), 3375-3383. (110) Wang, S.; Miao, Z.; Yang, J.; Gu, Z.; Li, P.; Zhang, Y.; Song, Y. Lead-Chelating Intermediate for Air Processed Phase Pure FAPbI3 Perovskite Solar Cells. *Angewandte Chemie* **2024**, e202407192.
- (111) Luo, T.; Chen, R.; Zhang, G.; Li, L.; Wu, H.; Zhang, W.; Chen, W.; Chang, H. MASCN Surface Treatment to Reduce Phase Transition Temperature and Regulate Strain for Efficient and Stable α-FAPbI3 Perovskite Solar Cells. *ACS Applied Materials & Interfaces* **2023**, *15* (32), 38496-38506.
- (112) Kresse, G.; Furthmüller, J. Efficiency of ab-initio total energy calculations for metals and semiconductors using a plane-wave basis set. *Computational materials science* **1996**, 6 (1), 15-50.
- (113) Kresse, G.; Hafner, J. Ab initio molecular dynamics for liquid metals. *Physical review B* **1993**, *47* (1), 558.
- (114) Brooks, K. III i I. Statistics 2000, 2002 (2004), 2001.
- (115) Nan, Z.-A.; Chen, L.; Liu, Q.; Wang, S.-H.; Chen, Z.-X.; Kang, S.-Y.; Ji, J.-B.; Tan, Y.-Y.; Hui, Y.; Yan, J.-W. Revealing phase evolution mechanism for stabilizing formamidinium-based lead halide perovskites by a key intermediate phase. *Chem* **2021**, *7* (9), 2513-2526.
- (116) Tanaka, M.; Sekii, H.; Nagasawa, T. Space-group determination by dynamic extinction in convergent-beam electron diffraction. *Acta Crystallographica Section A: Foundations of Crystallography* **1983**, 39 (6), 825-837.
- (117) Vigil, J. A.; Hazarika, A.; Luther, J. M.; Toney, M. F. FA x Cs1–x PbI3 Nanocrystals: tuning crystal symmetry by A-site cation composition. *ACS Energy Letters* **2020**, *5* (8), 2475-2482.
- (118) Gratia, P.; Zimmermann, I.; Schouwink, P.; Yum, J.-H.; Audinot, J.-N.; Sivula, K.; Wirtz, T.; Nazeeruddin, M. K. The many faces of mixed ion perovskites: unraveling and understanding the crystallization process. *ACS Energy Letters* **2017**, *2* (12), 2686-2693.
- (119) Chen, Y.; Lei, Y.; Li, Y.; Yu, Y.; Cai, J.; Chiu, M.-H.; Rao, R.; Gu, Y.; Wang, C.; Choi, W. Strain engineering and epitaxial stabilization of halide perovskites. *Nature* **2020**, *577* (7789), 209-215.

- (120) Fan, H.; Li, F.; Wang, P.; Gu, Z.; Huang, J.-H.; Jiang, K.-J.; Guan, B.; Yang, L.-M.; Zhou, X.; Song, Y. Methylamine-assisted growth of uniaxial-oriented perovskite thin films with millimeter-sized grains. *Nature Communications* **2020**, *11* (1), 5402.
- (121) Weller, M. T.; Weber, O. J.; Frost, J. M.; Walsh, A. Cubic perovskite structure of black formamidinium lead iodide, α -[HC (NH2) 2] PbI3, at 298 K. *The journal of physical chemistry letters* **2015**, 6 (16), 3209-3212.
- (122) Xu, C.; Mao, J.; Guo, X.; Yan, S.; Chen, Y.; Lo, T. W.; Chen, C.; Lei, D.; Luo, X.; Hao, J. Two-dimensional ferroelasticity in van der Waals β '-In2Se3. *Nature Communications* **2021**, *12* (1), 3665.
- (123) Soffa, W.; Laughlin, D. E. Diffusional phase transformations in the solid state. In *Physical metallurgy*, Elsevier, 2014; pp 851-1020.
- (124) Van der Zwaag, S. Kinetics of phase transformations in steels. In *Phase Transformations in Steels*, Elsevier, 2012; pp 126-156.
- (125) Maurya, S. K.; Nie, J. F.; Alankar, A. Atomistic analyses of HCP-FCC transformation and reorientation of Ti in Al-Ti multilayers. *Computational Materials Science* **2021**, *192*, 110329.
- (126) Yang, J. X.; Zhao, H. L.; Gong, H. R.; Song, M.; Ren, Q. Q. Proposed mechanism of HCP→ FCC phase transition in titianium through first principles calculation and experiments. *Scientific reports* **2018**, *8* (1), 1992.
- (127) Tyson, W. Basal and prismatic slip in hcp crystals. *Acta metallurgica* **1967**, *15* (3), 574-577.
- (128) Howe, J.; Aaronson, H.; Hirth, J. Aspects of interphase boundary structure in diffusional phase transformations. *Acta materialia* **2000**, *48* (15), 3977-3984.
- (129) Li, S.; Xiao, Y.; Su, R.; Xu, W.; Luo, D.; Huang, P.; Dai, L.; Chen, P.; Caprioglio, P.; Elmestekawy, K. A. Coherent growth of high-Miller-index facets enhances perovskite solar cells. *Nature* **2024**, 1-3.
- (130) Ma, C.; Kang, M.-C.; Lee, S.-H.; Kwon, S. J.; Cha, H.-W.; Yang, C.-W.; Park, N.-G. Photovoltaically top-performing perovskite crystal facets. *Joule* **2022**, 6 (11), 2626-2643.
- (131) He, J.; Li, D.; Liu, H.; Xiang, J.; Bai, J.; Ren, Y.; Wang, Z.; Xia, M.; Yin, X.; Yuan, L. Single Crystal Seeds Inducing the Crystallization of High Performance α -FAPbI3 for Efficient Perovskite Solar Cells. *Advanced Energy Materials* **2023**, *13* (23), 2300451.
- (132) Shin, S.; Seo, S.; Jeong, S.; Sharbirin, A. S.; Kim, J.; Ahn, H.; Park, N. G.; Shin, H. Kinetic Controlled Crystallization of α FAPbI3 Inducing Preferred Crystallographic Orientation Enhances Photovoltaic Performance. *Advanced Science* **2023**, *10* (14), 2300798.
- (133) Meng, K.; Wang, X.; Xu, Q.; Li, Z.; Liu, Z.; Wu, L.; Hu, Y.; Liu, N.; Chen, G. In

- situ observation of crystallization dynamics and grain orientation in sequential deposition of metal halide perovskites. *Advanced Functional Materials* **2019**, *29* (35), 1902319.
- (134) Thapliyal, S.; Agrawal, P.; Agrawal, P.; Nene, S. S.; Mishra, R. S.; McWilliams, B. A.; Cho, K. C. Segregation engineering of grain boundaries of a metastable Fe-Mn-Co-Cr-Si high entropy alloy with laser-powder bed fusion additive manufacturing. *Acta Materialia* **2021**, *219*, 117271.
- (135) Li, X.; Li, J.; Kou, H.; Zhu, B. Atomic-scale understanding of the unilateral thickening of γ lamellae during α to γ phase transformation in Ti48Al2Cr2Nb alloy. *Materials Letters* **2018**, *229*, 202-205.
- (136) Hitzenberger, C.; Karnthaler, H.; Korner, A. In situ TEM study of the hcp to fcc martensitic phase transformation in CoNi single crystals. *Acta Metallurgica* **1988**, 36 (10), 2719-2728.
- (137) Hitzenberger, C.; Karnthaler, H. Weak-beam TEM study of the hcp to fcc martensitic phase transformation lamellae in CoNi. *Philosophical Magazine A* **1991**, *64* (1), 151-163.
- (138) Mittemeijer, E. Analysis of the kinetics of phase transformations. *Journal of Materials science* **1992**, *27*, 3977-3987.
- (139) Readey, D. W. Kinetics in materials science and engineering; CRC Press, 2017.
- (140) Lee, S. R.; Lee, D.; Choi, S. G.; Jung, S. K.; Lee, J. H.; Kim, M. c.; Park, J. S.; Lee, J. W. Accelerated degradation of FAPbI3 perovskite by excess charge carriers and humidity. *Solar RRL* **2024**, *8* (5), 2300958.
- (141) Ruellou, J.; Courty, M.; Sauvage, F. Thermal and Photo-Degradation Study of α -FAPbI3-Based Perovskite Using In Situ X-Ray Diffraction. *Advanced Functional Materials* **2023**, *33* (34), 2300811.
- (142) Raval, P.; Kennard, R. M.; Vasileiadou, E. S.; Dahlman, C. J.; Spanopoulos, I.; Chabinyc, M. L.; Kanatzidis, M.; Manjunatha Reddy, G. Understanding instability in formamidinium lead halide perovskites: kinetics of transformative reactions at grain and subgrain boundaries. *ACS Energy Letters* **2022**, *7* (4), 1534-1543.
- (143) Hirel, P.; Marton, P.; Mrovec, M.; Elsässer, C. Theoretical investigation of {1 1 0} generalized stacking faults and their relation to dislocation behavior in perovskite oxides. *Acta materialia* **2010**, *58* (18), 6072-6079.
- (144) Zhou, Y.; Vasiliev, A. L.; Wu, W.; Yang, M.; Pang, S.; Zhu, K.; Padture, N. P. Crystal morphologies of organolead trihalide in mesoscopic/planar perovskite solar cells. *The journal of physical chemistry letters* **2015**, 6 (12), 2292-2297.
- (145) Mehdi, H.; Matheron, M.; Mhamdi, A.; Cros, S.; Bouazizi, A. Effect of the hole transporting layers on the inverted perovskite solar cells. *Journal of Materials*



Science: Materials in Electronics **2021**, 32 (16), 21579-21589.

(146) Yang, X.; Luo, D.; Xiang, Y.; Zhao, L.; Anaya, M.; Shen, Y.; Wu, J.; Yang, W.; Chiang, Y. H.; Tu, Y. Buried interfaces in halide perovskite photovoltaics. *Advanced materials* **2021**, *33* (7), 2006435.

(147) Rombach, F. M.; Haque, S. A.; Macdonald, T. J. Lessons learned from spiro-OMeTAD and PTAA in perovskite solar cells. *Energy & Environmental Science* **2021**, *14* (10), 5161-5190.

(148) Wang, M.; Wang, H.; Li, W.; Hu, X.; Sun, K.; Zang, Z. Defect passivation using ultrathin PTAA layers for efficient and stable perovskite solar cells with a high fill factor and eliminated hysteresis. *Journal of Materials Chemistry A* **2019**, *7* (46), 26421-26428.

(149) Akbulatov, A. F.; Frolova, L. A.; Griffin, M. P.; Gearba, I. R.; Dolocan, A.; Vanden Bout, D. A.; Tsarev, S.; Katz, E. A.; Shestakov, A. F.; Stevenson, K. J. Effect of Electron-Transport Material on Light-Induced Degradation of Inverted Planar Junction Perovskite Solar Cells. *Advanced Energy Materials* **2017**, *7* (19), 1700476. (150) Kroll, M.; Öz, S. D.; Zhang, Z.; Ji, R.; Schramm, T.; Antrack, T.; Vaynzof, Y.; Olthof, S.; Leo, K. Insights into the evaporation behaviour of FAI: material degradation and consequences for perovskite solar cells. *Sustainable Energy & Fuels* **2022**, 6 (13), 3230-3239.